НАУЧНОМ ВЕЋУ
ИНСТИТУТА ЗА ФИЗИКУ
УНИВЕРЗИТЕТ У БЕОГРАДУ

Предмет: покретање поступка за избор у звање истраживач-сарадник

Молим Научно веће Института за физику, Универзитета у Београду, да покрене поступак за мој избор у звање истраживач сарадник

У прилогу достављам:

1. Мишљење руководиоца пројекта са предлогом комисије која ће писати извештај.

2. Кратку стручну биографија кандидата.

3. Кратак преглед научне активности кандидата.

4. Списак објављених радова и других публикација, разврстан по важећим категоријама прописаним Правилником.

5. Копије објављених радова и других публикација

6. Потврда о уписаним докторским студијама.

7. Потврда о просеку на основним и мастер студијама (фотокопија дипломе).

8. Потврда о прихваћеној теми докторске дисертације.

У Београду,   Тијана Томашевић-Илић

24.05.2019.

НАУЧНОМ ВЕЋУ
ИНСТИТУТА ЗА ФИЗИКУ
УНИВЕРЗИТЕТ У БЕОГРАДУ

Предмет: Мишљење руководиоца пројекта о избору у звање истраживач-сарадник кандидата Тијане Томашевић-Илић са предлогом комисије која ће писати извештај

Тијана Томашевић-Илић је од 01.11.2016. запослена у Лабораторији за графен, друге 2Д материјале и уређене наноструктуре, Центра за чврсто стање и нове материјале на Институту за физику Београд, Универзитет у Београду. Ангажована је на пројекту ОИ171005 „Физика уређених наноструктура и нових материјала у нанофотоници" финансираним од стране Министарства за просвету, науку и технолошки развој Републике Србије, са фокусом истраживања танких филмова 2Д материјала добијених методом ексфолијације из течне фазе. Аутор и коаутор је шест научних радова и дванаест саопштења са међународних конференција (прилог). На 25. седници Већа научних области природних наука, одржаној 25.04.2019. године, одобрена јој је тема докторске дисертације под називом „Површинска модификација графена ексфолираног из течне фазе и депонованог Лангмир-Блоџетовом методом".

Обзиром да испуњава све услове предвиђене Законом о научно-истраживачкој делатности и Правилником о поступку, начину вредновања и квалитативном исказивању научноистраживачких резултата истраживача МНПТР Републике Србије, сагласан сам са покретањем поступка за избор Тијане Томашевић-Илић у звање истраживач-сарадник.

За чланове комисије за избор Тијане Томашевић-Илић у звање истраживач-сарадник предлажем:

1. Др Радоша Гајића, научног саветника, Института за физику, Универзитета у Београду
2. Др Јелену Пешић, научног сарадника, Института за физику, Универзитета у Београду
3. Др Марка Спасеновића, вишег научног сарадника, Института за хемију, технологију и металургију, Универзитета у Београду

Руководилац пројекта
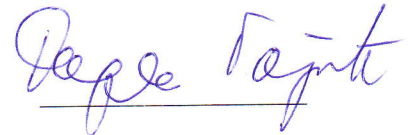
Др. Радош Гајић

У Београду,

06.05.2019.

Стручна биографија

Тијана (Драган) Томашевић-Илић рођена је 19. 10. 1982. године у Београду. Основне студије на Факултету за физичку хемију Универзитета у Београду завршила је 2011. године, одбраном дипломског рада „Испитивање глазура византијске керамике применом микро-раманске спектроскопије“. Током 2011. и 2012. године била је учесник програма „Прва Шанса“ у Централном институту за конзервацију. Мастер академске студије Факултета за физичку хемију Универзитета у Београду завршила је 2015. године, одбраном мастер рада „Сребрни филмови на нанокристалној TiO_2 подлози: синтеза, карактеризација и антимикробна активност“. Докторске академске студије уписала је на Факултету за физичку хемију 2015. године. Исте године започела је свој научно-истраживачки рад као волонтер на Институту за физику Универзитет у Београду, у Лабораторији за графен, друге 2Д материјале и уређене наноструктуре, Центра за чврсто стање и нове материјале. У Институту за физику запослена је од новембра 2016. године. Ангажована је на пројекту ОИ171005 „Физика уређених наноструктура и нових материјала у нанофотоници“, финансираним од стране Министарства за просвету, науку и технолошки развој Републике Србије, са фокусом истраживања танких филмова 2Д материјала добијених методом ексфолијације из течне фазе. Учествовала је у пројекту билатералне сарадње Србија-Хрватска (2016-2017, „Подешавање вишечестичне интеракције у графену интеркалацијом цезијума“) и пројекту Сарадње науке и привреде „Снимање из ваздуха извора буке и имплементација у ГИС-у“ (2017-2018), финансираним од стране Фонда за иновациону делатност. Тијана Томашевић-Илић је аутор/коаутор шест научних радова са СЦИ-листе (два М21а, један М21 и три М22 категорије) и више саопштења са међународних конференција штампаних у изводу.

Кратак преглед научне активности

Тијана Томашевић-Илић запослена је у лабораторији за графен, друге 2Д-материјале и уређене наноструктуре у Центру за физику чврстог стања и нове материјале, Института за физику Универзитета у Београду. Ангажована је на националном пројекту "Физика уређених наноструктура и нових материјала у нанофотоници" ОИ171005.

Истраживања у оквиру докторске дисертације „Површинска модификација графена ексфолираног из течне фазе и депонованог Лангмир-Блоџетовом методом" под менторством др. Марка Спасеновића и проф. Иванке Холцлајтнер-Антуновић, подразумевају испитивање утицаја површинске модификације агресивним методама, као што су фотохемијска оксидација озоном и хемијска функционализација јаким оксидативним средствима на структуру и оптоелектронска својства танких филмова графена добијеног методом ексфолијације из течне фазе индуковане ултразвуком и депонованог на подлогу Лангмир-Блоџетовом методом. Ова метода, која се заснива на (само)организацији наноструктура на течно-гасној међуфази индукованој површинским напоном материјала, представља методу за добијање великих површина високо транспарентног графенског филма на различитим подлогама. Међутим, главни недостатак свих метода које се заснивају на самоорганизацији наноструктура у танке филмове је велика густина дефеката која директно утиче на повећање површинске отпорности филмова. Насупрот томе, управо присуство велике густине дефеката омогућава да се на површини ових филмова, применом одговарајућих метода површинске модификације, одвијају различите физичке интеракције и хемијске промене, које доприносе смањењу површинске отпорности или изазивају неки други жељени ефекат. Истраживање подразумева оптимизацију услова добијања 2Д материјала методом ексфолијације из течне фазе, формирање филмова на површини подлога различитог материјала Лангмир-Блоџетовом методом, карактеризацију добијених филмова, анализу природе и густине дефеката добијених филмова графена, површинску модификацију наведеним методама, испитивање промена на површини самоорганизованих графенских слојева, методама вибрационе спектрометрије (ФТИЦ-Инфрацрвеном спектрометријом са Фуријеовом трансформацијом и микро-раманском спектрометријом), УЉ/ВИД спектрофотометријом, микроскопијом атомских сила, микроскопијом сила Келвиновом пробом и скенирајућом електронском микроскопијом, као и испитивање утицаја површинске модификације на оптоелектронске особине филмова графена добијених Лангмир-Блоџетовом методом. Резултати овог истраживања су до сада публиковани у оквиру два М21а и једног М22 рада и приказани на више конференција од међународног значаја.

Поред основног истраживања везаног за израду докторске дисертације, кандидат се бави анализом танких филмова других 2Д материјала, као што су молибден-дисулфид, хекса-борнитрид и платина-дисулфид, оптимизацијом формирања филмова из раствора ових материјала и могућностима њихове примене у области оптоелектронике.

Списак објављених радова и других публикација

Радови у врхунском међународном часопису изузетних вредности (М21а)

1. **Tijana Tomašević-Ilić**, Đorđe Jovanović, Igor Popov, Rajveer Fandan, Jorge Pedrós, Marko Spasenović and Radoš Gajić, Reducing sheet resistance of self-assembled transparent graphene films by defect patching and doping with UV/ozone treatment, Applied Surface Science 458 (2018) 446–453.
2. Aleksandar Matković, Ivana Milošević, Marijana Milićević, **Tijana Tomašević-Ilić**, Jelena Pešić, Milenko Musić, Marko Spasenović, Djordje Jovanović, Borislav Vasić, Christopher Deeks, Radmila Panajotović, Milivoj R. Belić, and Radoš Gajić, Enhanced sheet conductivity of Langmuir-Blodgett assembled graphene thin films by chemical doping, 2D Materials 3 (2016) 015002.

Радови у врхунском међународном часопису (М21)

3. Ivana D Vukoje, **Tijana D Tomašević-Ilić**, Aleksandra R Zarubica, Suzana Dimitrijević, Milica D Budimir, Mila R Vranješ, Zoran V Šaponjić and Jovan M. Nedeljković, Silver film on nanocrystalline TiO2 support: photocatalytic and antimicrobial ability, Materials Research Bulletin 60 (2014) 824-829.

Радови у истакнутом међународном часопису (М22)

4. Jelena Pešić, Jasna Vujin, **Tijana Tomašević‑Ilić**, Marko Spasenović and Radoš Gajić, DFT study of optical properties of MoS2 and WS2 compared to spectroscopic results on liquid phase exfoliated nanoflakes, Optical and Quantum Electronics 50 (2018) 291.
5. S. Djurić, G. Kitić, J. Dubourg, R. Gajić, **T. Tomašević-Ilić**, V. Minić and M. Spasenović, Miniature graphene-based supercapacitors fabricated by laser ablation, Microelectronic Engineering 182 (2017) 1-7.
6. **Tijana Tomašević-Ilić**, Jelena Pešić, Ivana Milošević, Jasna Vujin, Aleksandar Matković, Marko Spasenović and Radoš Gajić, Transparent and conductive films from liquid phase exfoliated graphene, Optical and Quantum Electronics 48 (2016) 319.

Саопштење са међународног скупа штампано у изводу (М34)

1. Djordje Jovanović, **Tijana Tomašević-Ilić**, Nikola Tasić, Aleksandar Matković, Marko Spasenović and Radoš Gajić, Emmanuel Kymakis, Silicon going indoors, NanoBio 2018, 24-28 September, 2018, Heraclion, Crete.
2. **Tijana Tomašević-Ilić**, Aleksandar Matković, Jasna Vujin, Radmila Panajotović, Marko Spasenović and Radoš Gajić, P-type field-effect transistors based on liquid phase exfoliated MoS2, Graphene 2017, 28-31 March, 2017, Barcelona, Spain.
3. **T. Tomašević-Ilić**, Dj. Jovanović, J. Pešić, A. Matković, M. Spasenović and R. Gajić, Enhancing conductivity of self-assembled transparent graphene films with UV/Ozone Treatment, Photonica 2017, 28. Aug - 1. Sep, 2017, Belgrade, Serbia.

4. J. Pešić, J. Vujin, **T. Tomašević-Ilić**, M. Spasenović and R. Gajić, Ab-initio study of optical properties of MoS2 and WS2 compared to spectroscopic results of liquid phase exfoliated nanoflakes, Photonica 2017, Aug - 1. Sep, 2017, Belgrade, Serbia.
5. T. Szabó, J. Vujin, **T. Tomaševic**, R. Panajotović, A. E. Sarrai, Sz. Zsolt, G. Váró, K. Hajdu, M. Botond, K. Hernádi and L. Nagy, Posiible applications of carbon based bio-nanocomposites in optoelectronics, XXVIst Congress of the Hungarian Biophysical Society, August 22-25 2017, Szeged, p.54.
6. T. Szabó, **T. Tomaševic**, R. Panajotović, J. Vujin, A. E. Sarrai, G. Váró, Zs. Szegletes, G. Garab, K. Hajdu and L. Nagy, Photosynthetic reaction-center/graphene biohybrid for optoelectronics, 5th International Conference on Biosensing Technology, 7-10 May 2017, Riva del Garda, Italy, p.121.
7. Marko Spasenović, **Tijana Tomašević-Ilić**, Aleksandar Matković and Radoš Gajić, Transparent and Conductive Films From Liquid Phase Exfoliated Graphene, EuroScience Open Forum – ESOF 2016, 24-27 July 2016, Manchester, United Kingdom, p. 40-41.
8. Djordje Jovanović, **Tijana Tomašević**, Aleksandar Matković, Nikola Tasić and Rados Gajić, Low light solar cells, 13th International Conference on Nanosciences and Nanotechnologies, NN16, 5-8 July 2016, Thessaloniki, Greece, p.289.
9. D. Jovanović, **T. Tomašević**, A. Matković, M. Musić, N. Tasić, M. Spasenović and R. Gajić, Low light low cost solar cells, 3rd International School and Conference on Optoelectronics, Photonics, Engineering and Nanostructures, Saint Petersburg OPEN 2016, 28 – 30 March 2016, St Petersburg, Russia, p.205.
10. **T. Tomašević-Ilić**, J. Pešić, I. Milošević, J. Vujin, A. Matković, M. Spasenović and R. Gajić, Transparent and conductive films from liquid phase exfoliated graphene, the Fifth international school and conference on photonics, Photonica 2015, 24-28 August 2015, Belgrade, Serbia, p.191.
11. A. Matković, I. Milošević, M. Milićević, **T. Tomašević-Ilić**, J. Pešić, M. Musić, M. Spasenović, Dj. Jovanović, B. Vasić, M. R. Belić and R. Gajić, Chemical Doping of Langmuir-Blodgett Assembled Graphene Films for Flexible Transparent Conductive Electrodes, the 19th Symposium on Condensed Matter Physics - SFKM 2015, 7 – 11 September 2015, Belgrade, Serbia, p.93.

Предавање по позиву са међународног скупа штампано у изводу izvodu (М32)

12. A. Matković, I. Milošević, M. Milićević, A. Beltaos, **T. Tomašević-Ilić**, J. Pešić, M. M. Jakovljević, M. Musić, U. Ralević, M. Spasenović, Dj. Jovanović, B. Vasić, G. Isić and R. Gajić, Spectroscopic and Scanning Probe Microscopic Investigations and Characterization of Graphene, the 19th Symposium on Condensed Matter Physics - SFKM 2015, 7 – 11 September 2015, Belgrade, Serbia, p.32.

Full Length Article

Reducing sheet resistance of self-assembled transparent graphene films by defect patching and doping with UV/ozone treatment

Tijana Tomašević-Ilić[a,*], Đorđe Jovanović[a], Igor Popov[a,b], Rajveer Fandan[c], Jorge Pedrós[c], Marko Spasenović[a], Radoš Gajić[a]

[a] Graphene Laboratory (GLAB) of the Center for Solid State Physics and New Materials, Institute of Physics, University of Belgrade, Pregrevica 118, 11080 Belgrade, Serbia
[b] Institute for Multidisciplinary Research, University of Belgrade, Kneza Višeslava 1, 11030 Belgrade, Serbia
[c] Departamento de Ingeniería Electrónica and Instituto de Sistemas Optoelectrónicos y Microtecnología, Universidad Politécnica de Madrid, Madrid 28040, Spain

ABSTRACT

Liquid phase exfoliation followed by Langmuir-Blodgett self-assembly (LBSA) is a promising method for scalable production of thin graphene films for transparent conductor applications. However, monolayer assembly into thin films often induces a high density of defects, resulting in a large sheet resistance that hinders practical use. We introduce UV/ozone as a novel photochemical treatment that reduces sheet resistance of LBSA graphene threefold, while preserving the high optical transparency. The effect of such treatment on our films is opposite to the effect it has on mechanically exfoliated or CVD films, where UV/ozone creates additional defects in the graphene plane, increasing sheet resistance. Raman scattering shows that exposure to UV/ozone reduces the defect density in LBSA graphene, where edges are the dominant defect type. FTIR spectroscopy indicates binding of oxygen to the graphene lattice during exposure to ozone. In addition, work function measurements reveal that the treatment dopes the LBSA film, making it more conductive. Such defect patching paired with doping leads to an accessible way of improving the transparent conductor performance of LBSA graphene, making solution-processed thin films a candidate for industrial use.

1. Introduction

Graphene, with its high optical transparency and low sheet resistance, is an excellent choice for transparent electrodes in various optoelectronic devices [1]. For such applications, transparency in the visible part of the spectrum should be above 80%, while the sheet resistance should be low enough for practical use, all while keeping production costs to a minimum. In the past decade, numerous research efforts were performed to achieve production of thin graphene films usable in practical applications [2–4]. Although chemical vapor deposition (CVD) yields graphene sheets of high quality that can be scaled for industrial use [5], the method is generally regarded as costly [6] and alternative methods are being sought that satisfy the quality/cost tradeoff. Liquid phase exfoliation (LPE) [7] is the most perspective way of obtaining large quantities of exfoliated graphite in solution at reasonable production costs. Nevertheless, all solution-processed graphene needs to be controllably assembled into thin films of satisfactory quality for transparent conductor applications. A number of film assembly strategies exist, such as evaporation-based assembly, assisted, and micropatterned assembly [8]. Each specific thickness and arrangement of

graphene sheets in a thin film directly affects physical properties of the film [9] and device performance. Langmuir-Blodgett (LB) and Langmuir-Schaefer (LS) deposition, based on surface-tension induced self-assembly of nanoplatelets at an interface of two liquids or a gas and a liquid, are prime candidate methods for production of large-scale, highly transparent thin graphene films [10,11]. However, all self-assembled films suffer from a large density of defects that often leads to a high sheet resistance of deposited film. Conversely, the large defect density offers an opportunity for surface treatment such as annealing, chemical doping and functionalization [3,12], all of which can reduce sheet resistance or produce other desirable effects. The susceptibility of a film to treatment as well as its initial sheet resistance depend on the nature of the prevalent defects, such as impurities, vacancies, nanoplatelet edges, and topological defects, as well as the defect density. For example atoms located at the edges of a graphene sheet exhibit higher reactivity compared to those in the basal plane, making the ratio of the density of edge atoms to basal-plane atoms the determining factor for the efficiency of surface modification [13]. It is thus imperative to carefully study the nature and density of defects in any thin film transparent conductor, especially when considering physical or

---

* Corresponding author.
  E-mail address: ttijana@ipb.ac.rs (T. Tomašević-Ilić).

chemical treatment to enhance the film's practical usability.

Here, we report characterization of the defect type of Langmuir-Blodgett self-assembled (LBSA) films from LPE graphene and subsequent defect patching with UV/ozone (UVO) treatment. We observe the effects that photochemical oxidation has on our films exposed to ozone, a very important gas adsorbate that significantly alters the properties of materials through doping, affecting the performance of electronic devices [14–16]. As shown earlier, oxidation spreads from edges inwards across the entire surface of graphene flakes [17]. When applied even for a short time to mechanically exfoliated and monolayer CVD graphene, UVO leads to significant defect generation resulting in an increase of sheet resistance [18,19]. Ozone reacts with the edge sites of CVD graphene until reaching a saturation point. Beyond saturation, the basal plane becomes more susceptible to oxidation, resulting in the replacement and relief of carbon atom defects. We find that nanoplatelet edges are the dominant defect type in our films, in contrast to CVD-grown graphene and earlier reported mechanically exfoliated graphene, where charged impurities and covalently bonded adatoms are the limiting factor for carrier mobility [20]. We treat the film surface with UVO and find that the sheet resistance decreases by a factor of 3, while optical transparency throughout the visible part of the spectrum remains high ($> 80\%$) and virtually unchanged. Measurements of the surface work function indicate that doping is responsible for the decrease in sheet resistance. FTIR spectroscopy confirms formation of oxygen-containing groups after UVO treatment. With a careful analysis of Raman spectra, we find that the density of defects decreases with treatment, yielding an increase in the carrier mean free path, while edges remain the dominant defect type, all indicating that the ozone binds predominantly to the edges of graphene nanoplatelets. We perform the same UVO treatment on CVD graphene and show that on monolayer CVD graphene, UVO has a detrimental effect on sheet resistance. We also treat thick CVD-grown multilayer graphene films, which prove to be robust against UVO treatment, although such films have very low optical transparency. Furthermore, in order to understand the experimental results we theoretically analyze deposition of an ozone molecule on the edges of a wide graphene nanoribbon (GNR) as a nanosystem that well approximates LBSA film. After we determine the deposition mechanism, we present electronic and transport properties of such oxidized ribbons. Hence, transport and work function measurements indicate increased film doping, AFM indicates that no major macroscopically observable morphological changes are made on the film, Raman resolutely points to edge patching as the dominant interaction mechanism, while FTIR shows that oxygen binding to the graphene lattice occurs during treatment. Our experimental study is firmly backed by ab-initio calculations that indicate that ozone species binding to edges will increase film conductivity. We thus conclude that UVO treatment is a good option for reducing sheet resistance of LBSA LPE graphene films, bringing the electronic performance of these sheets closer to that of CVD graphene which is produced at a higher cost.

2. Methods

A graphene dispersion was prepared from graphite powder (Sigma Aldrich, product no. 332461) from a concentration of $18 \, \text{mg ml}^{-1}$ in N-Methyl-2-pyrrolidone (NMP, Sigma Aldrich, product no. 328634), exposed to 14 h of sonication in a low-power sonic bath. The resulting dispersion was centrifuged for 60 min at 3000 rpm in order to reduce the concentration of unexfoliated graphite. The resulting dispersions were used to form films approximately 3 nm thick by LBSA, in the same way that we demonstrated in our previous work [12,21]. A small amount of graphene dispersion is added to a water-air interface and after the film is formed, it is slowly scooped onto the target substrate (Fig. 1a). Glass and SiO_2/Si are used as substrates.

For single-layer CVD studies, we used commercially available monolayer CVD graphene grown on 20 μm thick copper foil (Graphene Supermarket) and transferred onto SiO_2/Si substrate with a home-built automatic transfer system using ammonium persulfate $((NH_4)_2S_2O_8)$ 0.3 M as copper etchant [22]. For multilayer CVD studies, we used multilayer graphene with an average thickness of 105 nm (about 300 monolayers) grown on 25 μm-thick nickel foil (Graphene Supermarket). We etched away the nickel foil in a 0.25 M solution of ferric chloride $(FeCl_3)$ in water, yielding a floating multilayer graphene film which was scooped out of the solution onto a SiO_2/Si substrate in the same way as already reported for multilayer graphene condenser microphones [23].

Photochemical oxidation (UVO treatment) is performed by exposing the graphene films to ultraviolet radiation and ozone for 3, 5, 15 and 30 min at a 50 °C chamber temperature and ambient pressure in a Novascan UV/ozone Cleaner by converting oxygen from ambient air to ozone using a high intensity mercury lamp (Fig. 1b). We perform the treatment in a standard commercially available UVO cleaner and acknowledge that while varying the intensity of the radiation and/or the concentration of ozone gas may lead to interesting results, it will be part of a subsequent study.

For optical characterization, UV–VIS spectra were taken using a Perkin-Elmer Lambda 4B UV/VIS Spectrophotometer. The oxidation process was characterized using a TriVista 557 S&I GmbH Micro Raman spectrometer ($\lambda = 532$ nm) at room temperature. FTIR spectra were measured with a Thermo Scientific Nicolet 6700 FT-IR spectrometer in the diffuse reflectance infrared Fourier transform (DRIFT) mode. The resistance of each sample was measured in a two-point probe configuration and the sheet resistance was obtained by considering sample geometry factors. The work function measurement is performed with Kelvin probe force microscopy (KPFM, NTEGRA Spectra), prior to and after photochemical treatment of our graphene films.

The calculations are done using density functional-based tight binding method (DFTB) [24,25] with self-consistent charge correction as implemented in the DFTB+ code [26]. Spin polarization was included in calculations. This method has a proven record of various applications to graphene and graphene nanoribbons [27–30]. Transport properties are calculated by DFTB augmented with the Green's functions formalism [31]. Since the atomic structure of LBSA graphene is dominated by edges, we consider GNR a suitable nanosystem that well approximates the nanoflakes in our experiment. For this purpose we model a wide GNR with width 2 nm. The interaction between electronic clouds of two GNR edges is small for such a wide ribbon, hence its electronic properties are equal to the asymptotic limit of wide ribbons
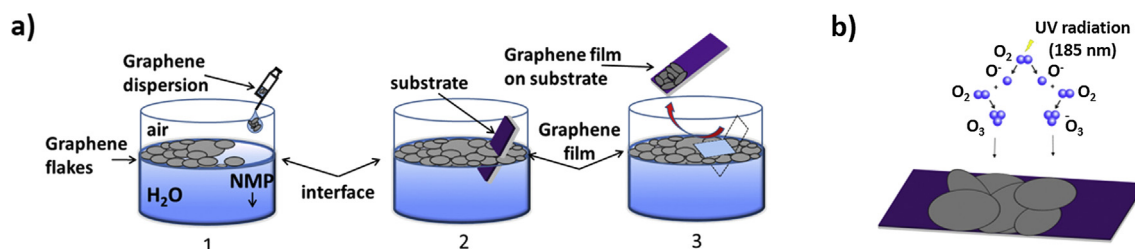
Fig. 1. (a) Schematic of Langmuir-Blodgett self-assembly (LBSA) on a water-air interface (1: film formation, 2: substrate immersion, 3: film deposition), NMP is N-Methyl-2-pyrrolidone; (b) Schematic of film exposure to photochemical oxidation.
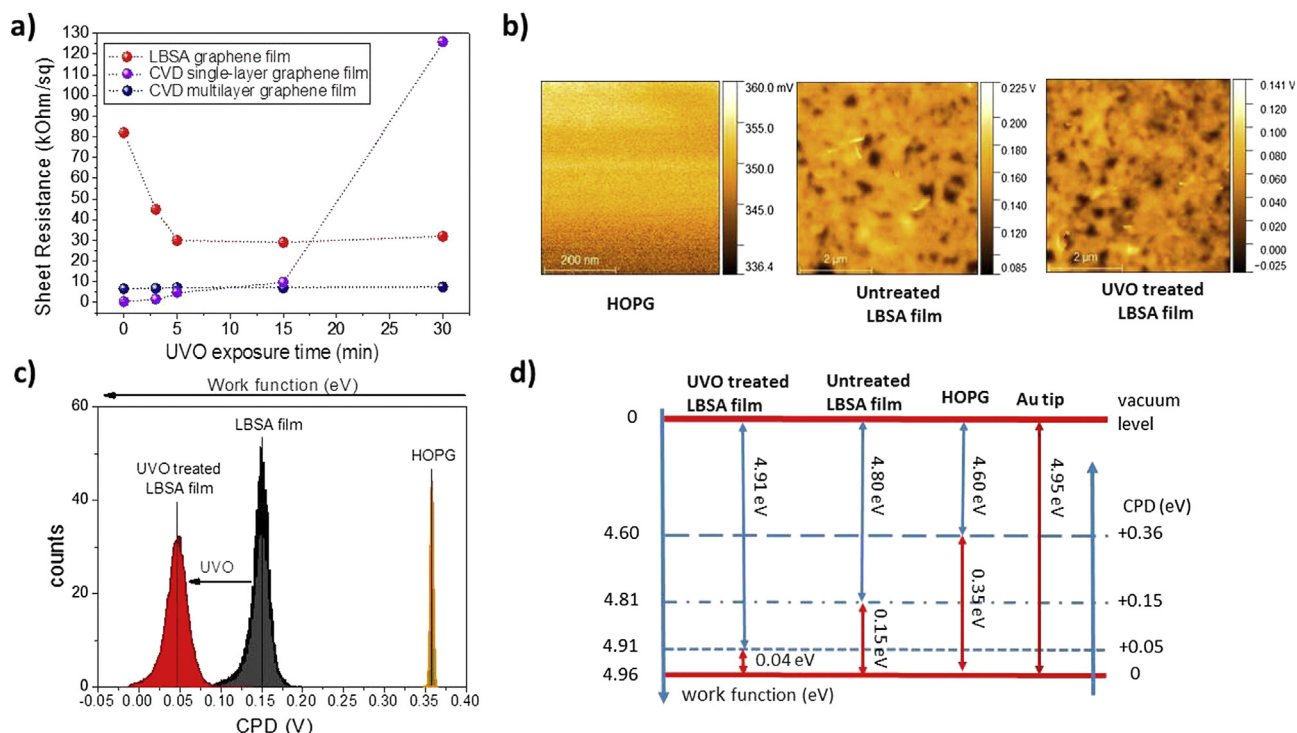
Fig. 2. (a) Sheet resistance of LBSA, CVD-grown single- and multilayer graphene films as a function of UVO exposure time, (b) KPFM map of HOPG, untreated, and UVO treated LBSA film, (c) KPFM histograms of LBSA graphene film before (grey) and after (red) UVO treatment, (c) Schematic of the relation between measured CPDs and their corresponding work functions.

[32]. The periodic (infinite) edges of GNR correspond to the flakes in the experiment, which have large circumferences, i.e. long edges. Utilization of GNR instead of nanoflakes per se is not only physically equivalent but also numerically much more tractable.

3. Results and discussion

Fig. 2a depicts the sheet resistance of graphene films upon exposure to UVO. Prior to exposure, the sheet resistance of LBSA graphene (red circles) is above 80 kΩ/sq. Upon exposure, the sheet resistance decreases rapidly within the first 5 min, reaching a value below 30 kΩ/sq, an approximately 3-fold reduction. At those exposure levels, oxidation reaches a saturation point and remains stable for longer exposure times. Single layer CVD graphene exhibits a pronouncedly different behavior (violet circles), starting from a very low value of sheet resistance which gently rises after 5 mins of exposure, dramatically increasing for longer exposures. After 15 min of treatment, sheet resistance of CVD graphene is still 3–4 times smaller than that of LBSA graphene, whereas after 30 min of exposure LBSA graphene exhibits 4 times smaller sheet resistance. Multilayer CVD graphene (blue circles) has a sheet resistance

of ~8 kΩ/sq, which changes only slightly even for long exposures to UVO.

It is expected that CVD graphene compared to LBSA graphene boasts a lower sheet resistance, which is inherently related to carrier mobility. Carrier mobility is inversely proportional to the density of scattering defects, which should be small in CVD graphene. LBSA graphene morphology has an abundancy of nanoplatelet edges [21] that act as scattering centers and have a detrimental effect on initial sheet resistance. However, with UVO treatment, that resistance decreases, pointing to a reaction of ozone with existing defects [17]. On CVD graphene, the few edge sites are quickly fully saturated by ozone molecules, forcing the molecules to deposit their energy by formation of defects or through adsorption, thus creating new point defects on the basal plane, having a detrimental effect on sheet resistance [19]. In multilayer graphene, UVO has little effect on sheet resistance because the ozone molecules react with the top layers only, whereas charge transport takes place through the entire volume of the sheet.

To examine the origins of decreasing sheet resistance with UVO treatment, we measure the surface work function (WF) with KPFM. Fig. 2b depicts KPFM maps of the contact potential difference (CPD)
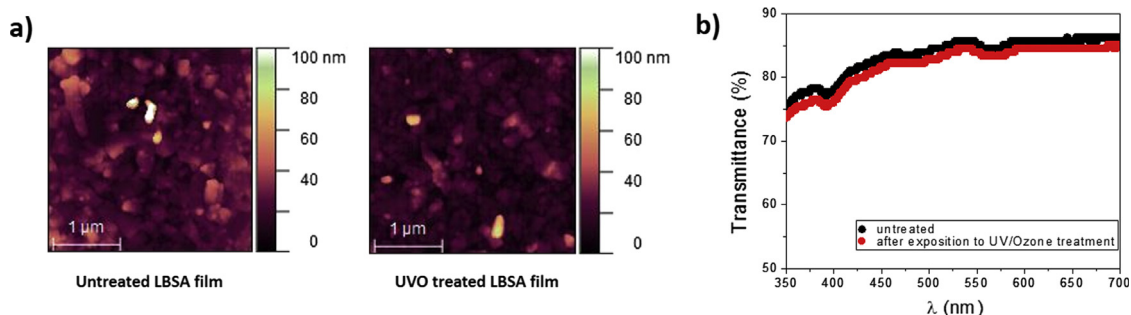
Fig. 3. (a) 3 × 3 μm² topograph of HOPG, untreated, and UVO treated LBSA film, (b) Transmittance of a LBSA graphene film in the visible range on a glass substrate, before (black) and after (red) 5 min exposure to UVO.

between the sample and the tip, before and after UVO exposure. Note the different colormap scale, that indicates a lower CPD between the sample and the metallized AFM tip for treated samples compared to untreated samples. To measure the absolute value of the WF, we use as a reference the work function of highly ordered pyrolytic graphite (HOPG), a tabulated value of 4.6 eV [33,34]. In order to determine the average CPD of the measured surface, histograms of KPFM maps were used and fitted to a Gaussian distribution (Fig. 2c). The mean WFs of the tip, HOPG, untreated, and treated films are plotted against the vacuum level in Fig. 2d. The exact procedure is detailed in our previous work [21]. It is evident that UVO increases the WF from 4.8 eV to 4.9 eV, shifting the Fermi level downwards by ∼100 meV. It is this additional UVO-induced p-doping that leads to an increased carrier concentration, in turn causing decreased sheet resistance [35].

Aside from improving the sheet resistance, for transparent conductor applications it is important that the optical transparency of the treated film remains high. Fig. 3a depicts AFM topography of the same areas of the film that were used to measure the WF. No difference is observed in the film morphology as an effect of UVO exposure. Fig. 3b depicts the transmittance spectrum of the pristine and treated UVO film. The film has good transparency throughout the visible part of the spectrum, with 80–85% transmittance. The transmittance of the film is barely affected by the treatment. For comparison, monolayer CVD would have transmittance on the order of ∼97%, whereas multilayer CVD transmits under 10% of light in the visible, according to manufacturer specifications. Hence, single layer CVD graphene has the overall best performance for transparent conductor applications, although cost remains a limiting factor for wide-scale use, whereas multilayer CVD has little use for such applications due to its low transparency. LBSA graphene holds the middle ground, with acceptable electronic and optical performance (especially after UVO treatment) with projected low costs of fabrication and good scalability. It is important to note that the unchanged transparency coupled with a reduced sheet resistance leads to a threefold increase in the figure of merit (FOM) for transparent conductor applications [36].

Fig. 4 shows FTIR spectra for untreated and UVO treated films. It is clear that the intensities of peaks associated with oxygen-containing groups increase after UVO exposure. We distinguish a change in shape and total peak area of a broad band in the 3000–3700 cm^{-1} region after UVO treatment, corresponding to the presence of hydroxyl and carboxyl groups as well as water. Also, a peak appears at 1825 cm^{-1} after 30 min of UVO exposure indicating the formation of interacting oxygen groups (OH and C=O). Another evident change after 30 min of exposure occurs near 800 cm^{-1}, in a spectral region associated to the formation of epoxides (C−O−C) at graphene edges, according to a previous report [37]. The overlapping spectral features of ethers, epoxides, carboxyles and hydroxyl groups complicate spectral interpretation in the 1000–1300 cm^{-1} region where there is a strong SiO$_2$ absorption band.

The opposite effect that UVO has on CVD and LBSA graphene demands an inquiry into the effect of reactive site morphology on reactions with ozone. LBSA graphene morphology is dominated by nanoplatelet edge defects, whereas CVD yields graphene that has a few edges, in which chemical reactions should be governed by point defects such as charged impurities and covalently bonded adatoms [36]. To clarify the nature of reactive defects and their evolution during UVO treatment, we apply Raman spectroscopy, a versatile tool for characterization of graphene-based materials [38].

Fig. 5a depicts Raman spectra of LBSA graphene as a function of UVO exposure. The spectra feature four pronounced bands: D at ∼1343 cm^{-1}, G at ∼1579 cm^{-1}, D' at ∼1614 cm^{-1} and the 2D band at ∼2694 cm^{-1}. Furthermore, several combinations of these bands are also observed: D + D" at ∼2450 cm^{-1} and D + D' at ∼2935 cm^{-1} (Fig. 5b), where D" is signature of a phonon belonging to the LA branch, typically observed at ∼1100 cm^{-1} [39]. The D and G bands are well resolved for all samples. The 2D peak is a typical signal arising in multilayer graphene. However, Raman spectra show evident changes of the intensity of the D mode with UVO exposure. Fig. 5c depicts the ratio
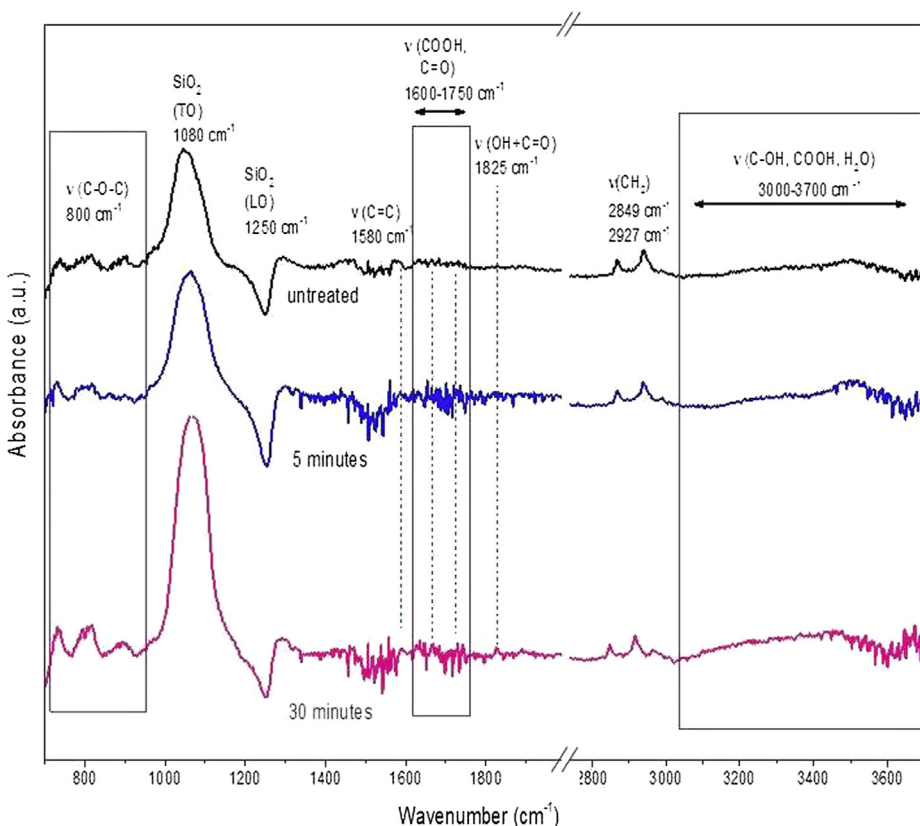
Fig. 4. Reflection infrared spectra of untreated (black), 5 min (blue) and 30 min (pink) UVO exposed LBSA graphene films. We indicate vibrational modes for hydroxyls (possible C−OH, COOH and H$_2$O contributions) at 3000–3700 cm^{-1}, carbonyl (C=O) and carboxyls (COOH) at 1600–1750 cm^{-1}, sp^2-hybridized (C=C) at 1580 cm^{-1} and epoxides (C−O−C) at 800 cm^{-1}. Vibrational modes of SiO$_2$ (LO and TO) appear at 1250 and 1080 cm^{-1}, respectively. The areas marked with rectangles are regions in which the most prominent spectral changes occur after UVO exposure.
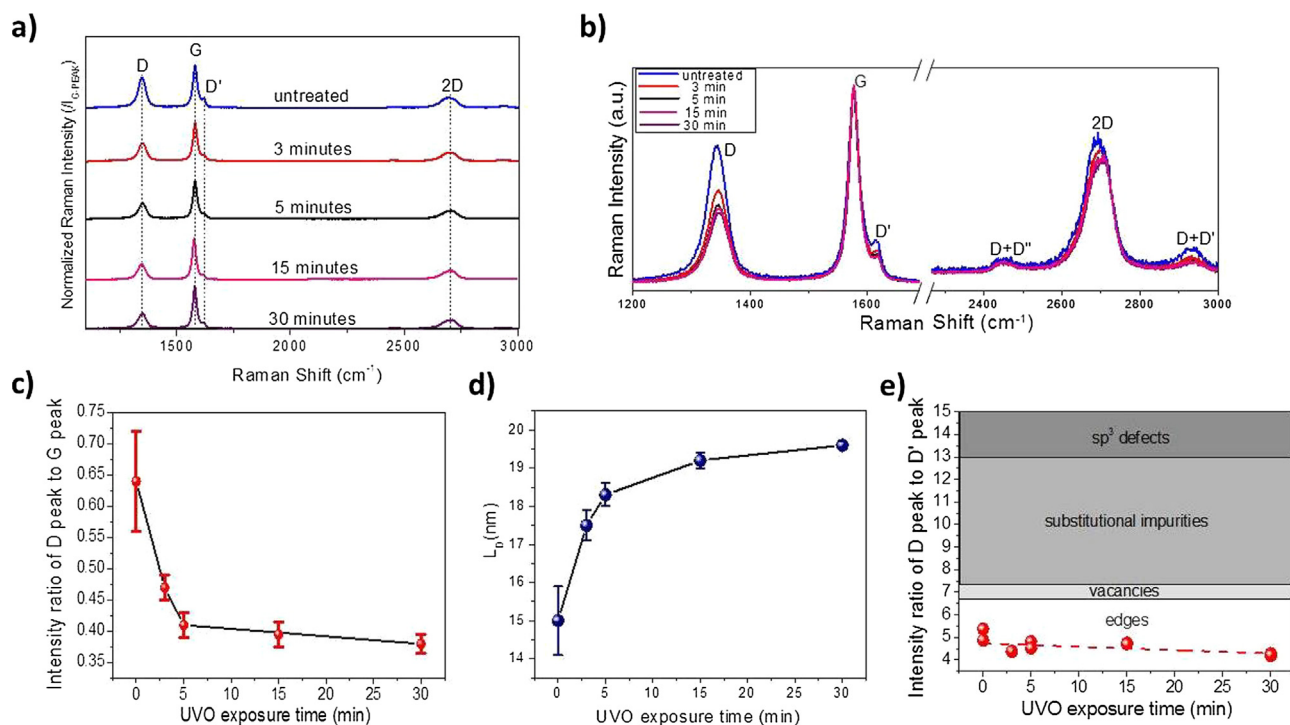
Fig. 5. (a) Representative Raman spectra of LBSA graphene as a function of UVO exposure time. We recorded Raman spectra in various regions to eliminate spot-to-spot variations in the obtained spectra. The spectra show four main bands: D, G, D', and 2D, as well as some weak combinations of these modes. (b) Close-up view of the main bands, (c) The D/G intensity ratio of the films as a function of UVO exposure. The D/G ratio is calculated from integrated peak areas. (d) Interdefect distance as a function of UVO exposure time. The error bar represents the standard deviation of five measurements, (e) The D/D' ratio as a function of UVO exposure time.

of the D peak to the G peak calculated from integrated peak areas, often used to monitor defect evolution in graphene. We observe a large decrease of this ratio during UVO exposure, indicating a reduction in defect density. The D/G intensity ratio evolution shows the same trend as sheet resistance, with a rapid change within the first 5 min of exposure, followed by saturation. The reduction of defect density with UVO exposure in LBSA graphene is opposite from our results on CVD graphene (Figs. S1 and S2) and the literature on monolayer graphene [12,13]. LBSA graphene thus responds in a unique way to an oxidizing environment, with ozone binding to existing defects leading to improved electrical performance.

Supplementary data associated with this article can be found, in the online version, at https://doi.org/10.1016/j.apsusc.2018.07.111.

The ratio I_D/I_G can be converted to the carrier mean free path (L_D), as long as the laser wavelength is known [40]:

$$L_D^2 (nm)^2 = (1.8 \pm 0.5) \times 10^{-9} \lambda_L^4 \left(\frac{I_D}{I_G} \right)^{-1}$$

(1)

For the wavelength used in this study (λ_L = 532 nm), we plot L_D as a function of exposure time in Fig. 5d. L_D in LBSA graphene increases from 15 nm to 19.5 nm upon UVO exposure, again indicating defect patching. Before and after exposure, the mean free path is smaller than our average flake diameter (previously reported as 120 nm [21]), which points to defects within the nanoplatelets, either through edges of sheets that are stacked on top of each other, or through other point-like defects that we cannot observe with AFM and SEM.

Possible defects in graphene include topological defects (such as pentagon-heptagon pairs), boundaries, vacancies, substitutional impurities, and sp³ defects [41]. Topological defects have the lowest formation energy [41], and they are always present in LPE graphene sheets as a result of the cavitation process [42]. As the ratio between the intensity of the D and the D' mode is very sensitive to the type of defect, with a value of 3.5 for edges, 7 for vacancies, between 7 and 13 for substitutional impurities, and 13 for sp³ defects [43,44], we measure

this value to deduce the nature of defects in our sample. We observe that the ratio of the D-peak intensity to the D'-peak intensity in our films is nearly constant at a value of 4.8 ± 0.5, regardless of UVO exposure. The measured ratio indicates that edges are the dominant defect type in our films, ruling out vacancies, substitutional impurities, and sp³ defects, in agreement with previously published data for LPE graphene [42]. There is little change in defect type with photochemical oxidation (Fig. 5e), although the defect density decreases, indicating that ozone most likely reacts with the existing defects and patches them.

In LBSA graphene, flakes may bundle in stacks with varying thickness and lateral dimensions, edge geometries with varying saturation levels (bound oxygen, hydrogen, or other chemical groups), and a wide variety of possible defects. From these virtually infinite possibilities, for our DFTB + calculation we choose an example of a GNR with bare zigzag edges and with width of 2 nm. Electronic properties of graphene depend sensitively on physical and chemical modification of edges [45–47]. It was shown that roughness at zig-zag edges does not significantly influence their conductance in contrast to armchair edges [48–50]. The simple choice of a zig-zag GNR is for demonstration purpose only, i.e. to uncover the basic physics of the experimental results, without intent to cover all aspects of the experimental reality. The initial atomic structure consists of the GNR with an ozone molecule placed parallel to the edge. After geometry optimization of the system we obtained a transition configuration (TC) using the dimer method [51]. Optimization of the TC geometry led to the next (meta)stable geometry. The nudged elastic band (NEB) method [52,53] is used for evaluation of the potential barrier between the configurations. Using this procedure we obtained three (meta)stable configurations. The reaction is presented in Fig. 6a and b. Firstly, one of the two O-O bonds in O₃ breaks, which is followed by a rotation of the O−O dimer around a C−C axis by 180°, as illustrated with the insets in Fig. 6a. The product of the reaction is the GNR edge with three separate O adatoms at the nearest sites of the edge (the configuration will be called 3O in the
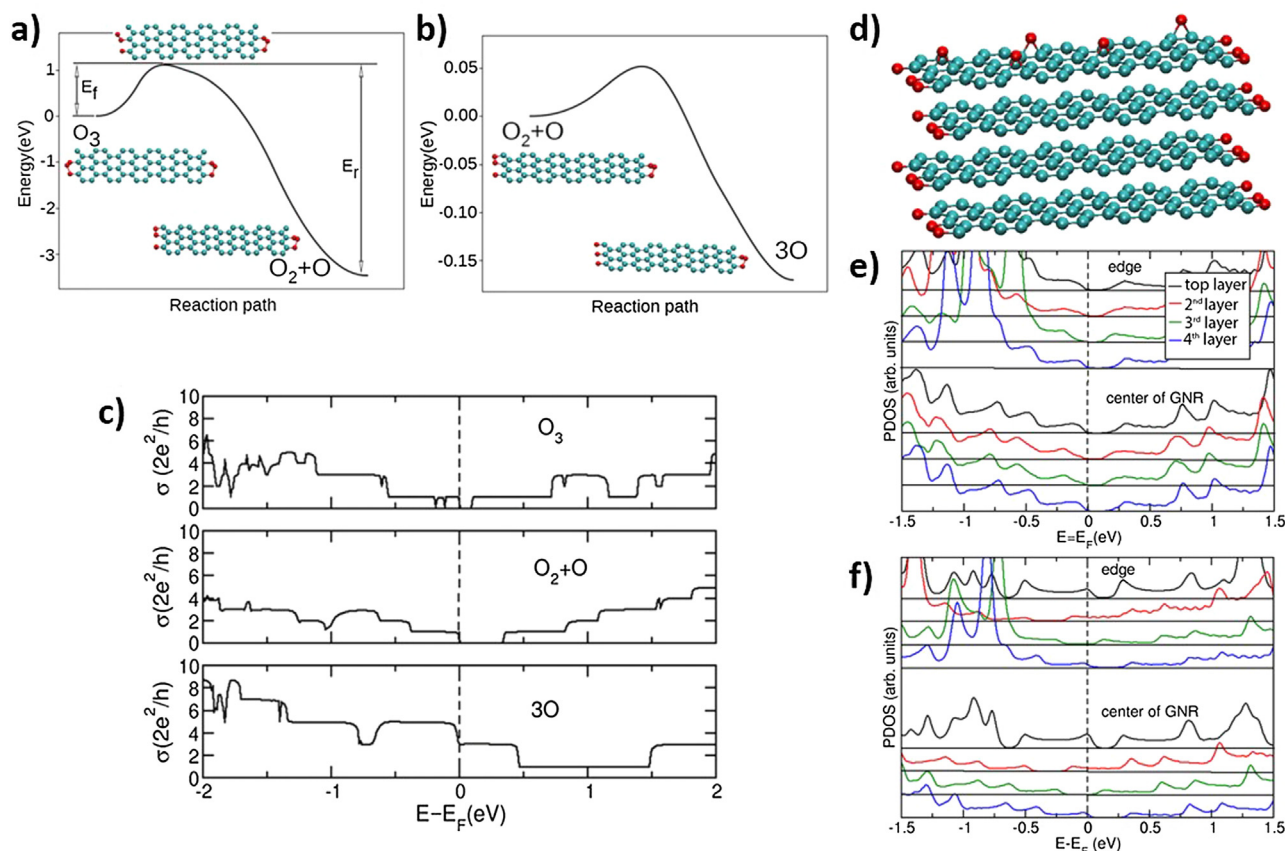
Fig. 6. (a) and (b) Potential energy surface of the cascaded reaction of an O_3 molecule with a GNR zig-zag edge (O_3 configuration). Breaking of an O—O bond in the ozone molecule and rotation of O—O dimer about C-O dimer (transition state), which settles the intermediate (3O) state, are shown in (a). The consequent association of two neighboring O atoms, yielding the O_2 + O configuration, is presented in (b). The reaction is analyzed only on one edge (the left edge in the insets). (c) Conductance at zero bias of the GNR with the three configurations. (d) Illustration of the stack with four layers of GNRs with O_2 + O edge configuration doped in-plane by five oxygen atoms. Projected density of states of the stack without (e) and with (f) in-plane doping. Panels (e) and (f) distinguish contributions to PDOS from GNR edges and lines of central carbon atoms.

remaining text). The potential barrier for the reaction is $E_f = 1.11$ eV, while the energy for the reverse reaction is $E_r = 4.58$ eV. At a temperature of 50 °C, which was used in our experiment, both forward and reverse reactions are impossible. However, the exposure of the sample to UV radiation may assist the reaction. The forward reaction is exothermic with $\Delta E = -3.47$ eV. Two of the three O atoms attached at the edge can associate into an O_2 molecule, as indicated in Fig. 6b. The potential barrier is much smaller in this case, being only $E_f = 0.05$ eV. The reverse reaction is also viable with $E_r = 0.22$ eV. The reaction is exothermic as well, with $\Delta E = -0.17$ eV. The final product of the cascaded reaction consisting of an O_2 molecule and an adatom at the GNR edge will be designated as O_2 + O configuration in following text. Therefore both configurations, O_2 + O and 3O, being nearly iso-energetic, can coexist at the same time. The reaction is somewhat different from the one obtained in [54], but it is expected since the paper considered zig-zag edges in a small hydrogenated carbon cluster in contrast to the infinite ribbon without edge saturation that we consider.

The conductance of the three configurations (the initial O_3 and the two reaction products O_2 + O and 3O) is shown in Fig. 6c. While a pristine zig-zag GNR (not shown in the figure) does not have an electronic band gap, a gap opens upon deposition of O_3 at a GNR edge. We set the Fermi level (E_F) to the top of the valence band in the initial O_3 and O_2 + O configurations. The electronic gaps are around 0.10 eV and 0.35 eV, respectively, whereas the conductance at E_F is one quantum for both cases. This corresponds to a sheet resistance of 12.9 kΩ. Breaking of the O—O bond in the O_2 + O configuration causes a significantly different conductance. The 3O configuration does not exhibit a gap,

while the conductance is increased by a factor of 3 or 5, since E_F is positioned at the border of regions with two distinct conductance values. The 3- to 5-fold increase of conductance of a free-standing GNR indicates a possible mechanism of decreasing sheet resistance in our experiment. Note that there is not a one-to-one correspondence between experiment and theory as transport through LBSA graphene is more complex, involving stacks of GNRs with a variety of edges, and transport between stacks which is perhaps based on quantum tunneling. However the increase of conductance is in positive correlation with our experiments. All configurations exhibit p-type doping, in agreement with experiment.

A complete analysis of electronic properties of stacks of flakes (or GNRs) would require consideration of flakes with numerous combinations of edge structures, physical dimensions of flakes and their different mutual orientations, varying number of GNRs in stacks. After obtaining the conductance inside and between stacks a set of stacks could be modeled with an equivalent electrical circuit and their resistance calculated. This comprehensive study will be published elsewhere. Here, for demonstration only, we opt for a single structure, a Bernal stacking of four GNRs with an O_2 + O edge configuration as shown in Fig. 6d. We compare projected density of states (PDOS) of the stack in the plane of the top layer, without and with oxidation in Fig. 6e and f, respectively. The O adatoms responsible for the in-plane oxidation make epoxy groups as found previously in [55]. Upper four sub-graphs in each panel represent PDOS at the GNR edge, while the lower four sub-graphs show PDOS at the center of GNR. Colors of the graphs distinguish four GNRs in the stack (named layers in Fig. 5e and f). Both

edges and the middle of GNRs contribute to PDOS in the range from E_F – 0.5 eV to E_F + 0.5 eV. Edges have much larger contributions for energies below E_F – 0.5 eV, hence conductance is expected to be dominated by edges for a bias voltage larger than ~1 V. The stack without in-plane oxidation exhibits a uniform PDOS among layers, with E_F positioned at the top of the valence band. In contrast, the oxidation of the top layer alternatively dopes the layers with p and n character. Since PDOS at E_F is non-zero in three out of four layers, we expect a much larger low-bias conductance of the in-plane oxidized stack than the one without in-plane oxidation. Note that the transport properties analyzed in this section are applicable only to the plane parallel to GNRs in the stack. The conductance in the perpendicular direction has a tunneling character, with expected much larger electric resistance.

4. Conclusion

In contrast to the degrading effects it has on CVD graphene, photochemical oxidation (UV/ozone treatment) of LBSA graphene leads to a decrease in defect density, which together with doping reduces sheet resistance while retaining high optical transparency. We find that edges are the dominant defect type in LBSA graphene, with little influence of other defects such as vacancies, impurities, or sp^3 defects that are common limiting factors for electronic performance of CVD and mechanically exfoliated graphene. Our study thus shows that graphene film morphology and defect landscape play a crucial role in the effect that UV/ozone treatment has on the film. This accessible treatment improves the performance of LBSA graphene, which is key to embedding such materials in durable devices especially those involving direct exposure to ultraviolet radiation and ozone gas. Our novel observation is expected to contribute to the technological acceptance of thin films based on solution-processed 2D materials.

Acknowledgments

References

[1] F. Bonaccorso, Z. Sun, T. Hasan, A.C. Ferrari, Graphene photonics and optoelectronics, Nat. Photonics 4 (2010) 611–622.

[2] W. Ren, H.M. Cheng, The global growth of graphene, Nat. Nanotech. 9 (2014) 726–730.

[3] Q. Zheng, J.-K. Kim, Graphene for Transparent Conductors: Synthesis, Properties and Applications, Springer, New York, 2015.

[4] I. Banerjee, T. Faris, Z. Stoeva, P.G. Harris, J. Chen, A.K. Sharma, A.K. Ray, Graphene films printable on flexible substrates for sensor applications, 2D Mater. 4 (2017) 015036.

[5] T. Kobayashi, et al., Production of a 100-m-long high-quality graphene transparent conductive film by roll-to-roll chemical vapor deposition and transfer process, Appl. Phys. Lett. 102 (2013) 023112.

[6] E.L. Wolf, Practical Productions of Graphene, Supply and Cost, Applications of Graphene, Springer, New York, 2014, pp. 19–38.

[7] C. Backes, T.M. Higgins, A. Kelly, C. Boland, A. Harvey, D. Hanlon, J.N. Coleman, Guidelines for exfoliation, characterization and processing of layered materials produced by liquid exfoliation, Chem. Mater. 29 (2017) 243–255.

[8] J. Zhu, M.C. Hersam, Assembly and electronic applications of colloidal nanomaterials, Adv. Mater. 29 (2017) 1603895.

[9] S. Craciun, M. Russob, S. Yamamotoc, Taruchac, Tuneable electronic properties in graphene, Nano Today 6 (2011) 42–60.

[10] X. Li, G. Zhang, X. Bai, X. Sun, X. Wang, E. Wang, H. Dai, Highly conducting graphene sheets and Langmuir-Blodgett films, Nat. Nanotech. 3 (2008) 538–542.

[11] S.-K. Lee, H.Y. Jang, S. Jang, E. Choi, B.H. Hong, J. Lee, S. Park, J.-H. Ahn, All graphene-based thin film transistors on flexible plastic substrates, Nano Letters 12 (2012) 3472–3476.

[12] T. Tomašević-Ilić, J. Pešić, I. Milošević, J. Vujin, A. Matković, M. Spasenović, R. Gajić, Transparent and conductive films from liquid phase exfoliated graphene, Opt. Quant. Electron. 48 (2016) 319.

[13] M.R. Axet, R.R. Bacsa, B.F. Machado, P. Serp, Adsorption on and Reactivity of Carbon Nanotubes and Graphene, in: F. D'Souza, K.M. Kadish (Eds.), Handbook of Carbon Nano Materials, Volume 5: Graphene — Fundamental Properties, World Scientific, Singapore, 2014, pp. 39–183.

[14] I. Nasrallah, K.K. Banger, Y. Vaynzof, M.M. Payne, P. Too, J. Jongman, J.E. Anthony, H. Sirringhaus, Effect of ozone on the stability of solution-processed anthradithiophene-based organic field-effect transistors, Chem. Mater. 26 (2014) 3914–3919.

[15] P.J.D. Peterson, A. Aujla, K.H. Grant, A.G. Brundle, M.R. Thompson, J.V. Hey, R.J. Leigh, Practical use of metal oxide semiconductor gas sensors for measuring nitrogen dioxide and ozone in Urban environments, Sensors 17 (2017) 1653.

[16] Y. Xia, Y. Pan, H. Zhang, J. Qiu, Y. Zheng, Y.H. Chen, W. Huang, Graphene oxide by UV-Ozone treatment as efficient hole extraction layer for highly efficient and stable polymer solar cells, ACS Appl. Mater. Interfaces 9 (2017) 26252–26256.

[17] J.P. Froning, P. Lazar, M. Pykal, Q. Li, M. Dong, R. Zboril, M. Otyepka, Direct mapping of chemical oxidation of individual graphene sheets through dynamic force measurements at the nanoscale, Nanoscale 9 (2017) 119.

[18] E.X. Zhang, A.K.M. Newaz, B. Wang, C.X. Zhang, D.M. Fleetwood, K.I. Bolotin, R.D. Schrimpf, S.T. Pantelides, M.L. Alles, Ozone-exposure and annealing effects on graphene-on-SiO$_2$ transistors, Appl. Phys. Lett. 101 (2012) 121601.

[19] S. Zhao, P. Sumedh, S.P. Surwade, Z. Li, H. Liu, Photochemical oxidation of CVD-grown single layer graphene, Nanotechnology 23 (2012) 355703.

[20] N.M.R. Peres, Colloquium: The transport properties of graphene: An introduction, Rev. Mod. Phys. 82 (2010) 2673–2700.

[21] A. Matkovic, et al., Enhanced sheet conductivity of Langmuir-Blodgett assembled graphene thin films by chemical doping, 2D Mater. 3 (2016) 015002.

[22] A. Bosca, J. Pedros, J. Martínez, T. Palacios, F. Calle, Automatic graphene transfer system for improved material quality and efficiency, Sci. Reports 6 (2016) 21676.

[23] D. Todorović, A. Matković, M. Milićević, D. Jovanović, R. Gajić, I. Salom, M. Spasenović, Multilayer graphene condenser microphone, 2D Mater. 2 (2015) 045013.

[24] D. Porezag, T. Frauenheim, T. Kohler, G. Seifert, R. Kaschner, Construction of tight-binding-like potentials on the basis of density-functional theory: application to carbon, Phys. Rev. B 51 (1995) 12947.

[25] G. Seifert, D. Porezag, T. Frauenheim, Calculations of molecules, clusters, and solids with a simplified LCAO-DFT-LDA scheme, Int. J. Quantum Chem. 58 (1996) 185.

[26] B. Aradi, B. Hourahine, T. Frauenheim, DFTB+, a sparse matrix-based implementation of the DFTB method, J. Phys. Chem. 111 (2007) 5678.

[27] A. Zobelli, V. Ivanovskaya, P. Wagner, I.S. -Martinez, A. Yaya, C.P. Ewels, A comparative study of density functional and density functional tight binding calculations of defects in graphene, Phys. Stat. Sol. 249 (2012) 276.

[28] I. Popov, I. Đurišić, M. Belić, Designing topological defects in 2D materials using scanning probe microscopy and a self-healing mechanism: a density functional-based molecular dynamics study, Nanotechnology 28 (2017) 495706.

[29] E. Erdogan, I. Popov, C.G. Rocha, G. Cuniberti, S. Roche, G. Seifert, Engineering carbon chains from mechanically stretched graphene-based materials: Phys, Rev. B 83 (2011) 041401.

[30] E. Erdogan, I. Popov, G. Seifert, Robust electronic and transport properties of graphene break nanojunctions, Phys. Rev. B 83 (2011) 245417.

[31] S. Datta, Electronic Transport in Mesoscopic Systems, Cambridge University Press, Cambridge, 1997.

[32] Y.-W. Son, M.L. Cohen, S.G. Louie, Energy Gaps in Graphene Nanoribbons, Phys. Rev. Lett. 97 (2006) 216803.

[33] Y.-J. Yu, Y. Zhao, S. Ryu, L.E. Brus, K.S. Kim, P. Kim, Tuning the graphene work function by electric field effect, Nano Letters 9 (2009) 3430–3434.

[34] T. Takahashi, H. Tokailin, T. Sagawa, Angle-resolved ultraviolet photoelectron spectroscopy of the unoccupied band structure of graphite, Phys. Rev. B 32 (1985) 8317.

[35] A. Kasry, M.A. Kuroda, G.J. Martyna, G.S. Tulevski, A.A. Bol, Chemical doping of large-area stacked graphene films for use as transparent conducting electrodes, ACS Nano 4 (2010) 3839–3844.

[36] S. De, J.N. Coleman, Are there fundamental limitations on the sheet resistance and transmittance of thin graphene films? ACS Nano 4 (2010) 2713–2720.

[37] M. Acik, G. Lee, C. Mattevi, A. Pirkle, R.M. Wallace, M. Chhowalla, K. Cho, Y. Chabal, The role of oxygen during thermal reduction of graphene oxide studied by infrared absorption spectroscopy, J. Phys. Chem. C 115 (2011) 19761–19781.

[38] A.C. Ferrari, D.M. Basko, Raman spectroscopy as a versatile tool for studying the properties of graphene, Nat. Nanotech. 8 (2013) 235–246.

[39] L.G. Concado, A. Jorio, E.H. Martins Ferreira, F. Stavale, C.A. Achete, R.B. Capaz, M.V.O. Moutinho, A. Lombardo, T.S. Kulmala, A.C. Ferrari, Quantifying defects in graphene via raman spectroscopy at different excitation energies, Nano Letters 11 (2011) 3190–3196.

[40] L.E.F. Foa Torres, Stephan Roche, J.-C. Charlier, Introduction to Graphene-Based Nanomaterials: From Electronic Structure to Quantum Transport, Cambridge University Press Cambridge, 2014.

[41] L. Li, S. Reich, J. Robertson, Defect energies of graphite: density-functional calculations, Phys. Rev. B 72 (2005) 184109.

[42] M.V. Bracamonte, et al., On the nature of defects in liquid-phase exfoliated graphene on the nature of defects in liquid-phase exfoliated graphene, J. Phys. Chem. C 118 (2014) 15455–15459.

[43] A. Eckmann, A. Felten, A. Mishchenko, L. Britnell, R. Krupke, K.S. Novoselov,

C. Casiraghi, Probing the nature of defects in graphene by raman spectroscopy, Nano Letters 12 (2012) 3925–3930.

[44] A. Eckmann, A. Felten, I. Verzhbitskiy, R. Davey, C. Casiraghi, Raman study on defective graphene: effect of the excitation energy, type, and amount of defects, Phys. Rev. B 88 (2013) 035426.

[45] O. Hod, V. Barone, J.E. Peralta, G.E. Scuseria, Enhanced half-metallicity in edge-oxidized zigzag graphene nanoribbons, Nano Letters 7 (2007) 2295.

[46] G. Lee, K. Cho, Electronic structures of zigzag graphene nanoribbons with edge hydrogenation and oxidation, Phys. Rev. B 79 (2009) 165440.

[47] F.C. Sodi, G. Csanyi, S. Piscanec, A.C. Ferrari, Edge-functionalized and substitutionally doped graphene nanoribbons: Electronic and spin properties, Phys. Rev. B 77 (2008) 165427.

[48] D.A. Areshkin, D. Gunlycke, C.T. White, Ballistic transport in graphene nanostrips in the presence of disorder: importance of edge effects, Nano Letters 7 (2007) 204.

[49] F.M. Royas, D. Jacob, J.F. Rossier, J.J. Palacios, Coherent transport in graphene nanoconstrictions, Phys. Rev. B 74 (2006) 195417.

[50] T.C. Li, S.-P. Lu, Quantum conductance of graphene nanoribbons with edge defects, Phys. Rev. B 77 (2008) 085408.

[51] G. Henkelman, H. Jonsson, A dimer method for finding saddle points on high dimensional potential surfaces using only first derivatives, J. Chem. Phys. 111 (1999) 7010.

[52] H. Jonsson, G. Mills, K.W. Jacobsen, Nudged elastic band method for finding minimum energy paths of transitions, in: B.J. Berne, G. Cicotti, D.F. Coker (Eds.), Classical and Quantum Dynamics in Condensed Phase Systems, World Scientific, Singapore, 1998, pp. 385–404.

[53] G. Henkelman, B.P. Uberuaga, H. Jonsson, A climbing-image NEB method for finding saddle points and minimum energy paths, J. Chem. Phys. 113 (2000) 9901.

[54] K. Xu, P.D. Ye, Theoretical study on the oxidation mechanism and dynamics of the zigzag graphene nanoribbon edge by oxygen and ozone, J. Phys. Chem. C 118 (2014) 10400–10407.

[55] Ž. Šljivančanin, A.S. Milošević, Z.S. Popović, F.R. Vukajlović, Binding of atomic oxygen on graphene from small epoxy clusters to a fully oxidized surface, Carbon 54 (2013) 482.

Supplementary information

Reducing sheet resistance of self-assembled transparent graphene films by defect patching and doping with UV/ozone treatment

Tijana Tomašević-Ilić[1*], Đorđe Jovanović[1], Igor Popov[1, 2], Rajveer Fandan[3], Jorge Pedrós[3], Marko Spasenović[1], Radoš Gajić[1]

[1]Graphene Laboratory (GLAB) of the Center for Solid State Physics and New Materials, Institute of Physics, University of Belgrade, Pregrevica 118, 11080 Belgrade, Serbia

[2]Institute for Multidisciplinary Research, University of Belgrade, Kneza Višeslava 1a, 11000 Belgrade, Serbia

[3]Departamento de Ingeniería Electrónica and Instituto de Sistemas Optoelectrónicos y Microtecnología, Universidad Politécnica de Madrid, Madrid 28040, Spain

*E-mail: ttijana@ipb.ac.rs

UV/Ozone treatment was performed on CVD single- and multilayer graphene. Corresponding Raman spectra are shown in Figure S1.
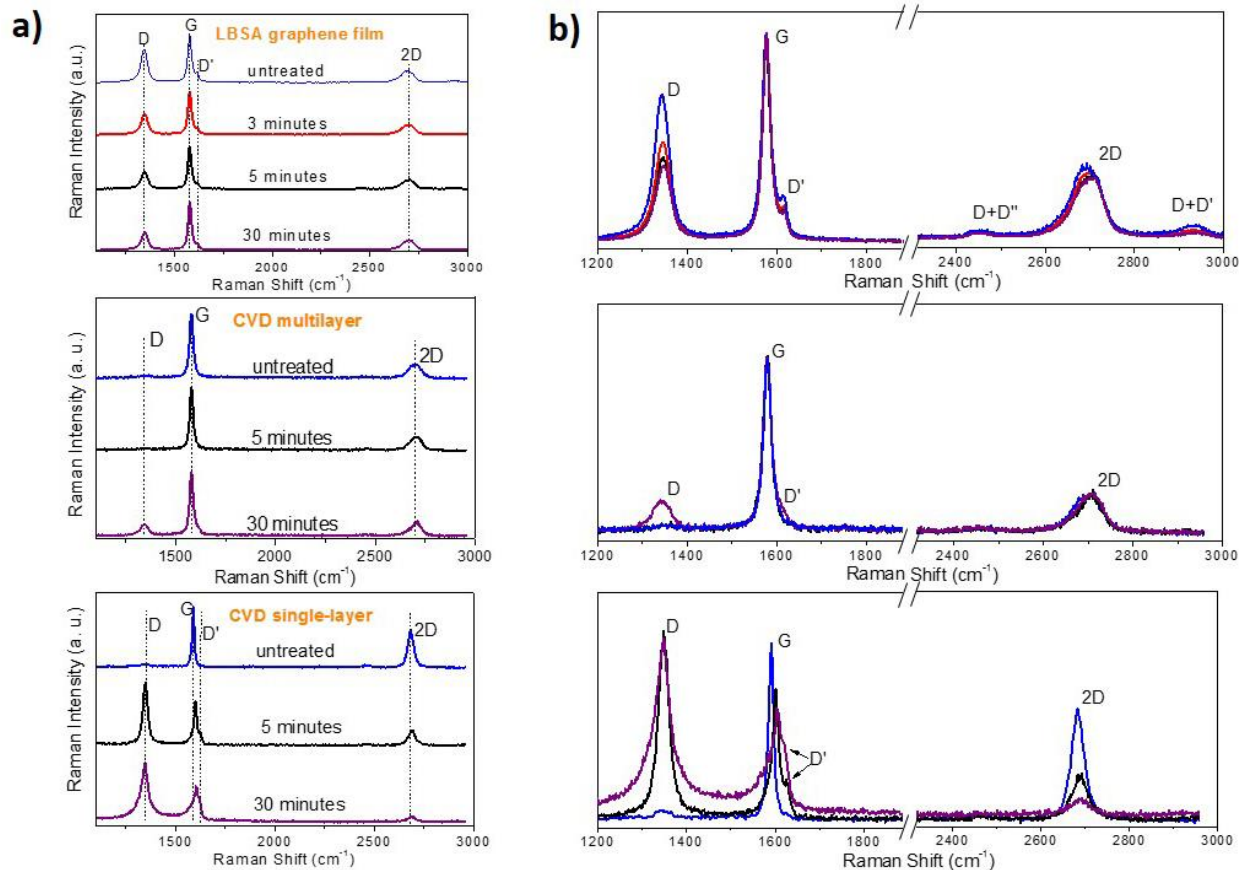
Fig. S1 (a) Raman spectra of the LBSA, CVD-grown multilayer and CVD-grown single-layer graphene films as a function of UVO exposure time, (b) Close-up view of the main bands of (a).

In all cases, Raman spectra show evident changes of the intensity of the D mode with photochemical oxidation. Figure S1 highlights the different behavior of LBSA and CVD graphene in an oxidizing environment. In contrast to the effect that UVO has on LBSA graphene, described in the main text, treatment of CVD graphene leads to defect generation. Upon photochemical oxidation, CVD graphene develops a strong D peak in the Raman spectra after only 5 min of exposure, indicating oxidative removal of the graphitic material and the formation

of a significant number of defects. Figure S2a shows a comparison of the ratio of the D-peak to the G-peak before and after UVO exposure for LBSA, CVD multilayer and CVD single-layer graphene. As highlighted in the main text, a large decrease of this ratio is observed after UVO exposure for LBSA graphene and an increase of this ratio is observed after the same time of exposure for CVD graphene, indicating defect patching in LBSA and defect formation in CVD. Figure S2b shows a change in the mean free path with UVO exposure of all three types of graphene.
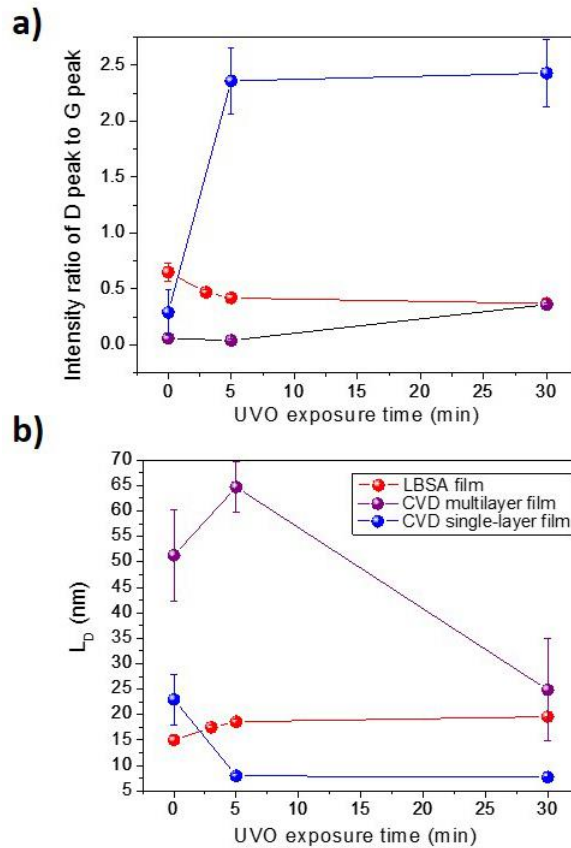
Fig. S2 (a) The D/G intensity ratio of the LBSA, CVD-grown multilayer and CVD-grown single-layer graphene films as a function of UVO exposure time. The D/G ratio is calculated from integrated peak areas. (b) Interdefect distance of the coresponding graphene films as a function of UVO exposure time. The error bar represents the standard deviation of five measurements.
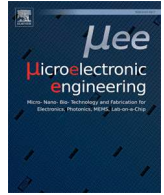
Research paper

Miniature graphene-based supercapacitors fabricated by laser ablation

CrossMark

Snezana M. Djuric [a],[*], Goran Kitic [a], Georges Dubourg [a], Rados Gajic [b], Tijana Tomasevic-Ilic [b], Vladan Minic [a], Marko Spasenovic [b]

[a] University of Novi Sad, BioSense Institute, Dr Zorana Djindjica 1, 21000 Novi Sad, Serbia
[b] Graphene Laboratory (GLAB) of the Center for Solid State Physics and New Materials, Institute of Physics, University of Belgrade, Pregrevica 118, 11080 Belgrade, Serbia

ABSTRACT

Micro-supercapacitors are high-performance energy storage devices, which are particularly important for building a micropower system to power portable and wearable devices. This study demonstrates a fabrication route for graphene-based in-plane micro-supercapacitors using a laser system for micromachining of electrodes on LTCC substrate. Micro-electrodes were patterned by programmed laser scanning. The proposed subtractive fabrication route is green, on demand and it enables the direct printing of micro-scale features (about 50 μm) with a precision of 2 μm. The width of electrodes was 210 μm, spacing between electrodes was 60 μm, and the length was 6.8 mm. In order to build all solid-state supercapacitive devices, a gel electrolyte was introduced into the active area of micro-electrodes (0.68 cm^2). Laser patterning enables fabrication of micro-supercapacitors of arbitrary sizes and patterns, thus providing a good opportunity for miniaturized electronic applications. Electrochemical characterization was performed. The resulting micro-supercapacitors deliver an area capacitance of 80.5 μF/cm^2.

© 2017 Elsevier B.V. All rights reserved.

1. Introduction

Recent advances in development of miniaturized electronic devices (portable electronics, wearable electronics) has increased the demand for energy systems with optimized capacity, cycle life, power and environmental impact. Energy storage devices have been identified as important electronic components for environmental and sustainable protection and efficient energy development and storage. Sustainable energy research has led to development of novel energy storage systems, particularly for the utilization of renewable energy. Renewable energy systems irregularly generate electricity. A promising solution to address this challenge is the development of efficient electrochemical energy storage systems like batteries and supercapacitors (SCs). One of the most important advantages of batteries over SCs is that for a given volume, they can store 3 to 30 times more energy. However, SCs can deliver the power that is hundreds to many thousands times larger than the power of similar-sized batteries. The life cycle of batteries is generally limited to several hundred to a few thousand cycles, compared to the many millions of life cycles for SCs [1].

Supercapacitors as high-performance energy storage devices are particularly important for building a micropower system, which will power up portable and wearable devices for a long time without maintenance. Their main advantages are portability, low environmental impact, flexibility, stability, safety, light-weight, high power density, and long cycle life.

According to the charge storage mechanism, SCs are generally divided into electric double layer capacitors (EDLCs) and pseudocapacitors. In EDLC, electrostatic energy storage is accumulated at the electrode/electrolyte interface (a Helmholtz double layer). The high capacitance is strongly dependent from high specific surface area and electronically conducting electrodes. In contrast, pseudocapacitors use fast and reversible electron transfer of the redox-active materials based on transitional metal oxides as well as electronically conducting polymers for charge storage [2,3]. All carbon-based materials with a high-surface area (activated carbon, carbon nanotubes, graphene, etc.) are used as electrode materials for EDLCs, whereas transition metal oxides (RuO_2, MnO_2, CoO_x, NiO, Fe_2O_3, etc.) and conducting polymers (polypyrrole, polyaniline, etc.) are used as electrode materials for pseudocapacitors [4].

EDLC SCs can be manufactured using different printing and lithography techniques. The binder-free microelectrodes were developed by combining electrostatic spray deposition and photolithography lift-off methods [5]. Fabrication procedure of three-dimensional micro supercapacitors with thick interdigitated electrodes supported and separated by SU-8 and sealed by PDMS caps with ionic liquid electrolytes injected into the electrode area was presented in [6]. A novel class of all solid-state graphene-based in-plane interdigitated micro-

supercapacitors on both rigid and flexible substrates through micropatterning of graphene films was demonstrated in [7]. Combined photolithography with selective electrophoretic buildup were used to fabricate lateral ultrathin reduced graphene oxides microelectrodes for all-solid-state micro-supercapacitors with a gel electrolyte [8]. A new approach for fabricating solid-state flexible micro SCs through selective wetting-induced micro-electrode patterning was analyzed in [9]. A tailorable gel-based supercapacitor with symmetric electrodes prepared by combining electrochemically reduced graphene oxide deposited on a nickel nanocone arrays current collector was presented in [10]. Scalable fabrication of flexible and high-performance graphene-based monolithic micro SCs by photochemical reduction and patterning of graphene oxide/TiO_2 hybrid films was described in [11].

A versatile printable technology to fabricate arbitrary-shaped, printable graphene-based planar sandwich SCs based on the layer-structured film of electrochemically exfoliated graphene as two electrodes and nanosized graphene oxide as a separator on one substrate was demonstrated in [12].

An ink-jet printed micro SCs (ink-jet printed graphene was on top of ink-jet printed silver current collectors) was reported in [13]. A new class of solid-state power sources fabricated on paper substrate by inkjet printer was demonstrated in [14]. A 3D printing technique known as direct-ink writing was applied for the fabrication of 3D periodic graphene composite aerogel microlattices for supercapacitor application. The 3D printing method was modified as to accommodate processing of an extrudable graphene oxide-based composite ink [15].

However, new techniques, which reduce the cost and improve scalability and form factor are constantly in demand. One such technique is laser-processed fabrication of supercapacitors. The scalable fabrication of a new type of all carbon, monolithic supercapacitors by laser reduction and patterning of graphite oxide films (avoiding the restacking of graphene sheets) was demonstrated in [16]. A graphene-oxide (GO) film supported on a flexible substrate was placed on top of a LightScribe-enabled DVD media disc, and a computed image is then laser-irradiated on the GO film in a computerized LightScribe DVD film in [17,18]. A new approach for fabrication of 2D MoS_2 film based micro-supercapacitors via laser patterning of painted MoS_2 films was presented in [19]. The fabrication of SCs based on laser carbonization of polyimide sheets, where localized pulsed laser irradiation rapidly converts the pristine polyimide surface into an electrically conductive porous structure was presented in [20–22]. Laser machining was applied to carbon films for the fabrication of microelectrodes on a glass wafer in [23]. A controlled high powered CO_2 laser system was used to reduce and pattern a graphene oxide film supported onto a flexible polyethylene terephthalate substrate [24,25]. Graphene-based in-plane flexible interdigitated micro-supercapacitor devices fabricated through direct laser writing onto ultra-thin graphite oxide films were presented in [26]. Although the focus of this work was on EDLC SCs, laser processed techniques can be applied for fabrication of hybrid supercapacitors as well. Energy-dense and high-power supercapacitor electrodes were realized by integrating a highly conductive and high-surface-area 3D laser-scribed graphene framework with MnO_2 [27].

There are different technologies used for macroscale patterning to achieve interdigital electrodes. High-temperature carbonization is one way to produce electrically conductive carbon for supercapacitors [28, 29]. The high-temperature carbonization is limited to rigid substrates that can survive high-temperatures, which is a shortcoming. Transfer of a porous carbon (electrodes), as a product of high-temperature carbonization, to flexible substrates requires a tedious step [30,31]. Microinterdigital electrodes can be patterned in a controlled way using photolithography, followed by high-temperature carbonization [32] or combining electrostatic spay deposition and photolithography lift-off [5]. However, microinterdigital electrodes can be directly written on flexible substrate by the laser-induced carbonization where the flexible substrate (pristine polymer) is used as precursor for carbonization [20]. Thin and flexible graphene interdigital electrodes were achieved

via direct writing on graphite oxide dispersed over the flexible substrate using lasers to reduce graphite oxides [17,18,24,25]. Ink-jet printing, which enables additive patterning, direct writing, low cost and scalability, can be used to print graphene or reduced graphene oxide for interdigital electrodes of supercapacitors [33,34,13]. Ink-jet printing is limited by the difficulties in delivering sufficient porous material and maintaining resolution. Thus, the method, which allows for freedom in the choice and amount of material that can be delivered is direct printing of graphite oxide into a specific pattern with a liquid dispenser, which was originally designed as a DNA array, and subsequent reduction of the graphite oxide [35]. The use of gravure for the printing of reduced graphene interdigital microsupercapacitors is attractive due to its high throughput, optimal control of feature size, and ability to use very wide range of potential inks [36,37]. A novel mask-free plasma-scanning method is used to fabricate all-solid-state interdigital microsupercapacitors via the application of an atmospheric pulsed micro-plasma jet [38,39]. The method does not require photoresist, masks, post-processing, vacuum system, high temperature treatment or clean room operations. Interdigital electrodes configuration are wildly used for design of EDLC. However, besides planar interdigital configuration, a three dimensional (3D) interdigital structure is used for microsupercapacitors [40]. 3D configuration significantly increases surface area for the same footprint. A theoretical study showed that a double stacked 3D configuration increases charging capacity for the same footprint in comparison with one layer 3D configuration [41]. An innovative approach to fabricate highly conductive interdigital microelectrodes is femtolaser in-situ reduction of hydrated graphene oxide and chloroauric acid ($HAuCl_4$) nanocomposite simultaneously, which incorporates both the patterning of reduced graphene oxide and the fabrication of Au collectors in a single step [42].

In the present study, a fabrication route of miniature graphene-based supercapacitors with laser processed electrodes is introduced. The study will explore electrochemical properties of graphene-based supercapacitors for energy storage applications. Screen printed gold layers on LTCC substrates have been used as current collectors. Thin films from liquid phase exfoliated graphene have been used as active material. These all-solid-state micro-supercapacitors have been fabricated using hydrogel (comprising aqueous H_2SO_4 solution and poly(vinyl alcohol)).

2. Fabrication procedure

2.1. Fabrication of LTCC substrate

The Low Temperature Cofired Ceramic (LTCC) technology is a way to produce multilayer circuits with the help of single tapes, which are to be used to apply conductive, dielectric and/or resistive pastes on. In this work, LTCC technology was used to prepare substrates with gold layers on the top for fabrication of miniature supercapacitors. Fig. 1 illustrates the fabrication process of the LTCC substrate. First, a mask design for via punching and tape cutting and a mask design for screen printing were prepared. Ceramtec: Ceramtape GC tapes were used. Tape cutting and via punching was performed using Diode pumped Laser Rofin Powerline D, ND: YAG, 1064 nm and computer loaded image files containing necessary mask designs. For screen fabrication, a photopolymer film of 30 μm was used and a screen of mesh size 325, wire diameter 0.03 mm and mesh width 0.05 mm was used. The screen was thoroughly cleaned, carefully coated, exposed and eventually a mask for a gold layer was developed. Gold layers were printed using Ekra M2H screen printer and TC 7102 gold conductive paste. Lamination mold and prepared tapes were dried in an oven at 80 °C before a collating step (in order to achieve a similar temperature with a lamination press CARVER 395CEB). The tapes were pressed between heated platens at 75 °C, 2300 kg for 3 min. Laminates were fired in the oven Nabertherm L9 11 SKM. Firing is performed according to two-step profile at two dwell temperatures: organic burnout and sintering temperature.
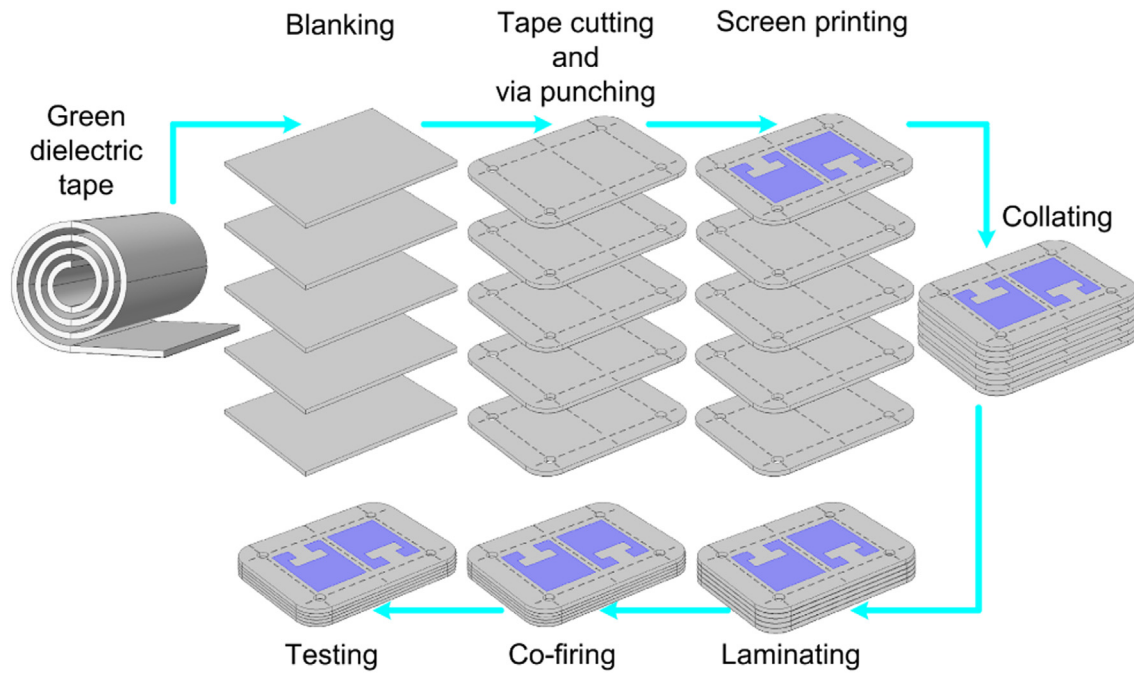
Fig. 1. LTCC processing steps to fabricate substrate with gold layers for supercapacitor's electrodes.

Organic burnout was done at 450 °C, which was reached with 2 °C/min rate, while sintering was done at 865 °C reached with the rate of 4 °C/min. After the end of firing cycle, a natural cooling took place. Gold layers were used as current collectors for electrochemical cells.

2.2. Preparation of graphene dispersion

Graphene sheets were exfoliated from graphite by ultrasonic treatment in a water solution of surfactant, sodium dodecylbenzenesulfonate (SDBS). All chemicals were purchased from Sigma Aldrich: graphite powder (product number 332461) and sodium dodecylbenzenesulfonate (product number 289957). Stock solution of SDBS was prepared in deionized water (resistivity 18 MΩ) by stirring overnight. The sample was prepared by dispersing graphite powder (concentration of 36 mg ml^{-1}) in the water solution of surfactant using 10 h of sonication in a low power sonic bath (Bransonic CPXH Ultrasonic Cleaning Bath). The resulting dispersion was centrifuged for 60 min at 3000 rpm in

order to reduce the amount of unexfoliated graphite. More details about graphene dispersion preparation is given in [43].

2.3. Spin-coating and laser ablation

Fabricated LTCC substrate with gold layers is shown in Fig. 2a. A multilayer graphene film was deposited over a gold layer (current collector) on LTCC substrate as the active material for supercapacitor electrodes, as it is shown in Fig. 2b. Each layer of the graphene film was obtained by spin-coating the graphene dispersion for 20 s at 1000 rpm. Three prototypes of supercapacitors, with different number of layers in graphene film, were fabricated and tested. In Sample 1, the active material was 20-layer graphene film. In Sample 2, the active material was 30-layer graphene film. In Sample 3, the active material was 40-layer graphene film. After deposition of each layer of graphene film, the substrate was heated in an oven for 10 s at 100 °C. After deposition of the last layer of graphene film, the substrate was heated in the oven for 12 min at 100 °C.
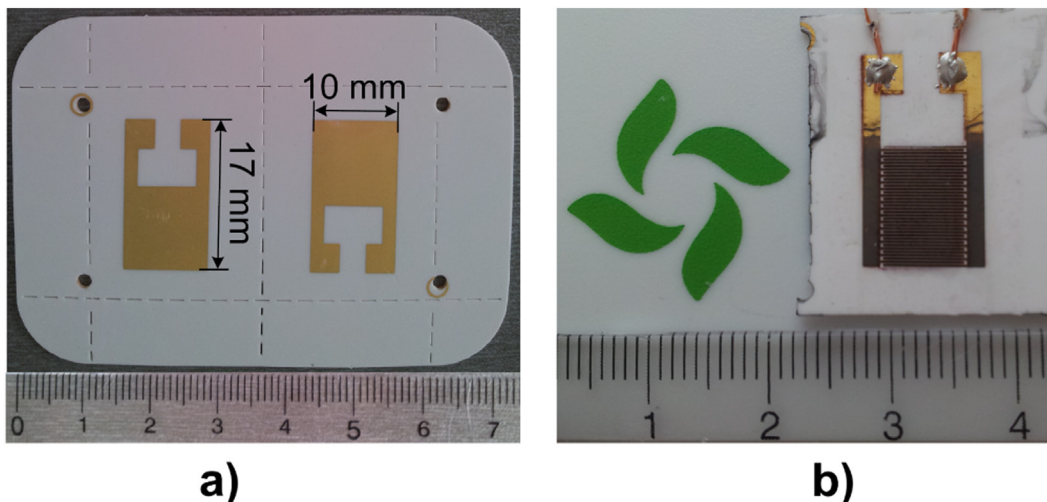
Fig. 2. a) LTCC substrate with gold layers for electrodes fabrication and b) interdigitated electrodes were laser ablated after deposition of graphene dispersion over gold layer.

A laser ablation process (Diode pumped Laser Rofin Powerline D, ND: YAG, 1064 nm) was used for shaping the geometries necessary for the interdigitated electrodes. A fabricated prototype of a supercapacitor with interdigitated electrodes on LTCC substrate is shown in Fig. 2b. The substrate constituted of a gold layer and graphene film was carefully aligned using a camera with computer-loaded image files containing interdigitated electrode designs. The current applied to the laser was adjusted to 28.7 A, in order to generate ablation of the layers without damaging the electrodes by a thermal effect. A frequency of 50 kHz and a speed of 150 mm/s were selected to achieve fast and well-resolved ablation. Four passes were needed to completely ablate the gold layer covered with the active material. The width of electrodes was 210 μm, spacing between electrodes was 60 μm, and the length was 6.8 mm. Laser ablation techniques enable direct printing of micro-scale objects from computer loaded image files in a cost effective, time saving and environmentally friendly fabrication process. The proposed subtractive fabrication method is green, on demand (less than 1 min is needed to ablate the interdigitated electrodes) and it enables the direct printing of micro-scale features (about 50 μm) with a precision of 2 μm.

2.4. Preparation of the hydrogel-polymer electrolyte, PVA-H₂SO₄

Polyvinyl alcohol (PVA) (Polyvinyl Alcohol 72,000 BioChemica, A2255, AppliChem) powder was mixed with deionized water (1 g PVA/10 g H_2O). The mixture was heated at approximately 90 °C under constant stirring until the solution turned clear. After cooling under ambient conditions, 0.8 g of concentrated sulfuric acid solution (95%–97% solution in water, 1093/5, ZORKA Pharma Hemija) was added and the solution was stirred thoroughly [18]. A 3D profile of the part of supercapacitor's electrodes, without electrolyte, is presented in Fig. 3a. The solid-state SCs were finished by drop-casting a PVA/H₂SO₄ solution as a solid electrolyte on micro-patterned electrodes. The active surface area, including the area of microelectrodes and the interspaces between them, was approximately 0.68 cm^2. A 2D view of electrodes surface with hydrogel-polymer electrolyte is shown in Fig. 3b. After deposition of the electrolyte, the sample was left in a fume hood for 24 h, to allow the electrolyte to solidify. Fig. 3 clearly shows that the microelectrodes are well aligned without any conspicuous defects or cuts. Before all experiments, using a multimeter, it was confirmed there was no electrical contact between the electrodes.

3. Capacitance studies

3.1. Electrochemical characterization

Cyclic voltammograms (CV) for the micro-supercapacitor cells are presented in Fig. 4. Cyclic voltammetry was examined at the scan rates from 10 mV/s to 3000 mV/s. All electrochemical measurements were carried out at room temperature. As shown in Fig. 4, the CV responses exhibit the typical capacitive behavior of a supercapacitor due to symmetrical electrode configuration and the potential-dependent charging behavior. CV loops are not of ideal rectangular shape due to the existence of cell resistance, and it is a common phenomenon in the capacitors. The resistance is determined by two factors. The first one is small ionic conductivity of the electrolyte and the second one is polymer electrolyte wetting within the electrodes. Although polymer electrolyte diffuses less inside the micro-electrodes than aqueous electrolyte, still diffusion process occurs. During the diffusion of H_2SO_4/PVA electrolyte, the gel electrolyte becomes solid due to the evaporation of water and, finally diffusion of the gel electrolyte stops. The open edges of micro-patterned electrodes with active material enhance the ability of the gel electrolyte to infiltrate into the layers of the electrodes, thus further enhancing total accessible electrochemical surface. In addition, non-ideal rectangular shape can be ascribed to the reaction of electrochemically active surface groups formed during laser processing. The cyclic voltammogram profiles contain some noise, which indicates that their energy state becomes non-uniformly distributed, thus provoking locally irregular doping energy states [44]. However, the CV loops are generally rectangular in shape over a wide range of scan rates confirming the formation of an electrical double layer and good charge propagation across the electrodes. Pseudocapacitive peaks are not apparent within the examined potential window. Electrochemical performance of Samples 1 and 2 was examined for the potential window of 0.8 V, whereas the potential window for Sample 3 was increased to 1 V, as it is shown in Fig. 4. Increasing the scan rate, the peak current density continues to increase fast, characteristic of a good instantaneous power. Sample 3 has the highest peak current density of all samples, as it is shown in Fig. 3c. The comparison of CV profiles for all three samples at a constant scan rate of 10 mV/s is shown in Fig. 3d. Although, all three CV profiles have similar shape, Sample 3 has a significantly higher peak current density. Electrochemical impedance spectroscopy also indicates supercapacitive effect, as it is shown in Fig. 5. A semi-vertical line is seen at low-frequencies which is common for supercapacitors. A leveling-off of the curve is observed at high frequencies as the consequence of large dynamic change in the electric field, which affect ion transport through the electrode pores [20], as it is shown in a magnified view in Fig. 5.

3.2. Capacitance calculation

The capacitance values were calculated from the CV data according to the Eq. (1):

$$C_{device} = \frac{1}{v(V_f - V_i)} \int_{V_i}^{V_f} I(V)dV, \tag{1}$$
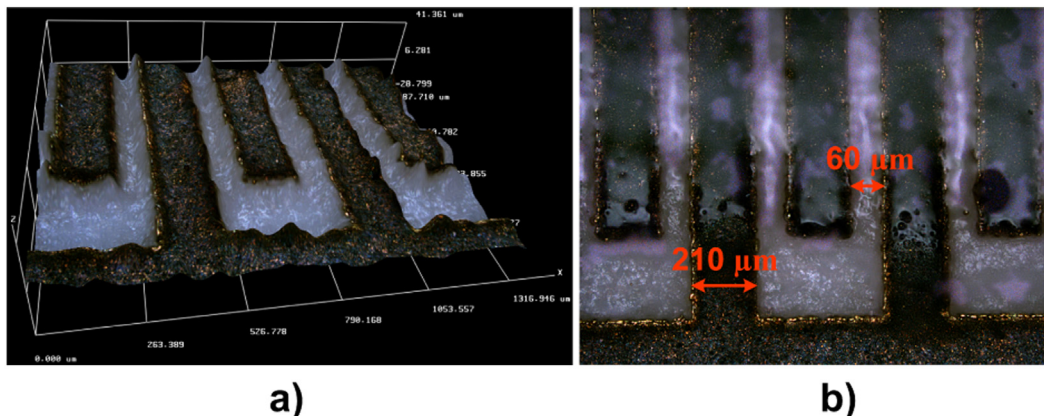
Fig. 3. a) A 3D image of the part of interdigitated electrodes before electrolyte deposition and b) a 2D image of the part of interdigitated electrodes after electrolyte deposition. Images were obtained by Huvitz HRM 300 profilometer.
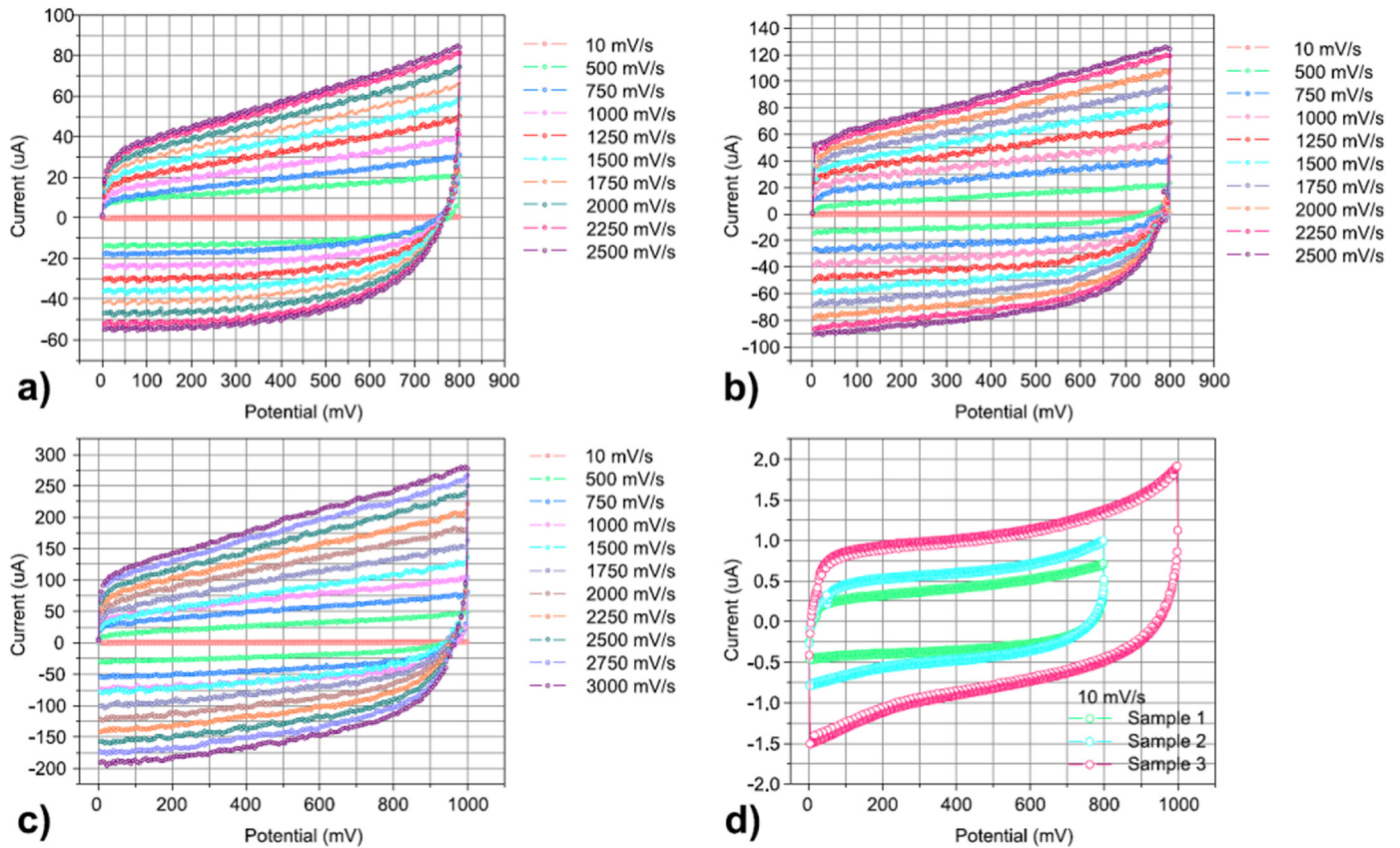
Fig. 4. Electrochemical properties of micro-supercapacitors a) Sample 1, b) Sample 2, c) Sample 3 and d) Comparison of cyclic voltammograms for Sample 1, Sample 2 and Sample 3 at 10 mV/s.

where C_{device} is the capacitance contribution from graphene electrodes, v is the scan rate (mV/s), V_i and V_f are the integration potential limits of the voltammetric curve and $I(V)$ is the voltammetric discharge current.

Specific capacitances were calculated based on the area of the device according to the Eq. (2):

$$C_{area} = C_{device}/V, \tag{2}$$

where C_{area} (in Fcm^{-2}) refer to the area capacitance of device. A and V are the total area of the device. The area capacitances were calculated based on the entire active surface area of the supercapacitor, including the area of microelectrodes and the interspaces between them (0.68 cm^2).

The capacitive contribution obtained from the integrated area under the CV loops revealed that the supercapacitive value of microelectrode is typically increased with the decrease in the scan rate, as it is shown in Fig. 6. The area capacitance for Sample 1 is 31.1 μF/cm^2, for Sample 2 is 47.4 μF/cm^2 and for Sample 3 80.5 μF/cm^2, comparable to the values reported in the literature for graphene based microsupercapacitors [7].

4. Conclusion

In summary, graphene based all solid-state micro-supercapacitors were fabricated using the focused laser beam to induce ablation of micro-supercapacitors on LTCC substrate. Electrochemical characterization of micro-supercapacitors showed formation of an electrical double layer and good charge propagation across the electrodes. The highest delivered area capacitance is 80.5 μF/cm^2, which is comparable with previously published works. The advantage of the applied fabrication route is laser patterning of micro-electrodes which requires short processing time and introduces flexibility and scalability in design of device geometry.

Acknowledgments
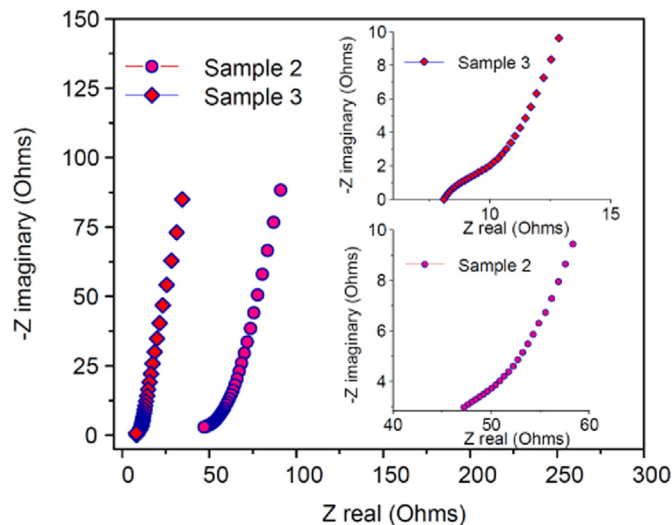
Fig. 5. Measured electrochemical impedance plots for Samples 2 and 3, with a magnified view of high frequency response.
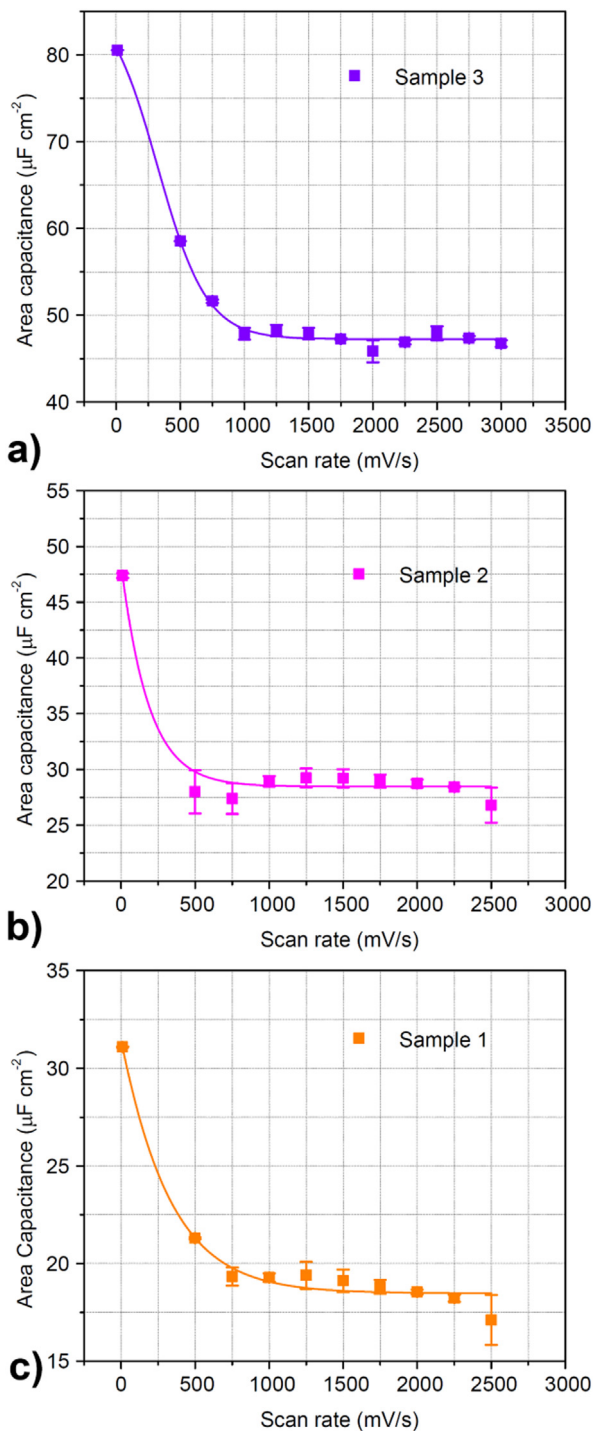
Fig. 6. Evolution of the area capacitance versus scan rate for a) Sample 3, b) Sample 2, and c) Sample 1.

References

[1] J.R. Miller, P. Simon, Electrochemical capacitors for energy management, Science 321 (2008) 651–652.
[2] P. Yang, W. Mai, Flexible solid-state electrochemical supercapacitors, Nano Energy 8 (2014) 274–290.
[3] Y. Zheng, Y. Yang, S. Chen, Q. Yuan, Smart, stretchable and wearable supercapacitors: prospects and challenges, CrystEngComm 18 (2016) 4218–4235.
[4] T. Palaniselvam, J.-B. Baek, Graphene based 2D-materials for supercapacitors, 2D Mater. 2 (2015) 032002.
[5] M. Beidaghi, C. Wang, Micro-supercapacitors based on interdigital electrodes of reduced graphene oxide and carbon nanotube composites with ultrahigh power handling performance, Adv. Funct. Mater. 22 (21) (2012) 4501–4510.
[6] S. Li, X. Wang, H. Xing, C. Shen, Micro supercapacitors based on a 3D structure with symmetric graphene or activated carbon electrodes, J. Micromech. Microeng. 23 (11) (2013) (Article# 114013, 10pp).
[7] Z.-S. Wu, K. Parvez, X. Feng, K. Müllen, Graphene-based in-plane micro-supercapacitors with high power and energy densities, Nat. Commun. 4 (2013) (Article#2487).
[8] Z. Niu, L. Zhang, L. Liu, B. Zhu, H. Dong, X. Chen, All-solid-state flexible ultrathin micro-supercapacitors based on graphene, Adv. Mater. 25 (29) (2013) 4035–4042.
[9] S.-K. Kim, H.-J. Koo, A. Lee, P.V. Braun, Selective wetting-induced micro-electrode patterning for flexible micro-supercapacitors, Adv. Mater. 26 (30) (2014) 5108–5112.
[10] B. Xie, C. Yang, Z. Zhang, P. Zou, Z. Lin, G. Shi, Q. Yang, F. Kang, C.-P. Wong, Shape-tailorable graphene-based ultrahigh rate supercapacitor for wearable electronics, ACS Nano 9 (6) (2015) 5636–5645.
[11] S. Wang, Z.-S. Wu, S. Zheng, F. Zhou, C. Sun, H.-M. Cheng, X. Bao, Scalable fabrication of photochemically reduced graphene-based monolithic micro-supercapacitors with superior energy and power densities, ACS Nano (2017)http://dx.doi.org/10.1021/acsnano.7b01390.
[12] S. Zheng, X. Tang, Z.-S. Wu, Y.-Z. Tan, S. Wang, C. Sun, H.-M. Cheng, X. Bao, Arbitrary-shaped graphene-based planar sandwich supercapacitors on one substrate with enhanced flexibility and integration, ACS Nano 11 (2) (2017) 2171–2179.
[13] J. Li, F. Ye, S. Vaziri, M. Muhammed, M.C. Lemme, M. Östling, Efficient inkjet printing of graphene, Adv. Mater. 25 (2013) 3985–3992.
[14] K.-H. Choi, J. Yoo, C.K. Lee, S.-Y. Lee, All-inkjet-printed, solid-state flexible supercapacitors on paper, Energy Environ. Sci. 9 (2016) 2812–2821.
[15] C. Zhu, T. Liu, F. Qian, T.Y.-J. Han, E.B. Duoss, J.D. Kuntz, C.M. Spadaccini, M.A. Worsley, Y. Li, Supercapacitors based on three-dimensional hierarchical graphene aerogels with periodic macropores, Nano Lett. 16 (2016) 3448–3456.
[16] W. Gao, N. Singh, L. Song, Z. Liu, A.L.M. Reddy, L. Ci, R. Vajtai, Q. Zhang, B. Wei, P.M. Ajayan, Direct laser writing of micro-supercapacitors on hydrated graphite oxide films, Nat. Nanotechnol. 6 (2011) 496–500.
[17] M.F. El-Kady, V. Strong, S. Dubin, R.B. Kaner, Laser scribing of high-performance and flexible graphene-based electrochemical capacitors, Science 35 (2012) 1326–1330.
[18] M.F. El-Kady, R.B. Kaner, Scalable fabrication of high-power graphene micro-supercapacitors for flexible and on-chip energy storage, Nat. Commun. 4 (2013) (Article#1475).
[19] L. Cao, S. Yang, W. Gao, Z. Liu, Y. Gong, L. Ma, G. Shi, S. Lei, Y. Zhang, S. Zhang, R. Vajtai, P.M. Ajayan, Direct laser-patterned micro-supercapacitors from paintable MoS$_2$ films, Small 9 (17) (2013) 2905–2910.
[20] J.B. In, B. Hsia, J.-H. Yoo, S. Hyun, C. Carraro, R. Maboudian, C.P. Grigoropoulos, Facile fabrication of flexible all solid-state micro-supercapacitor by direct laser writing of porous carbon in polyimide, Carbon 83 (2015) 144–151.
[21] J. Lin, Z. Peng, Y. Liu, F. Ruiz-Zepeda, R. Ye, E.L.G. Samuel, M.J. Yacaman, B.I. Yakobson, J.M. Tour, Laser-induced porous graphene films from commercial polymers, Nat. Commun. 5 (2014) (Article#5714).
[22] Z. Peng, J. Lin, R. Ye, E.L.G. Samuel, J.M. Tour, Flexible and stackable laser induced graphene supercapacitors, ACS Appl. Mater. Interfaces 7 (5) (2015) 3414–3419.
[23] H.-C. Huang, C.-J. Chung, C.-T. Hsieh, P.-L. Kuo, H. Teng, Laser fabrication of all-solid-state microsupercapacitors with ultrahigh energy and power based on hierarchical pore carbon, Nano Energy 21 (2016) 90–105.
[24] E. Ghoniem, S. Mori, A. Abdel-Moniem, Low-cost flexible supercapacitors based on laser reduced graphene oxide supported on polyethylene terephthalate substrate, J. Power Sources 324 (2016) 272–281.
[25] B. Xie, Y. Wang, W. Lai, W. Lin, Z. Lin, Z. Zhang, P. Zou, Y. Xu, S. Zhou, C. Yang, F. Kang, C.-P. Wong, Laser-processed graphene based micro-supercapacitors for ultrathin, rollable, compact and designable energy storage components, Nano Energy 26 (2016) 276–285.
[26] R. Kumar, R. Savu, E. Joanni, A.R. Vaz, M.A. Canesqui, R.K. Singh, R.A. Timm, L.T. Kubota, S.A. Moshkalev, Fabrication of interdigitated micro-supercapacitor devices by direct laser writing onto ultra-thin, flexible free-standing graphite oxide films, RSC Adv. 6 (2016) 84769–84776.
[27] M.F. El-Kady, M. Ihns, M. Li, J.Y. Hwang, M.F. Mousavi, L. Chaney, A.T. Lech, R.B. Kaner, Engineering three-dimensional hybrid supercapacitors and microsupercapacitors for high-performance integrated energy storage, PNAS 112 (14) (2015) 4233–4238.
[28] Z. Laušević, P.Y. Apel, J.B. Krstić, I.V. Blonskaya, Porous carbon thin films for electrochemical capacitors, Carbon 64 (2013) 456–463.
[29] H. Wang, Z.W. Xu, A. Kohandehghan, Z. Li, K. Cui, X.H. Tan, et al., Interconnected carbon nanosheets derived from hemp for ultrafast supercapacitors with high energy, ACS Nano 7 (6) (2013) 5131–5141.
[30] M.S. Kim, B. Hsia, C. Carraro, R. Maboudian, Flexible Microsupercapacitors From Photoresist-derived Carbon Electrodes on Flexible Substrates, Proceedings of IEEE MEMS Conference, San Francisco, CA, 2014.
[31] S. Chen, X. Wang, J. Pu, S. Li, A Surface-mount Flexible Micro-supercapacitors on Ultra Thin Parylene-C Substrate, Proceedings of 18th International Conference on Transducers, Anchorage, AK, 2015.
[32] B. Hsia, M.S. Kim, M. Vincent, C. Carraro, R. Maboudian, Photoresist-derived porous carbon for on-chip microsupercapacitors, Carbon 57 (2013) 395–400.
[33] L.T. Le, M.H. Ervin, H. Qiu, B.E. Fuchs, J. Zunino, W.Y. Lee, Ink-jet printed graphene for flexible micro-supercapacitors, 11th IEEE Conference on Nanotechnology 2011, pp. 67–71.

[34] L.T. Le, M.H. Ervin, H. Qiu, B.E. Fuchs, W.Y. Lee, Graphene supercapacitor electrodes fabricated by inkjet printing and thermal reduction of graphene oxide, Electrochem. Commun. 13 (4) (2011) 355–358.

[35] H. Jung, C.V. Cheah, N. Jeong, J. Lee, Direct printing and reduction of graphite oxide for flexible supercapacitors, Appl. Phys. Lett. 105 (2014) (Article#053902).

[36] Y. Xiao, L. Huang, Q. Zhang, S. Xu, Q. Chen, W. Shi, Gravure printing of hybrid MoS$_2$ @ S-rGO interdigitated electrodes for flexible supercapacitors, Appl. Phys. Lett. 107 (2015) (Article#113906).

[37] Q. Zhang, L. Huang, Q. Chang, W. Shi, L. Shen, Q. Chen, Gravure-printed interdigital microsupercapacitors on a flexible polyimide substrate using crumpled graphene ink, Nanotechnology 27 (2016) (Article#105401).

[38] D. Ye, S.-Q. Wu, Y. Yu, L. Liu, X.-P. Lu, Y. Wu, Patterned graphene functionalization via mask free scanning of micro-plasma jet under ambient condition, Appl. Phys. Lett. 104 (2014) (Article#103105).

[39] L. Li, D. Ye, Y. Yu, L. Liu, Y. Wu, Carbon-based flexible micro-supercapacitor fabrication via mask-free ambient micro-plasma-jet etching, Carbon 111 (2017) 121–127.

[40] W. Sun, X. Chen, Fabrication and tests of a novel three dimensional micro supercapacitor, Microelectron. Eng. 86 (2009) 1307–1310.

[41] H.E.Z. Abidin, A.A. Hamzah, B.Y. Majlis, J. Yunas, N.A. Hamid, U. Abidin, Electrical properties of double stacked *Ppy-PVA* supercapacitor for powering biomedical MEMS devices, Microelectron. Eng. 111 (2013) 374–378.

[42] R.-Z. Li, R. Peng, K.D. Kihm, S. Bai, D. Bridges, U. Tumuluri, Z. Wu, T. Zhang, G. Compagnini, Z. Feng, A. Hu, High-rate in-plane micro-supercapacitors scribed onto photo paper using in-situ femtolaser-reduced graphene oxide/Au nanoparticle microelectrodes, Energy Environ. Sci. 9 (2016) 1458–1467.

[43] T. Tomasevic-Ilic, J. Pesic, I. Milosevic, J. Vujin, A. Matkovic, M. Spasenovic, R. Gajic, Transparent and conductive films from liquid phase exfoliated graphene, Opt. Quant. Electron. 48 (2016) 319.

[44] J.-H. Sung, S.-Joon Kim, S.-H. Jeong, E.-H. Kim, K.-H. Lee, Flexible micro-supercapacitors, J. Power Sources 162 (2006) 1467–1470.

CrossMark

DFT study of optical properties of MoS$_2$ and WS$_2$ compared to spectroscopic results on liquid phase exfoliated nanoflakes

Jelena Pešić[1] · Jasna Vujin[1] · Tijana Tomašević-Ilić[1] · Marko Spasenović[1] · Radoš Gajić[1]

Abstract
We calculate the dielectric function within the framework of the random-phase approximation (RPA) based on DFT ground-state calculations, starting from eigenvectors and eigenvalues. The final goal of our theoretical work is a comparison to corresponding experimental data. We compare our computational results with optical measurements on MoS$_2$ and WS$_2$ nanoflakes. MoS$_2$ and WS$_2$ were exfoliated by ultrasonic treatment in high-boiling point organic solvent and characterized using UV–VIS spectrophotometry. We find that DFT-RPA yields a good, computationally inexpensive first approximation of the imaginary part of the dielectric function, although excitonic effects require more complex code and extra computing power.

Keywords DFT optical properties · MoS$_2$ and WS$_2$ · 2D materials

1 Introduction

Even though graphene is being the most promising two-dimensional material, absence of the gap has imposed limitations of its applications in nanoelectronics and nanophotonics. Transition metal dichalcogenide crystals (TMDCs) emerged as important alternative as a layered 2D materials family with the finite gap and received considerable attention owing to their extraordinary potential for applications in electronics and optics (Pospischil et al. 2014; Baugher et al. 2014; Britnell et al. 2013; Koppens et al. 2014; Ross et al. 2014; Shi 2013; Zhang 2016; Huang 2016; He 2016; Szczesniak 2017). MoS$_2$ and WS$_2$ are part of the family of transition

---

✉ Jelena Pešić
  yelena@ipb.ac.rs

[1] Graphene Laboratory (GLAB) of Center for Solid State Physics and New Materials, Institute of Physics Belgrade, University of Belgrade, Pregrevica 118, 11080 Belgrade, Serbia

 Springer

metal dichalcogenide crystals. They display distinctive properties at a thickness of one and few layers (Butler et al. 2013; Wang et al. 2012; Xu et al. 2014) and very peculiar physics, ranging from trions (Mak et al. 2013) to superconductivity (Szczesniak et al. 2018). They have also attracted much interest for applications in optoelectronics as detectors, photovoltaic devices and light emitters (Pospischil et al. 2014; Baugher et al. 2014; Britnell et al. 2013; Koppens et al. 2014; Ross et al. 2014). MoS_2 and WS_2 are layered crystals in hexagonal structure, consisting of metal atoms sandwiched between two chalchogenide atoms, with covalent interaction within layer and van der Waals interaction between layers. For many applications knowledge of the optical properties is of fundamental importance. Spectroscopic techniques are among the most important methods for research in the field of nanoscience and nanotechnologies. Parallel with the development of experimental methods, computational science becomes a very valuable tool in pursuit for new low-dimensional materials and their characterization. Employing high-end modeling codes, it is possible to simulate from first principles more than a few spectroscopic techniques. The most basic description of light-matter interactions in TMDC thin layers is given by the materials complex dielectric function. Importance of the dielectric function is not only in understanding theoretical concepts underlying interesting properties of TMDCs but it is crucial for the characterization of these materials i.e. the imaginary part of dielectric function is directly related to the absorption. The observed double-peak structure in the optical absorption spectra of monolayer TMDCs is connected to excitonic excitations. These excitons are due to the vertical transition at the K point of the Brillouin zone from a spin-orbit-split valence band to doubly degenerate conduction band (Zhu et al. 2011). For experimental approach, spectroscopic ellipsometry allows determination of material's optical properties in nondestructive manner (Tompkins and McGahan 1999; Liu et al. 2014). The liquid-phase exfoliation is a simple and effective method to exfoliate bulk layered materials into mono- and/or few-layer 2D nanosheets. In this work, high quality TMDC, MoS_2 and WS_2 were prepared in NMP with the similar procedure as our previous works (Matković et al. 2016; Tomašević-Ilić et al. 2016). UV–VIS spectroscopic measurements effectively characterize dispersions by their absorbtion spectra. Using approaches based on density functional theory (DFT), implemented in the Quantum Espresso software package (Giannozzi et al. 2009), we study optical properties of low-dimensional materials, MoS_2 and WS_2. We calculate the dielectric function within the framework of the random-phase approximation (RPA) (Brener 1975) based on DFT ground-state calculations, starting from eigenvectors and eigenvalues. Although the tight-binding approximation prove their efficiency and accuracy in describing low-dimensional bands and energy gaps in TDMC materials (Liu et al. 2013; Shanavas et al. 2015; Szczesniak et al. 2016), even for study of the optical properties (Ghader et al. 2015) we relay on DFT based methods due to their applicability on large spectra of systems joint with simplicity of use. The final goal of this study is a comparison to corresponding experimental data provided by spectroscopic measurements of liquid exfoliated nanoflakes of MoS_2 and WS_2. We use our results for analysis of optical properties of liquid phase exfoliated MoS_2 and WS_2 nanoflakes, as a proven method for analysis of basic optical properties of 2D materials (Pešić et al. 2016).

2 Computational details

For presented analysis, Quantum Espresso (QE) code (Giannozzi et al. 2009), based on DFT, was used. The approach is established on an iterative solution of the Kohn–Sham equations of the DFT in a plane-wave basis set. The ionic positions in the

cell are fully relaxed, in all calculations, to their minimum energy configuration using the Broyden–Fletcher–Goldfarb–Shanno (BFGS) algorithm. We modeled monolayer MoS$_2$ and WS$_2$ with hexagonal unit cell with 3 atoms per unit cell (Fig. 1). For presented analysis, GGA exchange-correlation functional, Perdew–Burke–Ernzerhof (PBE) (Krack 2005) was used. This parameter-free GGA functional, PBE, is known for its general applicability and gives rather accurate results for a wide range of systems. Compared to hybrid, PBE potential is significantly faster, hence more convenient for qualitative description we aim in this discussion. Although LDA is computationally even more affordable, GGA (i.e. PBE) has proven to be closer to experimental results for spectra of properties in low-dimensional materials (Rasmussen 2015; Molina-Sanchez et al. 2015). Additional accuracy that would be obtained with addition of spin orbit correction, however it would lead to significant increase in computational costs (Rasmussen 2015) making this approach obsolete, since we use it for its efficiency. Namely, many-body calculations applying the GW approximation and Bethe–Salpeter equation give good agreement for optical properties, but their computational costs is great comparing to DFT + RPA. Our computationally inexpensive approach gives qualitatively satisfying description. The hexagonal cell parameter c was set to be very large (10–12 Å) in order to simulate vacuum and two-dimensional system and avoid an interaction due to periodicity. The plane wave kinetic energy cutoff of 70 Ry was used and the uniform k-point grid was composed of 4096 points in the first Brillouin zone. In TMDCs van der Waals interaction (Lu et al. 2017) have an important effect on the electronic structure, and in case of multilayer, structures were relaxed to their minimum position, with van der Waals interaction included to obtain proper interlayer distance (using Grimme scheme Grimme 2006). In case of monolayer, there was no need for inclusion of it. Dielectric function $\epsilon(\omega)$ was calculated, in the range 1–20 eV, within the framework of the RPA (Brener 1975) based on DFT ground-state calculations, starting from eigenvectors and eigenvalues, implemented in Quantum Espresso (QE) code as epsilon.x post-processing utility. Matrix elements were accounted only for interband transitions. RPA does not include the nonlocal part of the pseudo-potential and it is not able to include in the calculation the non-local field and excitonic effects. We are interested in the study of the optical properties of this two materials using DFT as a computational inexpensive method for the qualitative description. In QE implementation of the RPA, frequency dependence is computed from an explicit summation of dipole matrix elements and transition energies. Similar theoretical methods were already used to describe the bulk TMDCs (Molina-Sanchez et al. 2015, 2013).
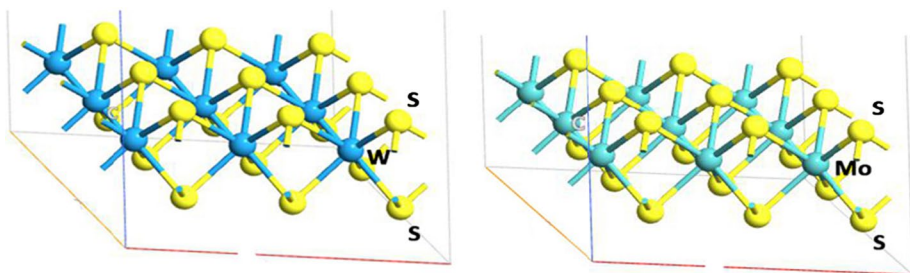
Fig. 1 Structure of monolayer of WS$_2$ and MoS$_2$

3 Synthesis of MoS$_2$ and WS$_2$ dispersions

Liquid Phase Exfoliation (LPE) is the physico-chemical process where thin sheets of van der Waals materials, ie. MoS$_2$ and WS$_2$ are exfoliated from their corresponding bulk materials by ultrasonic treatment in liquids such are organic solvents (Fig. 2). In liquid dispersion flakes mainly range from monolayer to few-layer flakes. For the fabrication of both MoS$_2$ and WS$_2$ dispersion, we followed the protocol described in earlier papers (Matković et al. 2016; Tomašević-Ilić et al. 2016; Panajotović et al. 2016; Vujin et al. 2016). An initial concentration of powders are: MoS$_2$ powder (Sigma Aldrich, Product No. 69860) 24 mg/ml and WS$_2$ powder (Sigma Aldrich Product No.243639) was 12 mg/ml. The mixture was sonicated in a low power sonic bath (Bransonic CPXH Ultrasonic 8 Cleaning Bath) for 14 h in *N*-Methyl-2-pyrrolidone (NMP) (Sigma Aldrich-328634) for both materials. In order to prevent reaggregation and reduce the amount of unexfoliated material, the solutions were centrifuged for MoS$_2$ 1000 rpm for 30 min and WS$_2$ 15 min at 3000 rpm and second centrifuge 6000 rpm for 15 min after we decanted excess of liquid.

4 Characterization of MoS$_2$ and WS$_2$ dispersions

Large quantities of TMDC flakes were observed as few-layer layered nanosheets, confirming the high quality of the prepared LPE samples. The aggregated nanosheets are absent in these SEM images (Fig. 3), which is in favor of quality of exfoliation procedure.

The UV–visible absorption spectra of the nanosheet dispersions in NMP was measured using the UV–VIS Spectrophotometer (Perkin-Elmer Lambda 4B). The quality of the obtained TMDC nanosheets was characterized by SEM (Tescan MIRA3 field-emission gun SEM). Two typical characteristic absorption peaks of MoS$_2$ and WS$_2$ are clearly observed at the region of 600 nm (Fig. 4, which correspond to the A1 and B1 direct excitonic transitions of the TMDC originated from the energy split of valence-band and spin-orbit coupling (Zhu et al. 2011; Coleman et al. 2011). Noteworthily, the splitting between A and B excitonic peaks of WS$_2$ is larger than that of MoS$_2$ because of the much heavier mass of the W atom (Shi 2013). These two peaks indicate that the TMDC are dispersed in NMP as the 2H-phase. The Lambert-Beer law was applied to UV–VIS absorption spectra to calculate TMDCs concentration by estimating the absorbance at distinctive peak (MoS$_2$ at 672 nm and WS$_2$ at 629 nm) by using a cell length of 1 cm and the extinction coefficient of MoS$_2$ ($\alpha = 34.00$ mL mg^{-1} m^{-1}), WS$_2$ ($\alpha = 27.56$ mL mg^{-1} m^{-1}), in NMP solutions, which corresponds to previously reported values (Coleman et al. 2011). The concentration of exfoliated MoS$_2$ is 343 µg ml^{-1} and WS$_2$ is 237 µg ml^{-1} .
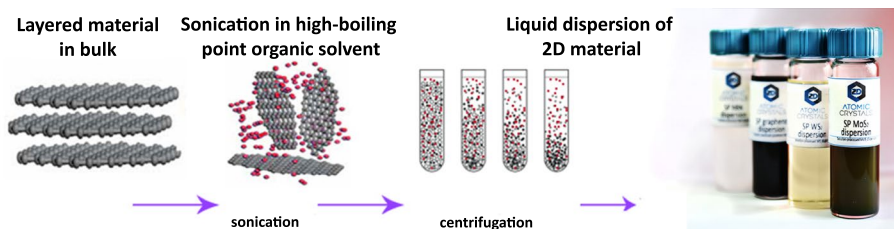
Fig. 2 Procedure of liquid phase exfoliation

Fig. 3 MoS$_2$ (up) and WS$_2$ (down) flakes on Si/SiO2 substrate—Tescan MIRA3 field-emission gun SEM-left. Photos of MoS$_2$ and WS$_2$ dispersions-right
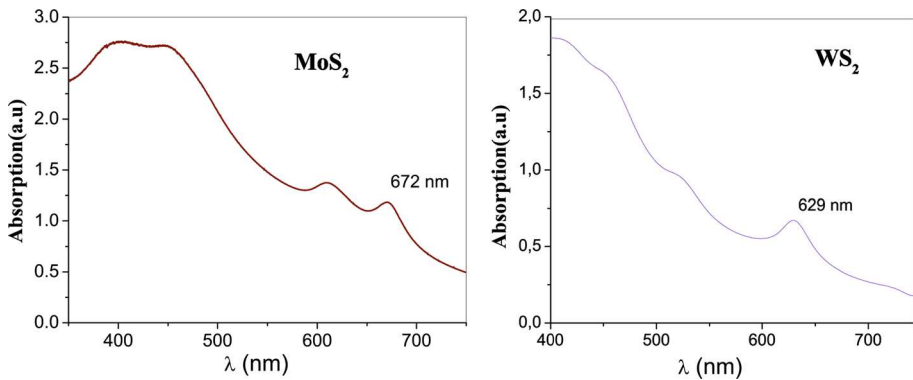
Fig. 4 UV–VIS spectra were taken using Perkin–Elmer Lambda 4B UV–VIS spectrophotometer with quartz cuvettes

5 Results and Discussion

First we calculate the dielectric function for the MoS$_2$ and WS$_2$ monolayer (Fig. 5a). On example of MoS$_2$ monolayer we shall discuss dielectric function. The imaginary part of the

dielectric function for the **E** vector perpendicular to the c axis is presented in the red color and **E** parallel to the c axis is presented in the green on Fig. 5. Four distinct structures on Fig. 5, at 1(2.7), 2(3.7), 3(4.2) and 4(5.3 eV) can be connected to the interband transitions, marked on the inset of the electronic band structure, with 1, 2, 3 and 4 as well. All the interband transition depicted here are mainly due to the transition from the p valence bands of sulfur to the d conduction bands of the molybdenium (Kumar et al. 2012). The peak 1 is determined by the interband transitions from the valence bands I, II below the Fermi energy to the conduction bands I, II and III above the Fermi energy along ΓM and $K\Gamma$ direction. The peak 2 is due the interband transitions from the valence bands II below the Fermi energy to the conduction bands II and III above the Fermi energy along ΓM direction and near the M. The peak 3 exists due to the interband transitions from the valence bands III below the Fermi energy to the conduction bands II and III above the Fermi energy along $K\Gamma$ direction. Peak 4 is determined by the interband transitions from the valence bands IV below the Fermi energy to the conduction band I above the Fermi energy in the vicinity of the M high symmetry point. Our calculations are in agreement with the other similar DFT studies (Kumar et al. 2012) and experimental research as well (Li et al. 2014). All TMDCs have similar band structure and corresponding analysis can be applied on WS_2 monolayer. In Fig. 5 imaginary part of dielectric function of WS_2 is presented. Same as for MoS_2, there are present four distinct peaks originating in same transitions as in MoS_2.

Next we compare the imaginary part of the dielectric function in MoS_2 and WS_2 with experimental results. Figure 6 qualitatively compares experimental results of MoS_2 and WS_2 LPE with DFT+RPA calculations and results obtained using the Kramers–Kronig analysis (Li et al. 2014). The green line represent experimental results, UV–VIS spectra of LPE flakes. Violet lines are DFT + RPA model of MoS_2 and WS_2. The red line is

Fig. 5 The calculated imaginary part of the dielectric function for MoS_2 and WS_2
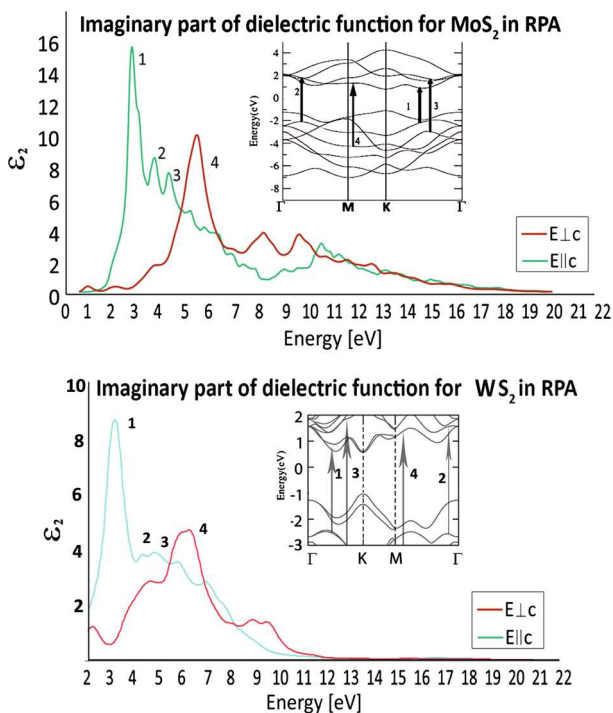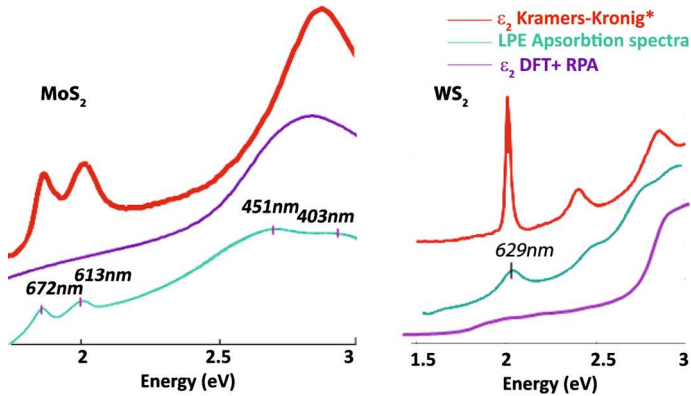
Fig. 6 The qualitative comparison of imaginary part of experimental results and theoretical calculations for MoS_2 and WS_2. Asterisks corresponds to result for the reference Li et al. (2014)

Fig. 7 The calculated imaginary part of the dielectric function for few layers of WS_2
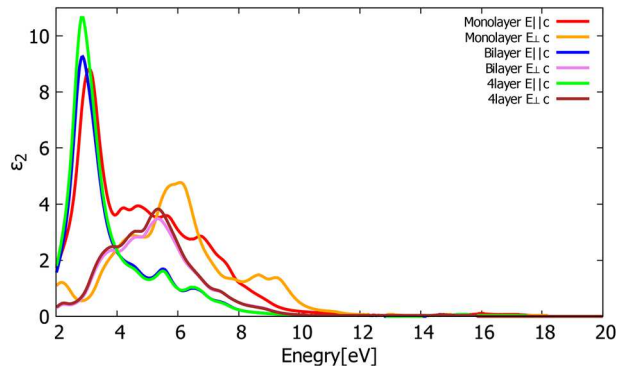
imaginary part of the dielectric function obtained using Kramers–Kronig analysis from the reference Li et al. (2014). Due to the nature of approximation, excitonic effects are not clearly visible in DFT+RPA calculation and characteristic A and B peaks are not present. However both for MoS_2 and WS_2 peaks at around 400 nm (which originate in electronic transitions) are well described.

After analysis of monolayer we proceeded with calculations of few layer structures to observe changes in the imaginary part of dielectric function with increase of number of layers. We compared monolayer with bilayer and 4-layer WS_2, Fig. 7 and conclude its thickness-dependent nature. It can be noticed that thicker structures have higher ϵ_2 in the low energy area. This regular change shows a good agreement with the variation tendency of the density of WS_2 films, as demonstrated in the XRD analysis in ref (Li et al. 2017). Being aware of this effect, a referent model for various thicknesses of TMDCs sheets (ie. number of layers) could be made using DFT-based approach. It is planned to be used as a guide in comparison with UV–VIS spectrophotometry measurement for rapid assessment of thickness of nanoflakes in dispersion.

6 Conclusion

In this paper we studied optical properties i.e. the dielectric function of the monolayer MoS_2 and WS_2 as a monolayer TMDCs, using DFT based techniques. Many effects present due to the exitonic effects demand detail and advanced approach based addition of GW approximation and Bethe–Salpeter equation (but computationally significantly more expensive, time-demanding and resource-consuming), in this kind of the calculations they have been complectly neglected. Thickness-dependent nature of MoS_2 and WS_2 dielctric function was revealed. However, we can conclude that DFT+RPA techniques can be used for quick analysis of the optical properties of these and similar 2D materials, and they provide the reliable and computationally non-expensive solution for the suitable qualitative description.

References

Baugher, B.W.H., et al.: Optoelectronic devices based on electrically tunable p-n diodes in a monolayer dichalcogenide. Nat. Nano **9**(4), 262–267 (2014)

Brener, N.E.: Random-phase-approximation dielectric function for diamond, with local field effects included. Phys. Rev. B **12**(4), 1487–1492 (1975)

Britnell, L., et al.: Strong light-matter interactions in heterostructures of atomically thin films. Science **340**(6138), 1311–1314 (2013)

Butler, S.Z., et al.: Challenges, and opportunities in two-dimensional materials beyond graphene. ACS Nano **7**(4), 2898–2926 (2013)

Coleman, J.N., et al.: Two-dimensional nanosheets produced by liquid exfoliation of layered materials. Science **331**(6017), 568–571 (2011)

Ghader, D., et al.: The electronic band structures and optical absorption spectra for incommensurate twisted few-layers graphene. arXiv:1504.01347v1 (2015)

Giannozzi, P., et al.: QUANTUM ESPRESSO: a modular and open-source software project for quantum simulations of materials. J. Phys. Condens. Matter **21**, 395502 (2009). http://www.quantum-espresso.org

Grimme, S.: Semiempirical GGA-type density functional constructed with a longrange dispersion correction. J. Comp. Chem. **27**(15), 1787–1799 (2006)

He, X.: Strain engineering in monolayer WS_2, MoS_2, and the WS_2/MoS_2 heterostructure. Apl. Phys. Lett. **109**(17), 173105 (2016)

Huang, G.Q.: Dynamical stability and superconductivity of Li-intercalated bilayer MoS_2: A first-principles prediction. Phys. Rev. B **93**(10), 104511 (2016)

Koppens, F.H.L., et al.: Photodetectors based on graphene, other two-dimensional materials and hybrid systems. Nat. Nano **9**, 780–793 (2014)

Krack, M.: Pseudopotentials for H to Kr optimized for gradient-corrected exchange-correlation functionals. Theor. Chem. Acc. **114**(1–3), 145–152 (2005)

Kumar, A., et al.: A first principle comparative study of electronic and optical properties of 1HMoS2 and 2HMoS2. Mat. Chem. Phys. **135**, 755–761 (2012)

Li, Y., et al.: Measurement of the optical dielectric function of monolayer transition-metal dichalcogenides: MoS_2, $MoSe_2$, WS_2, and WSe_2. Phys. Rev. B **90**(20), 205422 (2014)

Li, W., et al.: Broadband optical properties of large-area monolayer CVD molybdenum disulfide. Phys. Rev. B **90**(19), 195434 (2014)

Li, Da-Hai, et al.: Dielectric functions and critical points of crystalline WS_2 ultrathin films with tunable thickness. Phys. Chem. Chem. Phys. **19**, 12022 (2017)

Liu, G.-B., et al.: Three-band tight-binding model for monolayers of group-VIB transition metal dichalcogenides. Phys. Rev. B **88**(8), 085433 (2013)

Liu, H.-L., et al.: Optical properties of monolayer transition metal dichalcogenides probed by spectroscopic ellipsometry. Appl. Phys. Lett. **105**, 20 (2014)

Lu, N., et al.: Twisted MX$_2$/MoS$_2$ heterobilayers: effect of van der Waals interaction on the electronic structure. Nanoscale **9**, 19131–19138 (2017)

Mak, K.F., et al.: Tightly bound trions in monolayer MoS$_2$. Nat. Mater. **12**(3), 207–211 (2013)

Matković, A., et al.: Enhanced sheet conductivity of LangmuirBlodgett assembled graphene thin films by chemical doping. 2D Mater. **3**(1), 015002 (2016)

Molina-Sanchez, A., et al.: Effect of spin-orbit interaction on the optical spectra of single-layer, double-layer, and bulk MoS$_2$. Phys. Rev. B **88**(4), 045412 (2013)

Molina-Sanchez, A., et al.: Vibrational and optical properties of MoS2: from monolayer to bulk. Surf. Sci. Rep. **70**(4), 554–586 (2015)

Panajotović, R., et al.: Modifications of Lipid/2D-Material Heterostructures by SEM, Book of Abstracts, SPIG 2016, 182–185 (2016)

Pešić, J., et al.: Ab-initio study of the optical properties of the Li-intercalated graphene and MoS$_2$. Opt Quant Electron **48**, 368 (2016)

Pospischil, A., et al.: Solar-energy conversion and light emission in an atomic monolayer p-n diode. Nat. Nano **9**(4), 257–261 (2014)

Rasmussen, F.A.: Computational 2D materials database: electronic structure of transition-metal dichalcogenides and oxides. J. Phys. Chem. C **119**, 13169–13183 (2015)

Ross, J., et al.: Electrically tunable excitonic light-emitting diodes based on monolayer WSe$_2$ p-n junctions. Nat. Nano **9**(4), 268–272 (2014)

Shanavas, K.V., et al.: Effective tight-binding model for MX$_2$ under electric and magnetic fields. Phys. Rev. B **91**(23), 235145 (2015)

Shi, H.: Quasiparticle band structures and optical properties of strained monolayer MoS$_2$ and WS$_2$. Phys. Rev. B **87**(15), 155304 (2013)

Szczesniak, D., et al.: Complex band structures of transition metal dichalcogenide monolayers with spin-orbit coupling effects. J. Phys. Condens. Matter **28**(35), 355301 (2016)

Szczesniak, R.: Metallization and superconductivity in Ca-intercalated bilayer MoS$_2$. J. Phys. Chem. Solids **111**, 254–257 (2017)

Szczesniak, R., Durajski, A.P., Jarosik, M.W.: Strong-coupling superconductivity induced by calcium intercalation in bilayer transition-metal dichalcogenides. Front. Phys. **13**(2), 137401 (2018)

Tomašević-Ilić, T., et al.: Transparent and conductive films from liquid phase exfoliated graphene. Opt. Quant. Electron. **48**, 319 (2016)

Tompkins, H.G., McGahan, W.A.: Spectroscopic ellipsometry and reflectometry: a users guide. Wiley, New York (1999)

Vujin, J., et al.: Physico-Chemical Characterization Of Lipid-2d-Materials Self-Assembly For Biosensors, Book of Abstracts RAD 2016, 58 (2016)

Wang, Q.H., et al.: Electronics and optoelectronics of two-dimensional transition metal dichalcogenides. Nat. Nano **7**, 699–712 (2012)

Xu, X., et al.: Spin and pseudospins in layered transition metal dichalcogenides. Nat. Phys. **10**, 343–350 (2014)

Zhang, J.-J.: Strain-enhanced superconductivity of MoX$_2$(X=S or Se) bilayers with Na intercalation. Phys. Rev. B **93**(15), 155430 (2016)

Zhu, Z.Y., Cheng, Y.C., Schwingenschlogl, U.: Giant spin-orbit-induced spin splitting in two-dimensional transition-metal dichalcogenide semiconductors. Phys. Rev. B **84**(15), 153402 (2011)

CrossMark

Transparent and conductive films from liquid phase exfoliated graphene

**Tijana Tomašević-Ilić[1] · Jelena Pešić[1] · Ivana Milošević[1] ·
Jasna Vujin[1] · Aleksandar Matković[1] · Marko Spasenović[1] ·
Radoš Gajić[1]**

Abstract We describe transparent and conductive films of liquid-phase exfoliated graphene deposited with the Langmuir–Blodgett (LB) method. Graphene sheets (GS) were exfoliated from graphite by ultrasonic treatment in N-Methyl-2-pyrrolidone (NMP) and N, N-dimethylacetamide (DMA) solvents. For comparison, graphene sheets were also exfoliated in a water solution of surfactants. We confirm a higher exfoliation rate for surfactant-based processing compared to NMP and DMA. Furthermore, we demonstrate that our films exfoliated in NMP and DMA, deposited with LB and annealed have a higher optical transmittance and lower sheet resistance compared to films obtained with vacuum filtration, which is a necessary step for GS exfoliated in water solutions. The structural, optical and electrical properties of graphene layers were characterized with scanning electron microscopy, atomic force microscopy, UV/VIS spectrophotometry and sheet resistance measurements. Our facile and reproducible method results in high-quality transparent conductive films with potential applications in flexible and printed electronics and coating technology.

Keywords Graphene · LPE · Langmuir–Blodgett assembly

1 Introduction

Transparent conductors are an essential part of many optical devices. Many of the thin metallic or metal oxide films used as transparent conductors (Granqvist 2007) exhibit nonuniform absorption across the visible spectrum (Phillips et al. 1994), or they are

✉ Tijana Tomašević-Ilić
ttijana@ipb.ac.rs

[1] Center for Solid State Physics and New Materials, Institute of Physics, University of Belgrade, Pregrevica 118, 11080 Belgrade, Serbia

Springer

chemically unstable, or both (Scott et al. 1996; Schlatmann et al. 1996). The experimental discovery of graphene (Novoselov et al. 2004) brought a new alternative to this field. Graphene is a material with high optical transparency, large carrier mobility, good chemical stability, and mechanical strength, making it an excellent choice for transparent electrodes in various optoelectronic devices (Blake et al. 2008).

Although graphene is a natural choice for transparent conductive films (Bonaccorso et al. 2010), the feasibility of its mass production is essential for applications. In order to produce large quantities of graphene Blake et al. (Blake et al. 2008) and Hernandez et al. (2008) developed a method of graphene production using solvent assisted exfoliation (or liquid phase exfoliation, LPE) of bulk graphite, which is simpler and less costly than chemical vapor deposition and returns a higher yield than mechanical exfoliation (Novoselov et al. 2004, 2005). LPE allows the possibility to scale up the synthesis of graphene making it economically available in a large amount, presenting a promising route for large-scale production (Paton et al. 2014).

Numerous research efforts followed up to increase the concentration and quality of the graphene flakes produced. One of the most promising synthesis routes for LPE graphene is non-covalent exfoliation using solvents that have surface energy values comparable to that of graphite (Hernandez et al. 2008). Typically ultrasound assists the separation of graphene flakes from graphite powder in solvent. Exfoliation conditions such as the initial concentration of graphite powder, sonication time (Khan et al. 2010), solvent type (O'Neill et al. 2011; Bourlinos et al. 2009; Hernandez et al. 2010; Lotya et al. 2009; Guardia et al. 2011), and possible filtration (Khan et al. 2011) were tuned in order to optimize the yield and quality of graphene dispersions. These graphene dispersions can be used to form films by various methods, for example spray coating (Blake et al. 2008), vacuum filtration (Hernandez et al. 2008; Lotya et al. 2009) or Langmuir–Blodgett assembly (LBA) (Cote 2009; Kim et al. 2013; Li et al. 2008).

In this study, graphene sheets (GS) were exfoliated from graphite by ultrasonic treatment in organic solvents with high boiling points, N-Methyl-2-pyrrolidone (NMP), N, N-dimethylacetamide (DMA), and for comparison, in a water solution of surfactant, sodium dodecylbenzenesulfonate (SDBS) and Pluronic P-123 (P-123). The graphene dispersions from NMP and DMA were used to form films by controlled deposition of few-layer graphene using the Langmuir–Blodgett (LB) method on a water–air interface. We confirm a higher exfoliation rate for surfactant-based processing, but demonstrate that our films exfoliated in organic solvents with high boiling points and deposited with LB have a higher optical transmittance and lower sheet resistance compared to films obtained with vacuum filtration, which is a necessary step for GS exfoliated in water solutions. The structural, optical and electrical properties of graphene layers were characterized with scanning electron microscopy, atomic force microscopy, UV/VIS spectrophotometry and sheet resistance measurements.

2 Experimental procedure

All chemicals used were purchased from Sigma Aldrich: graphite powder (product number 332461), N-Methyl-2-pyrrolidone (product number 328634), N, N-dimethylacetamide (product number 38840), sodium dodecylbenzenesulfonate (product number 289957) and Pluronic P-123 (product number 435467). The particular graphite powder product was chosen for its large initial flake size, which should result in the largest possible graphene

flakes after exfoliation. Stock solutions of SDBS and P-123 of different concentrations were prepared in deionized water (resistivity 18 MΩ) by stirring overnight. A range of graphene dispersions were prepared. A typical sample was prepared by dispersing graphite in the desired solvent using from 30 min to 14 h of sonication in a low power sonic bath. The resulting dispersion was centrifuged for 60 min at 3000 rpm in order to reduce the amount of unexfoliated graphite.

The graphene sheets exfoliated from graphite by ultrasonic treatment in NMP were used to form films at a water–air interface. Beakers filled with deionized water, 10 mL volume, were used for film formation. A 1.5–2 vol% of GS + NMP was added to the interface with a continuous flow rate of 5–10 mL/s (Fig. 1a). This set of parameters provides enough surface pressure for the film to be close-packed. After the film is formed, it is slowly scooped onto the targeted substrate (Fig. 1b), as shown in our previous work (Matković et al. 2016). PET and SiO₂/Si were used as substrates. As it has been shown that annealing decreases sheet resistance due to solvent evaporation (Hernandez et al. 2008; Lotya et al. 2009), some of these deposited films were annealed. Annealing was carried out in a tube furnace at 250 °C in an argon atmosphere for 2 h.

For optical characterization, UV–VIS spectra were taken using a SUPER SCAN Varian spectrophotometer with quartz cuvettes. The resistance of each sample was measured in a two-point probe configuration, and the sheet resistance was obtained by including the sample geometry factors. AFM measurements were taken with an atomic force microscope, NTEGRA Spectra, in tapping mode. SiO₂/Si was chosen as a substrate for AFM due to its low surface roughness. The lateral profile of graphene flakes was analyzed with a Tescan MIRA3 field-emission gun SEM.

3 Results and discussion

We optimized for high graphene concentration and large flake size, tuning exfoliation conditions such as initial graphite concentration, sonication time and solvent type. The Lambert–Beer law was applied to UV–VIS absorption spectra to find graphene concentration. The concentration was estimated from the absorbance at 660 nm by using the extinction coefficient of graphene ($\alpha = 13.90$ mL mg^{-1} m^{-1}) previously determined in surfactant/water solutions (Hernandez et al. 2008; Lotya et al. 2009; Guardia et al. 2011) and ($\alpha = 24.60$ mL mg^{-1} m^{-1}) in NMP and DMA solutions (Hernandez et al. 2008). Figure 2a depicts a higher final concentration for surfactant-based processing for all initial concentrations of graphite powder, from 0.5 to 18 mg mL^{-1}. The most commonly used deposition technique for LPE GS is vacuum filtration. This is a necessary step for GS exfoliated in water solutions. For GS films formed by evaporation of a high boiling point

Fig. 1 Schematic representations of **a** LBA GS film formation, **b** scooping of the film onto a targeted substrate
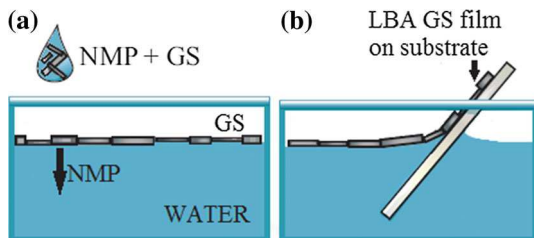
solvent, one of the biggest problems is that graphene flakes aggregate during evaporation (O'Neill et al. 2011) hindering fine control over the film thickness (Hernandez et al. 2008). This can be avoided by depositing with LB, which allows reliable and reproducible thickness control and prevents further agglomeration of graphene flakes during drying (Kim et al. 2013). We chose the dispersion in NMP with the highest graphene concentration (Fig. 2b) for experiments on LB films.

A single LB deposition resulted in films with an average thickness 3.3 nm, as measured with AFM, indicating an average GS thickness of 10 layers (Fig. 3).

Figure 4 shows optical transmittance versus sheet resistance for varying number of LB depositions on PET, compared to graphene film obtained with vacuum filtration of GS exfoliated from the same graphite precursor using the same experimental procedure (Hernandez et al. 2008; Lotya et al. 2009) before and after annealing. The highest transparency for a single LB film deposition prior to annealing was found to be about 83 %, which is between 20 and 40 % higher than the transmittance that can be accomplished with vacuum-filtration. The sheet resistance of one LB film deposition is between 70 and 250 kΩ/sq, 2–5 times lower than sheet resistance achieved with vacuum filtration without annealing. Increasing the graphene film thickness with additional LB depositions led to consistent increases in conductivity, but a decrease in transparency. Our graphene films for three LB depositions prior to annealing have comparable sheet resistance but higher optical transmittance compared to vacuum-filtered films after annealing.

The electrical conductivity is affected by the size and connectivity of the flakes as well as the thickness of the films. Our average GS diameter was is 120 nm, as measured with SEM (Fig. 5). SEM also revealed the presence of pinholes between flakes for a single LB deposition, which probably results in parasitic sheet resistance (Fig. 5a). In order to remove the residual solvent between the overlapping flakes, which may affect transport, we employed thermal annealing. Annealing does not repair the holes and other irreversible defects (Fig. 5b), but it can remove residual solvents, improving the coupling between graphene flakes and hence decreasing sheet resistance. For a single LB deposition, annealing reduced sheet resistance by about six times, without considerably decreasing transparency (Fig. 4). The sheet resistance of a singly deposited film after annealing was found to be between 10 and 20 kΩ/sq, a significant improvement over other published data. After annealing we performed a second LB deposition and achieved sheet resistance of
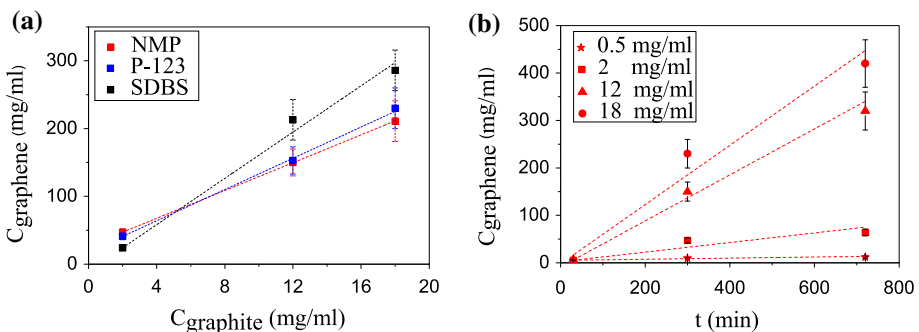
Fig. 2 Concentration of dispersed graphene: a in different solutions for different initial graphite concentration and sonication time of 5 h, b in NMP for different sonication time and different initial graphite concentration
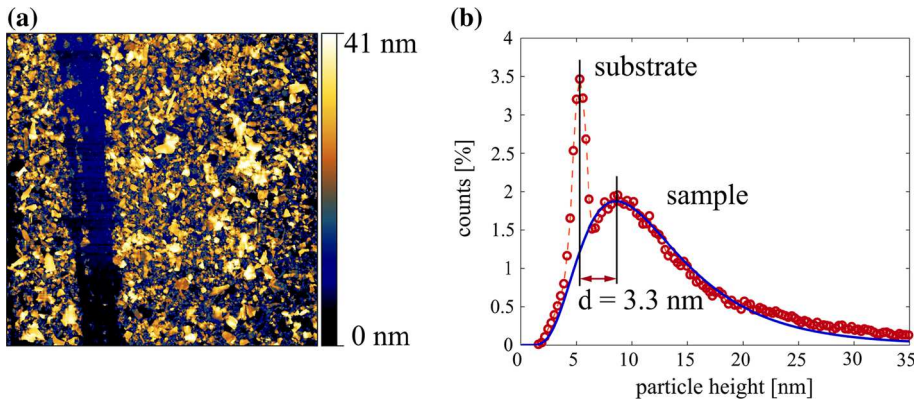
Fig. 3 **a** AFM image of a LB graphene film on a SiO₂/Si substrate, **b** an LB GS film/substrate height histogram fitted with a log-normal curve
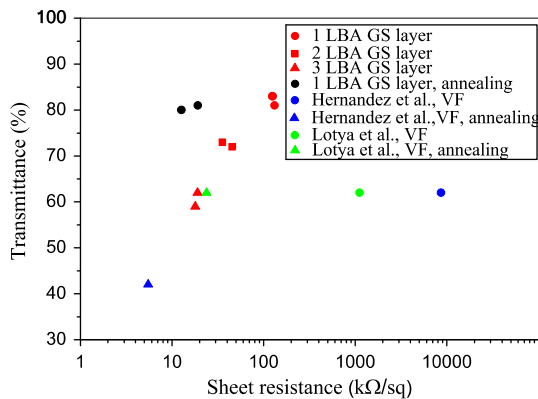
Fig. 4 Optical transmittance versus sheet resistance for varying number of LB deposition of graphene sheets on PET exfoliated in NMP before (*red*) and after annealing (*black*), compared to graphene films obtained with vacuum filtration in the same solvent (*blue*) (Hernandez et al. 2008) and graphene films obtained with vacuum filtration in surfactant/water solutions (*green*) (Lotya et al. 2009) before and after annealing. (Color figure online)
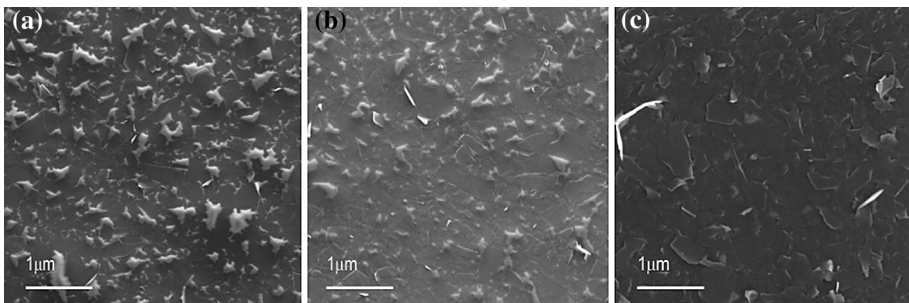
Fig. 5 SEM images of: **a** singly deposited LB film on a glass substrate, **b** the same film after annealing, **c** two LB depositions with an annealing step in between

3 kΩ/sq and a transparency of more than 70 %. Decreased resistance is the result of reduced density of pinholes (Fig. 5c) as well as increased film thickness.

4 Conclusion

In summary, we have shown that Langmuir–Blodgett assembly of multi-layer graphene sheets produced from liquid phase exfoliation of graphite powder in solvents can be used to fabricate transparent and conductive films. The sheet resistance of deposited LBA GS layers was found to be between 15 and 250 kΩ/sq, with transmittance between 60 and 85 %, depending on the number of deposited LBA graphene layers. The conductivity of these LBA films can be further increased by about six times with annealing, without considerably decreasing transparency. Optoelectronic properties of these films are much better compared to graphene films obtained with vacuum filtration of GS exfoliated with the same experimental procedure, which is the most commonly used deposition technique for LPE GS. Ours is a facile, reproducible and low-cost technique for transparent conductive films with potential applications in coating technology.

References

Blake, P., et al.: Graphene-based liquid crystal device. Nano Lett. **8**, 1704–1708 (2008)

Bonaccorso, F., et al.: Graphene photonics and optoelectronics. Nat. Photonics **4**, 611–622 (2010)

Bourlinos, A.B., et al.: Liquid-phase exfoliation of graphite towards solubilized graphenes. Small **5**, 1841–1845 (2009)

Cote, L.J.: Langmuir–Blodgett assembly of graphite oxide single layers. J. Am. Chem. Soc. **131**, 1043–1049 (2009)

Granqvist, C.G.: Transparent conductors as solar energy materials: a panoramic review. Sol. Energy Mater. Sol. Cells **91**, 1529–1598 (2007)

Guardia, L., et al.: High-throughput production of pristine grapheme in an aqueous dispersion assisted by non-ionic surfactants. Carbon **49**, 1653–1662 (2011)

Hernandez, Y., et al.: High-yield production of graphene by liquid-phase exfoliation of graphite. Nat. Nanotechnol. **3**, 563–568 (2008)

Hernandez, Y., et al.: Measurement of multicomponent solubility parameters for graphene facilitates solvent discovery. Langmuir **26**, 3208–3213 (2010)

Khan, U., et al.: High-concentration solvent exfoliation of graphene. Small **6**, 864–871 (2010)

Khan, U., et al.: Solvent-exfoliated graphene at extremely high concentration. Langmuir **27**, 9077–9082 (2011)

Kim, H.K., et al.: Optoelectronic properties of graphene thin films deposited by a Langmuir–Blodgett assembly. Nanoscale **5**, 12365–12374 (2013)

Li, X., et al.: Highly conducting graphene sheets and Langmuir–Blodgett films. Nat. Nanotechnol. **3**, 538–542 (2008)

Lotya, M., et al.: Liquid phase production of graphene by exfoliation of graphite in surfactant/water solutions. J. Am. Chem. Soc. **131**, 3611–3620 (2009)

Matković, A., et al.: Enhanced sheet conductivity of Langmuir-Blodgett assembled graphene thin films by chemical doping. 2D Mater. **3**(1), 015002 (2016)

Novoselov, K.S., et al.: Electric field effect in atomically thin carbon. Science **306**, 666–669 (2004)

Novoselov, K.S., et al.: Two-dimensional atomic crystals. Natl. Acad. Sci. U.S.A. **102**, 10451–10453 (2005)

O'Neill, A., et al.: Graphene dispersion and exfoliation in low boiling point solvents. J. Phys. Chem. C **115**, 5422–5428 (2011)

Paton, K.R., et al.: Scalable production of large quantities of defect-free few-layer graphene by shear exfoliation in liquids. Nat. Mater. **13**, 624–630 (2014)

Phillips, J.M., et al.: Transparent conducting thin films of GalnO3. Appl. Phys. Lett. **65**, 115–117 (1994)

Schlatmann, A.R., et al.: Indium contamination from the indium–tin–oxide electrode in polymer light emitting diodes. Appl. Phys. Lett. **69**, 1764–1766 (1996)

Scott, J.C., et al.: Degradation and failure of MEH-PPV light-emitting diodes. J. Appl. Phys. **79**, 2745–2751 (1996)

Enhanced sheet conductivity of Langmuir–Blodgett assembled graphene thin films by chemical doping

2D Materials

Enhanced sheet conductivity of Langmuir–Blodgett assembled graphene thin films by chemical doping

Aleksandar Matković[1], Ivana Milošević[1], Marijana Milićević[1], Tijana Tomašević-Ilić[1], Jelena Pešić[1], Milenko Musić[1], Marko Spasenović[1], Djordje Jovanović[1], Borislav Vasić[1], Christopher Deeks[2], Radmila Panajotović[1], Milivoj R Belić[3] and Radoš Gajić[1]

1   Center for Solid State Physics and New Materials, Institute of Physics, University of Belgrade, Pregrevica 118, 11080 Belgrade, Serbia
2   Thermo Fisher Scientific, Unit 24, The Birches Industrial Estate, East Grinstead, RH19 1UB, UK
3   Texas A & M University at Qatar, PO Box 23874 Doha, Qatar

E-mail: amatkovic@ipb.ac.rs

Keywords: graphene, nitric acid doping, Langmuir–Blodgett assembly, enhanced conductivity

Supplementary material for this article is available online

Abstract

We demonstrate a facile fabrication technique for highly conductive and transparent thin graphene films. Sheet conductivity of Langmuir–Blodgett assembled multi-layer graphene films is enhanced through doping with nitric acid, leading to a fivefold improvement while retaining the same transparency as un-doped films. Sheet resistivity of such chemically improved films reaches 10 kΩ/□, with optical transmittance 78% in the visible. When the films are encapsulated, the enhanced sheet conductivity effect is stable in time. In addition, stacking of multiple layers, as well as the dependence of the sheet resistivity upon axial strain have been investigated.

1 Introduction

Graphene has a multitude of potential applications from high-speed electronics, to energy storage and conversion, to use as transparent conductor [1–3]. As graphene technology matures, applications are moving from the lab to the market, and the performance-to-cost ratio is becoming a crucial parameter in technology adoption, raising the importance of scalable and cost effective routes for production of graphene and related materials [4–7].

Transparent conductive electrodes (TCEs) [8] are an exemplary technology for which graphene offers key advantages compared to established standards. The unique properties that graphene TCEs offer are flexibility [9], thermal and chemical stability [10, 11], functionalization [12] and ease of integration with organic semiconductors [13–15]. Therefore, the use of graphene has already been demonstrated in photovoltaic solar cells [11, 16–18], liquid crystal displays [10], touch-screen panels [19], organic light emitting diodes [20, 21] and many others.

Most of these applications currently rely on graphene obtained through chemical vapor deposition (CVD) [22–24]. Although the CVD process produces some of the highest quality graphene films [25], there are several drawbacks of this technique. CVD of graphene requires high growth temperatures, a vacuum environment and transfer from the metallic substrate, during which the costly metal is usually sacrificed [26]. Nonetheless, multiple layers of CVD graphene grown on copper, transferred, stacked [27] and chemically doped [19, 28] have managed to surpass the industry standard [8] for TCEs set by indium–tin–oxide.

A low-cost alternative to CVD is solution-processed synthesis of graphene and related materials, the first experiments of which yielded graphene oxide [29–31]. Solution-processed sheets of reduced graphene oxide are functionalized with hydroxyls and epoxides and cannot be fully reduced to graphene, which limits film conductance. This issue can be overcome by using a non-covalent liquid phase exfoliation (LPE) of graphite in organic solvents with matching surface energy. LPE was first demonstrated for graphene [10, 32, 33], and then adopted for other two-dimensional materials such as boron-nitride, MoS_2, WS_2, WSe_2 and other [7, 34–36]. LPE of graphite results in a dispersion of graphene and multi-layer graphene sheets (GSs) in the solvent. There are many ways
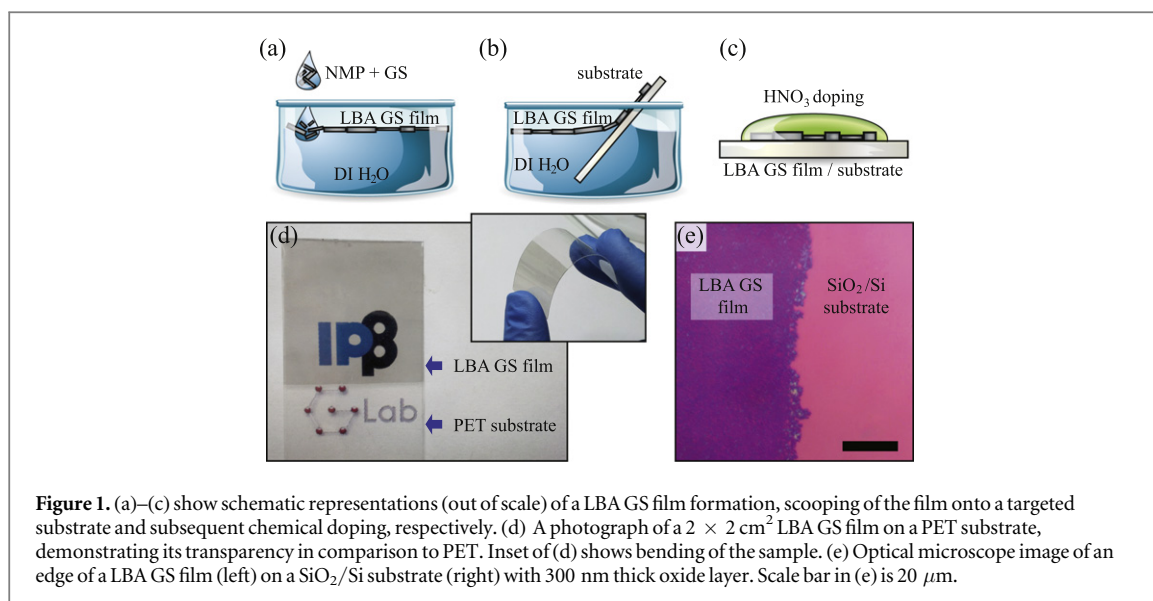
Figure 1. (a)–(c) show schematic representations (out of scale) of a LBA GS film formation, scooping of the film onto a targeted substrate and subsequent chemical doping, respectively. (d) A photograph of a 2 × 2 cm^2 LBA GS film on a PET substrate, demonstrating its transparency in comparison to PET. Inset of (d) shows bending of the sample. (e) Optical microscope image of an edge of a LBA GS film (left) on a SiO$_2$/Si substrate (right) with 300 nm thick oxide layer. Scale bar in (e) is 20 μm.

to deposit these sheets onto a targeted substrate, for example spray coating [10], ink-jet printing [37–39], vacuum filtration [31, 40], Langmuir–Blodgett assembly (LBA) [41–44], or self-assembly on a liquid–liquid interface [45–47]. Still, the electronic conductance of LPE films is inferior to that of CVD graphene, and any improvement is a step towards industrial applications of solution processed graphene.

We make transparent conductive films of multilayer GSs on flexible polyethylene terephthalate (PET) by LBA on a water–air interface. The sheets adhere strongly to the PET substrate, which allows immersion into other liquids without the risk of the film washing away. We make use of the strong adhesion to chemically dope the graphene in nitric acid for enhanced conductivity, and to stack multiple films on top of each other, opening a gateway to liquid phase assembly of Van der Waals heterostructures [36, 48, 49]. The power of this method is demonstrated by the fivefold reduction in sheet resistivity for a single LBA layer, while maintaining the same optical transparency of the unperturbed films.

We show that LBA GS films can be very effectively p-doped by nitric acid, making them a more suitable low-cost alternative to CVD graphene for various TCE applications. As indicated by the work function measurements and by the measurements of the sheet resistivity under axial strain, chemical doping does not only increase carrier concentration of individual GSs, but also reduces the contact resistance between GSs, which additionally contributes to a larger reduction factor of the sheet resistivity.

2 LBA GS film fabrication and morphological characterization

2.1 Preparation of GS dispersion
As a starting material for the formation of LBA layers, a dispersion of GSs in *N*-methylpyrrolidone (NMP) has

been used. The dispersion fabrication process is based on the earlier established protocol [32]. An initial concentration of graphite powder (Sigma Aldrich-332461) was 18 mg ml^{-1} in NMP (Sigma Aldrich-328634). The solution was sonicated in a low-power ultrasonic bath for 14 h, and centrifuged for one hour at 3000 rpm immediately after sonication. The results of this process are GSs in solution, with a concentration of 0.36 mg ml^{-1}. The concentration was determined via UV–VIS spectrophotometry (SUPER SCAN, Varian) [32]. This particular set of LPE parameters was chosen since the resulting dispersion of GSs in NMP was found to be stable for over six months.

2.2 Langmuir–Blodgett assembly
GSs suspended in NMP were used to fabricate transparent and conductive films by LBA at a water–air interface [43]. Since the LPE process introduces a low degree of oxidation and covalent functionalization, resulting GSs have high hydrophobicity, which is very favorable for the formation of LBA layers [41]. Furthermore, driven by the minimization of interfacial energy, LBA produces a close packed structure of GSs [45]. A schematic representation of LBA GS film formation is presented in figure 1(a). Beakers filled with deionized water (18.2 MΩ) with a water–air interface surface-to-water volume ratio of 0.5 cm^{-1} were used for film formation. A 1.5–2 vol% of GS +NMP was added to the interface with a continuous flow rate of 5–10 μl s^{-1}. A closely packed LBA GS film was found to form on the water–air interface with this set of parameters. Formation of the LBA film was found to be self-limiting, meaning that prior to the film formation on the whole given surface, added GSs are fixed at the interface, and after the complete film was formed, any additional GSs fall through the interface to the bottom of the beaker. Only several microliters of the GS+NMP solution are needed to

fabricate several square centimeters of film. When scaled up, one liter of GS+NMP solution would be sufficient to produce 150×150 m^2 of LBA GS films. Compared to CVD graphene, fabrication cost of these TCEs would be at least three orders of magnitude smaller [4].

2.3 Deposition on a substrate and chemical doping

Interestingly, as proposed by Kim *et al* [43], this process dissolves NMP in the water, effectively removing most of the solvent from the graphene layer. After the film is formed, it is slowly scooped onto the targeted substrate, as schematically presented in figure 1(b). The substrate was either pre-positioned vertically at the edge of the beaker, or was introduced after the LBA film was formed, puncturing the film near the edge of the beaker. Films are then left to dry for several minutes in ambient conditions. After the films were transferred onto the targeted substrates their sheet conductivity was enhanced by chemical doping. This was achieved either by dipping into or covering LBA GS films with a 65% solution of nitric acid in water (see figure 1(c)), followed by quick drying with an air gun.

Our procedure yields quality films on all tested substrates, including SiO$_2$/Si, quartz, glass and PET. We typically pre-fabricated ~50 nm thick gold electrodes on the substrates prior to GS deposition. Figures 1(d) and (e) show LBA GS films on the PET and SiO$_2$/Si substrate, respectively. Films fabricated with this method are uniform over the entire substrate area. Up to several square centimeters of uniform LBA GS films on various substrates were fabricated using this technique, with sheet conductivity and optical transparency not varying more than 5% from the mean value over the entire film.

2.4 Film morphology

The morphology of the obtained LBA GS films was characterized with atomic force microscopy (AFM) and scanning electron microscopy (SEM). AFM measurements were carried out on an atomic force microscope, NTEGRA Spectra, in tapping mode. A typical AFM profile of an LBA GS film on a SiO$_2$/Si substrate is shown in figure 2(a). SiO2/Si was chosen as a substrate for AFM due to its low surface roughness. Figure 2(b) shows a height histogram of a 5×5 μm^2 AFM topography image containing a sharp edge of the LBA GS layer (inset). Ten height histograms of sample/substrate edge areas were used to estimate the thickness of LBA GS films. Each histogram had two clearly resolved peaks corresponding to LBA GS film and the substrate. An average film thickness was estimated as a peak-to-peak distance. While the substrate peak is narrow, due to the low roughness of the SiO$_2$, (left peak in figure 2(b)), the LBA GS film has a much broader height distribution. The sample peak was fitted with a log-normal curve, yielding a mean

film thickness (3.4 ± 0.7) nm. This indicates that LBA GS films have an average thickness of ~10 layers.

The lateral profile of graphene flakes was analyzed with a Tescan MIRA3 field-emission gun SEM. A histogram of flake diameter is presented in figure 2(c). The distribution of flake diameters from six 5×5 μm^2 SEM images (~2000 flakes) was fitted with a log-normal curve, giving an average flake diameter of 120 nm. Both AFM and SEM images were used to estimate a surface coverage of over 90%.

3 Results and discussion

3.1 Nitric acid doping

The key result of this study is doping of LBA GS films with nitric acid for improved sheet conductivity. Chemical doping of graphene can be accomplished with various liquids, vapors and polymers [10, 16, 17, 19, 28, 50–53]. One of the most efficient p-type chemical dopants of graphite and graphene is nitric acid [19, 28, 52, 54, 55]. Nitric acid has been used to chemically dope CVD graphene, and reduce the sheet resistivity by a factor of two to three [17, 19, 28, 50]. It was also used to chemically dope reduced GO [53]. Nitric acid doping of graphene was found to be very favorable for photovoltaic solar cells, where graphene is used as a top anode [16, 17, 50, 56]. Besides a reduction in sheet resistivity, the doping increases graphene's work function from about 4.5 to 5 eV, making these TCEs more suitable anode electrodes for various types of hybrid solar cells [17, 50, 52, 56, 57]. Recently, nitrogen-doped reduced GO and carbon have been demonstrated to show enhancement in energy storage [58, 59]. In the following sections we discuss the results of doping LBA GS films with nitric acid.

3.2 Nitric acid exposure time

In order to determine optimal conditions for chemical doping, the exposure time of a single layer LBA GS layer to nitric acid was varied between 10 s and 2 h. Figure 3(a) shows the exposure time dependent reduction factor of the sheet resistivity, obtained as the ratio of the sheet resistivity prior and after the doping (R_{ND}/R_D). Even after only 30 s of the exposure, the reduction factor greater than four was achieved, and after several minutes the reduction factor was found to saturate at (5 ± 1). In order to ensure the control over chemical doping, the exposure time of 5 min was chosen as an optimal value in this study.

3.3 Time stability of the enhanced conductivity effect

Considering that nitric acid is volatile and that dopants can be desorbed from the sample, the stability of the sheet resistivity was examined over an extended period of time. Two batches of LBA GS films were prepared,

Figure 2. (a) An AFM topography image of a LBA graphene film on a SiO_2/Si substrate. Scale bar is 5 μm. (b) An LBA GS film/substrate height histogram obtained from a 5×5 μm^2 AFM topography image (inset), fitted by a log-normal curve (solid line). The height of the film has been estimated to 3.4 nm, indicating an average GS thickness of ten layers. (c) GS diameter histogram obtained from several SEM images. The dashed line in (c) represents a log-normal fit, giving an average GS diameter of 120 nm.

Figure 3. (a) Sheet resistivity reduction factor after chemical doping with varied exposure time. (b) Stability of the doped LBA GS films, comparing encapsulated samples with the ones that were exposed to ambient air. (c) The sheet resistivity (R_S) as a function of the light absorption at 650 nm wavelength. The data for up to three stacked LBA GS layers is shown, both prior (circles) and after (diamonds) the chemical doping, with solid and dashed lines as smooth fits for the undoped and doped samples, respectively. Shaded areas indicate a sample-to-sample variations in both R_S and the light absorption. Inset of (c) shows sheet conductivity as a function of the number of stacked LBA GS layers.

one with the doped LBA GS surface exposed to the ambient conditions, and the other encapsulated (covered with Scotch tape) immediately after chemical doping. Figure 3(b) shows the relative change of sheet resistivity in time as $R(t)/R_0$, where R_0 stands for the initial sheet resistivity. Encapsulated samples show excellent time stability, with less than 5% change in sheet resistivity over two weeks.

3.4 Stacking of multiple LBA GS layers
The excellent adhesion of LBA GS sheets to the PET substrate allows not only for straightforward methods of chemical doping using liquids, but also for reproducible stacking of additional LBA layers. This is a very promising technique for making solution-based GRM

heterointerfaces [36], using a simple, one-step, low-cost and high-yield self-assembly process.

Figure 3(c) shows the sheet resistivity (R_S) as a function of optical transmittance of stacked LBA GS layers. After stacking, samples were exposed to nitric acid for 5 min. The lowest sheet resistivity obtained were on the order of 800 $\Omega/\square$, albeit at only 50% transmittance. The fact that subsequent doping can affect the entire film could be attributed to intercalation of nitric acid into the LBA GS stacks [28].

The sheet conductivity ($\sigma_S = 1/R_S$) of both doped and undoped samples was found to linearly depend on the number of LBA layers, as shown in the inset of figure 3(c). This indicates that appended LBA layers act as additional transport channels, and that the current is homogenously distributed across the entire film
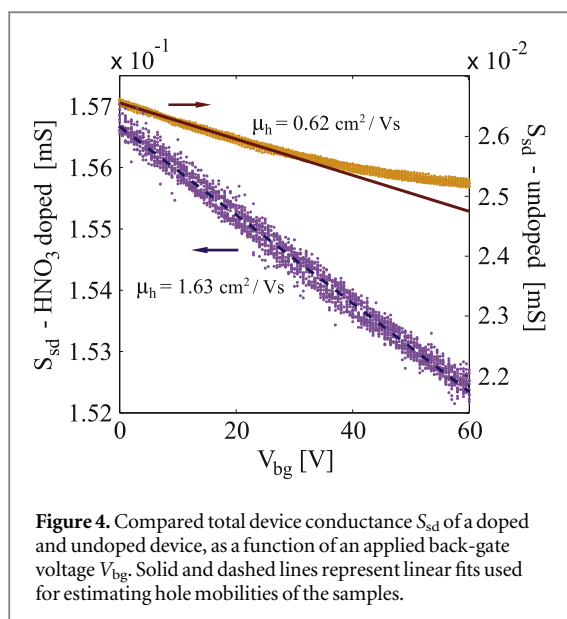
Figure 4. Compared total device conductance S_{sd} of a doped and undoped device, as a function of an applied back-gate voltage V_{bg}. Solid and dashed lines represent linear fits used for estimating hole mobilities of the samples.

when the distance between the electrodes is in the millimeter range [28].

3.5 Sheet resistivity and DC electrical characteristics measurements

The total resistance of each sample was measured in a two-point probe configuration, and the sheet resistivity was obtained by including the sample geometry factors. More details are given in supplementary information. The contact resistance was neglected being a three orders of magnitude smaller than the LBA GS film resistance. Sheet resistivity of as produced LBA GS films on PET was (70 ± 6) kΩ/$\square$ for films with average thickness of 10 graphene layers. The sheet resistivity of the films after the doping was found to be reduced by the factor of five to six, reaching the value of (12 ± 3) kΩ/$\square$. This change is two times larger than that reported for nitric acid doping of CVD graphene [17, 19, 28, 50]. Such a large reduction of sheet resistivity can be attributed to the fact that LPE based films have a large amount of un-functionalized GS edges, thus having more sites available for adsorption of NO_3^- and hydroxyl groups [53].

In order to characterize electrical properties of both undoped and chemically doped LBA GS films, measurements of direct-current (DC) electrical characteristics were carried out at room temperature. Device preparation, schematic representation of the measurement setups and measurements of the current between source (s) and drain (d) electrodes as a function of applied source–drain voltage V_{sd} are given in supplementary information.

Figure 4 shows the dependence of the total conductance (S_{ds}) as a function of back gate voltage (V_{bg}) for several consequent sweeps between 0 and 60 V. The negative slope of $S_{ds}(V_{bg})$ confirms that both undoped and chemically doped LBA GS films have holes as dominant charge carriers. Unintentional

p-doping of the sample prior to the exposure to nitric acid is attributed to the remaining water and NMP residue at the interface during film transfer [32]. Conductance function was approximated to be linear, neglecting the deviation of the undoped sample at higher voltages, which is likely due to approaching a charge neutrality point. Using the linear approximation, carrier mobility has been estimated [43, 60] to be 0.6–0.8 cm^2 V^{-1} s^{-1} for the undoped samples, and 1.55–1.75 cm^2 V^{-1} s^{-1} for the samples that were exposed to nitric acid.

3.6 X-ray photoelectron spectroscopy (XPS)

XPS was used to elucidate the mechanisms behind the doping of graphene with HNO$_3$. Measurements were carried out on a Thermo Scientific Theta Probe XPS system, providing the quantitative elemental analysis. The samples were not encapsulated, and the measurements were carried out at room temperature without *in situ* heating. In addition, angle resolved XPS was used to obtain qualitative information of elemental distribution along the depth of the samples. Experimental details are given in supplementary information. XPS indicated the presence of carbon, oxygen, and nitrogen in the sample (see supplementary information figure S2). Nitrogen 1s core level intensities of undoped LBA GS film on PET imply nitrogen concentrations of ~0.5 at%, which is an indication of intrinsic film doping by residual NMP [32].

Figures 5(a) and (b) show C 1s and O 1s core-level XPS spectra of the pristine and HNO$_3$-treated graphene films deposited on PET. In figure 5(a) the C 1s band is deconvoluted to reveal peaks corresponding to binding energies of graphene (sp^2)/C–C bonds (284.4 eV), as well as the C–O (288,6 eV) and C=O bonds (289.1 eV). The origin of a small C=O peak in the pristine graphene/PET sample may be from photoelectrons ejected from the PET substrate or from the water molecules trapped between the flakes in the film.

In figure 5(b), the O 1s band peak has been deconvoluted to reveal the C–O (533.6 eV) and C=O (532 eV) bonds. In both C 1s and O 1s bands the chemical modification by HNO$_3$ is evident through the change in the intensity of C=O peaks. This change is small (oxygen content is reduced from 7.3 to 5.9 at%) and can not solely account for the change in conductivity of graphene films after the treatment with nitric acid. The relative depth plot (see supplementary information figure S3) reveals the change in the elemental distribution across the graphene layer. In pristine graphene films, oxygen atoms are mostly placed closer to the surface layer, while in the acid-treated films the situation is reversed. This can be an indication of the rearrangement in the LBA graphene films on the substrate, with oxygen bonds established between the edges of the graphene flakes deeper in the film. This result is in accordance with the reduction of

Figure 5. (a) and (b) detailed photoelectron spectra for C 1s and O 1s bands, respectively. Here, solid and dashed lines represent a LBA GS film on PET before and after chemical doping.
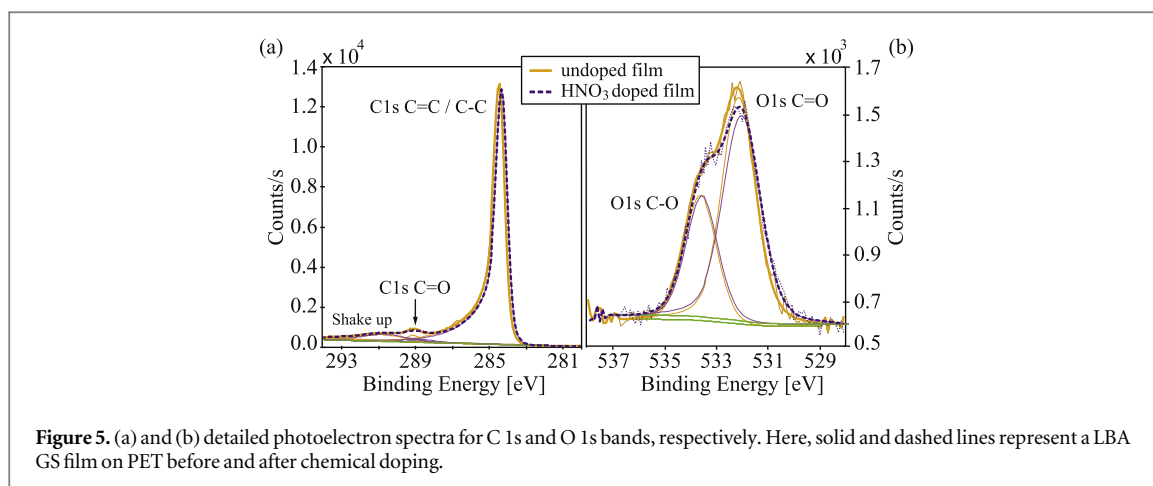
the relative intensity of the D- and G-modes in our Raman spectra, corresponding to the GS edges.

The amount of nitrogen in acid-treated films increased from 0.5 to 1 at%. The nature of the measurements could potentially diminish in a small fraction the amount of nitrogen present in the sample. However, the samples were not heated and the nitrogen is incorporated within the film, therefore the change in at% of nitrogen that could arise from these measurements is neglected. In the high-resolution spectrum of N 1s band (see supplementary information figure S3), there is no evidence of the shift in binding energy corresponding to N–O or N–C chemical bonding. Its binding energy (399.8 eV) corresponds to previously reported conjugated nitrogen which does not belong to the graphene molecule [61].

XPS analysis indicates that nitrogen is not incorporated in the honeycomb lattice structure as this would result in n-doping of graphene [51]. The $C=O^{-}$, $C(O)OH^{-}$, and NO_3^{-} bonds are changing the carbon atoms hybridization and possibly allowing for the creation of edge-plane like catalytic sites in graphene [52, 62]. Which one of these chemical moieties is the most important factor contributing to the improved conductivity of HNO_3-treated graphene is not clear.

3.7 Transmittance measurements
The effect of chemical doping on optical properties of LBA GS films was investigated with measurements of optical transmittance, using a spectroscopic ellipsometer in photometric mode (SOPRA GES5E IRSE). Figure 6(a) shows the transmittance of a LBA GS film in the visible and UV ranges on quartz. In the UV, the transmittance of graphene is dominated by an exciton-shifted van Hove peak in absorption [63–65]. For this reason the measured data was fitted with a Fano resonant function [65, 66]. Average transmittance of a single LBA GS film at a wavelength of 650 nm was (78 ± 4)%. Considering that each layer of graphene absorbs 2.3% of incident light in the visible part of the spectrum [67] and has a thickness of 0.335 nm, the

average film thickness indicated by transmittance measurements is (3.2 ± 0.6) nm, in agreement with AFM measurements.

The transmittance of the doped film at the same wavelength is 74%, which is within the experimental error and the variation between individual samples (figure 6(a), shaded area). While the transmittance decreased only slightly with chemical doping, the sheet resistivity of this sample decreased by a factor of ~ 4.5.

3.8 Raman spectroscopy
Raman spectra of LBA GS films prior to and after nitric acid doping were also investigated. Room temperature measurements of Raman spectra were obtained using a TriVista 557 S&I GmbH Raman spectrometer ($\lambda = 532$ nm). Figure 6(b) shows Raman spectra of a LBA GS film on a glass substrate prior to (solid line) and after (dashed line) chemical doping, compared with graphite powder (dotted-line) before the LPE process. Analogous results were obtained for films on a PET substrate (see supplementary information), however in this case Raman spectra is dominated by PET modes. No significant shifts of any characteristic Raman modes of graphene (graphite) were detected after chemical doping. The only notable change of the Raman spectra due to chemical doping was the reduction of a $I(D)/I(G)$ relative intensity by 25% (see figure 6(b) inset). The relative intensity $I(D)/I(G)$ is indicative of the amount of GS edge scattering [68], hence our results point to a weakening of edge effects in doped films.

3.9 Work function measurements
The work function of a surface holds important information about the electronic structure. Using Kelvin probe force microscopy (KPFM, NTEGRA Spectra), we measured the work function of LBA GS films prior to and after chemical treatment, using the tabulated value of the work function for highly ordered pyrolytic graphite (HOPG) [69, 70] as a reference for
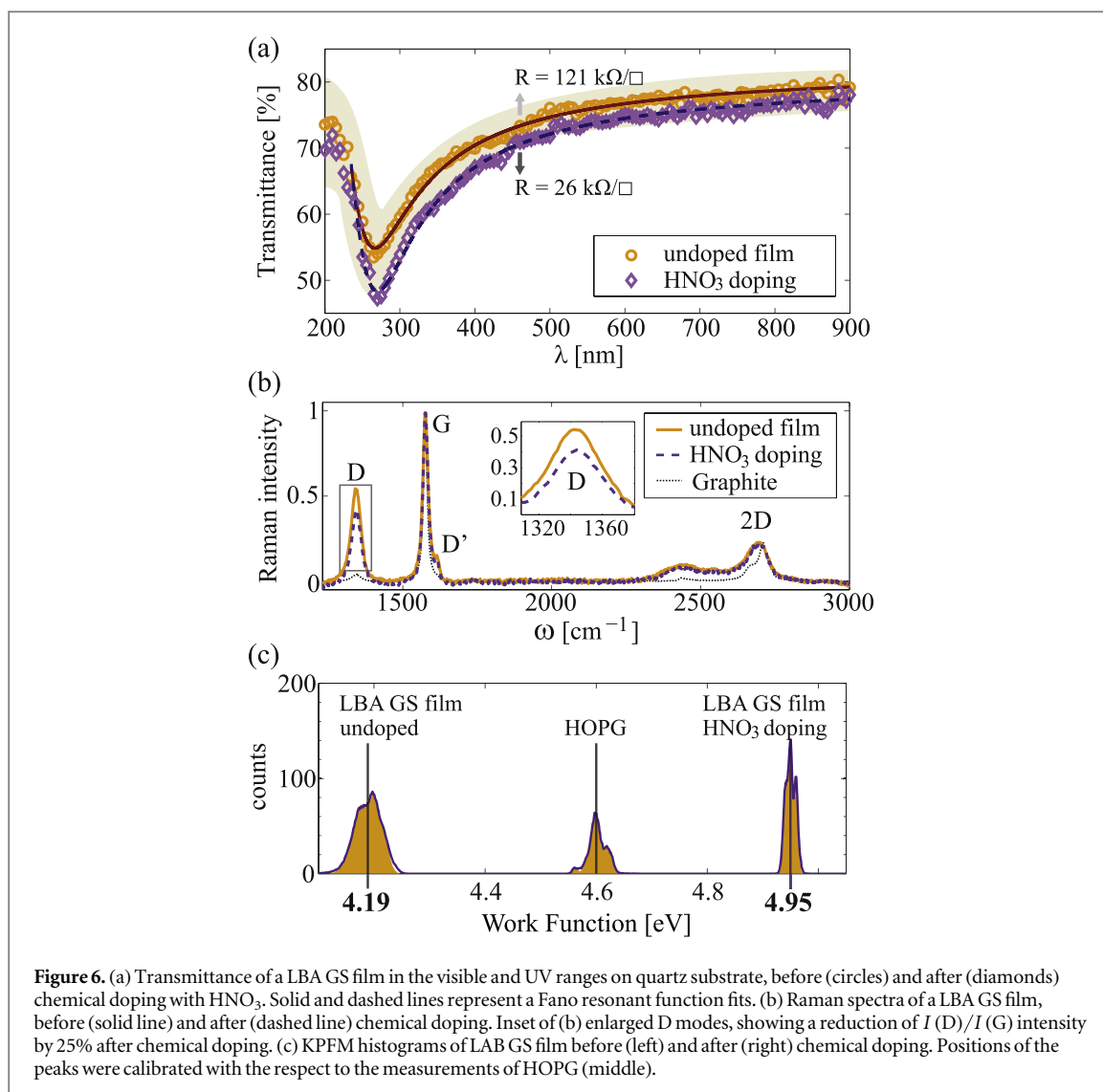
Figure 6. (a) Transmittance of a LBA GS film in the visible and UV ranges on quartz substrate, before (circles) and after (diamonds) chemical doping with HNO_3. Solid and dashed lines represent a Fano resonant function fits. (b) Raman spectra of a LBA GS film, before (solid line) and after (dashed line) chemical doping. Inset of (b) enlarged D modes, showing a reduction of $I(D)/I(G)$ intensity by 25% after chemical doping. (c) KPFM histograms of LAB GS film before (left) and after (right) chemical doping. Positions of the peaks were calibrated with the respect to the measurements of HOPG (middle).

calibrating the AFM tip (details in supplementary information).

As a result, the work function values of (4.19 ± 0.05) eV and (4.95 ± 0.05) eV were obtained for the LBA GS films prior and after chemical doping, respectively. The results are presented in figure 6(c). Undoped films have much lower work function than HOPG, which is expected due to the presence of a large number of GS edges. Furthermore, this confirms that GSs are not functionalized, since in the case of reduced GO or surfactant assisted LPE much higher work functions of the resulting films are obtained [71].

Chemical doping with nitric acid increases the work function by as much as 0.75 eV, a 50% larger increase than in the case of a similar treatment of CVD graphene [17, 50]. An increase of the work function confirms that electrons migrate from GSs [72], resulting in further p-doping and a decrease of the Fermi level with the respect to Dirac point. Adsorption of NO_3^- groups at the sheet edges is also expected to strongly contribute to the increase of the work function.

3.10 Dependence of the sheet resistivity upon axial strain

In addition to chemical doping, the change of the sheet resistivity of LBA GS films on PET substrates was investigated under various bending conditions. The curvature of the substrate was controlled by a micrometer screw in steps of 150 μm, as schematically presented in figure 7(a). The amount of bending is expressed as an axial strain (ϵ) that LBA GS films suffer at the surface of a PET substrate upon bending. Bending radii down to 6 mm were used, giving values of axial strain up to 1.6%. Stretched LBA GS films have shown an increase in the sheet resistivity, significantly larger than in the CVD graphene [9]. Upon axial strain of about 1.5% LBA GS films on PET substrate show an increase of sheet resistivity by as much as 50%. Furthermore, Raman spectra of strained films (given in supplementary information figure S5) did not show any detectable shifts of graphene modes. This indicates that individual GSs are not exhibiting a significant amount of strain. The change in sheet resistivity is attributed to increased separation between individual
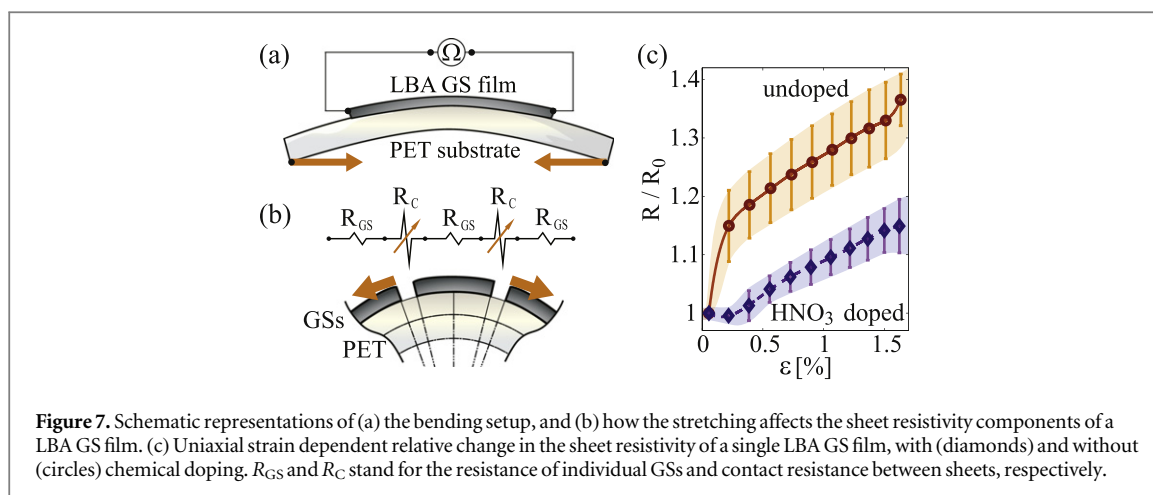
Figure 7. Schematic representations of (a) the bending setup, and (b) how the stretching affects the sheet resistivity components of a LBA GS film. (c) Uniaxial strain dependent relative change in the sheet resistivity of a single LBA GS film, with (diamonds) and without (circles) chemical doping. R_{GS} and R_C stand for the resistance of individual GSs and contact resistance between sheets, respectively.

GSs, which increases the contact resistance between them, as schematically presented in figure 7(b). The relative change in sheet resistivity upon bending reaches 20% larger values in undoped films, as presented in figure 7(c). A large change of resistance upon axial strain opens up a possibility to use LBA GS films in sensing applications as strain gauges, pressure sensors, touch screens or e-skin [73].

Chemically doped samples show a significantly different change in sheet resistivity under small axial strain. For bending radii greater than 30 mm (axial strain less than 0.3%) chemically doped samples show a negligible change in the sheet resistivity. On the other hand, undoped samples show more than 10% change for the same bending conditions. Axial strain of 0.3% would correspond to the separation between individual sheets of 0.36 nm when an averaged sheet diameter of 120 nm is considered. Interestingly, this is well matched with a thermochemical radii of NO_3^- anions. This indicates that NO_3^- groups attached at the edges of GSs provide a contact between the sheets until a high enough axial strain is reached. Afterwards, the sheet resistivity of the doped samples follow a similar trend as the undoped ones. This opens up a possibility to use chemically doped LBA GS films for flexible TCEs, in the cases when small bending radii are not required.

4 Conclusion

In summary, we have shown how the LBA of multi-layer GSs produced from the dispersion in NMP and transferred on PET can be used to fabricate transparent and conductive films. An excellent adhesion of these films on PET enables for a straightforward chemical doping and stacking of multiple layers. In particular, p-type chemical doping with nitric acid has been used to reduce sheet resistivity and increase work function of these films, thus making them a more suitable low-cost alternative to CVD graphene for various TCE applications.

The sheet resistivity of deposited LBA GS layers on PET was found to be (70 ± 6) kΩ/□ with the transmittance of 78% at 650 nm wavelength. Upon a short exposure to nitric acid, sheet resistivity was reduced 5–6 fold, reaching the value of (12 ± 3) kΩ/□ with a minor reduction of the visible light transmittance. An increase of the LBA GS film work function by 0.75 eV was found upon chemical doping, yielding a value of 4.95 eV for the doped films. The work function measurements and the dependance of the sheet resistivity upon axial strain both indicate that a large reduction of the sheet resistivity occurs due to adsorption of NO_3^- groups at the edges of GSs. This reduces a contact resistance between the sheets, in addition to an increase of carrier concentration within the sheets.

References

[1] Novoselov K S, Falko V I, Colombo L, Gellert P R, Schwab M G and Kim K 2012 *Nature* **490** 192–200
[2] Ferrari A C *et al* 2014 *Nanoscale* **7** 4598–810
[3] Bonaccorso F, Colombo L, Yu G, Stoller M, Tozzini V, Ferrari A C, Ruoff R S and Pellegrini V 2015 *Science* **347** 1246501
[4] Segal M 2009 *Nat. Nanotechnol.* **4** 612–4
[5] Park S and Ruoff R S 2009 *Nat. Nanotechnol.* **4** 217–24
[6] Britnell L *et al* 2013 *Science* **340** 1311–4
[7] Bonaccorso F, Lombardo A, Hasan T, Sun Z, Colombo L and Ferrari A C 2012 *Mater. Today* **15** 564–89
[8] De S and Coleman J N 2010 *ACS Nano* **4** 2713–20
[9] Kim K S, Zhao Y, Jang H, Lee S Y, Kim J M, Kim K S, Ahn J-H, Kim P, Choi J-Y and Hong B H 2009 *Nature* **457** 706–10
[10] Blake P *et al* 2008 *Nano Lett.* **8** 1704–08
[11] Wang X, Zhi L and Mullen K 2008 *Nano Lett.* **8** 323–7
[12] Wang H-X, Wang Q, Zhou K-G and Zhang H-L 2013 *Small* **9** 1266–83

[13] Pang S, Hernandez Y, Feng X and Mullen K 2011 *Adv. Mater.* **23** 2779–95

[14] Kratzer M, Bayer B C, Kidambi P R, Matković A, Gajić R, Cabrero-Vilatela A, Weatherup R S, Hofmann S and Teichert C 2015 *Appl. Phys. Lett.* **106** 103101

[15] Chhikara M, Pavlica E, Matković A, Beltaos A, Gajić R and Bratina G 2014 *Carbon* **69** 162–8

[16] Miao X, Tongay S, Petterson M K, Berke K, Rinzler A G, Appleton B R and Hebard A F 2012 *Nano Lett.* **12** 2745–50

[17] Wu Y, Zhang X, Jie J, Xie C, Zhang X, Sun B, Wang Y and Gao P 2013 *J. Phys. Chem.* C **117** 11968–76

[18] Park H, Chang S, Zhou X, Kong J, Palacios T and Gradecak S 2014 *Nano Lett.* **14** 5148–54

[19] Bae S *et al* 2010 *Nat. Nanotechnol.* **5** 574–8

[20] Wu J, Agrawal M, Becerril H A, Bao Z, Liu Z, Chen Y and Peumans P 2010 *ACS Nano* **4** 43–8

[21] Han T-H, Lee Y, Choi M-R, Woo S-H, Bae S-H, Hong B H, Ahn J-H and Lee T-W 2012 *Nat. Photon.* **6** 105–10

[22] Coraux J, N'Diaye A T, Busse C and Michely T 2008 *Nano Lett.* **8** 565–70

[23] Reina A, Jia X, Ho J, Nezich D, Son H, Bulovic V, Dresselhaus M S and Kong J 2008 *Nano Lett.* **9** 30–5

[24] Li X *et al* 2009 *Science* **324** 1312–4

[25] Hao Y *et al* 2013 *Science* **342** 720–3

[26] Zaretski A V and Lipomi D J 2015 *Nanoscale* **7** 9963–9

[27] Li X, Zhu Y, Cai W, Borysiak M, Han B, Chen D, Piner R D, Colombo L and Ruoff R S 2009 *Nano Lett.* **9** 4359–63

[28] Kasry A, Kuroda M A, Martyna G J, Tulevski G S and Bol A A 2010 *ACS Nano* **4** 3839–44

[29] Stankovich S, Dikin D A, Dommett G H, Kohlhaas K M, Zimney E J, Stach E A, Piner R D, Nguyen S T and Ruoff R S 2006 *Nature* **442** 282–6

[30] Stankovich S, Dikin D A, Piner R D, Kohlhaas K A, Kleinhammes A, Jia Y, Wu Y, Nguyen S T and Ruoff R S 2007 *Carbon* **45** 1558–65

[31] Eda G, Fanchini G and Chhowalla M 2008 *Nat. Nanotechnol.* **3** 270–4

[32] Hernandez Y *et al* 2008 *Nat. Nanotechnol.* **3** 563–8

[33] Cai M, Thorpe D, Adamson D H and Schniepp H C 2012 *J. Mater. Chem.* **22** 24992–5002

[34] Coleman J N *et al* 2011 *Science* **331** 568–71

[35] Eda G, Yamaguchi H, Voiry D, Fujita T, Chen M and Chhowalla M 2011 *Nano Lett.* **11** 5111–6

[36] Withers F *et al* 2014 *Nano Lett.* **14** 3987–92

[37] Torrisi F *et al* 2012 *ACS Nano* **6** 2992–3006

[38] Secor E B, Prabhumirashi P L, Puntambekar K, Geier M L and Hersam M C 2013 *J. Phys. Chem. Lett.* **4** 1347–51

[39] Del S K, Bornemann R, Bablich A, Schäfer-Eberwein H, Li J, Kowald T, Östling M, Bolívar P H and Lemme M C 2015 *2D Mater.* **2** 011003

[40] Dikin D A, Stankovich S, Zimney E J, Piner R D, Dommett G H, Evmenenko G, Nguyen S T and Ruoff R S 2007 *Nature* **448** 457–60

[41] Li X, Zhang G, Bai X, Sun X, Wang X, Wang E and Dai H 2008 *Nat. Nanotechnol.* **3** 538–42

[42] Zhu Y, Cai W, Piner R D, Velamakanni A and Ruoff R S 2009 *Appl. Phys. Lett.* **95** 103104

[43] Kim H, Mattevi C, Kim H J, Mittal A, Mkhoyan K A, Riman R E and Chhowalla M 2013 *Nanoscale* **5** 12365–74

[44] Yang T, Yang J, Shi L, Mäder E and Zheng Q 2015 *RSC Adv.* **5** 23650–7

[45] Biswas S and Drzal L T 2008 *Nano Lett.* **9** 167–72

[46] Woltornist S J, Oyer A J, Carrillo J-M Y, Dobrynin A V and Adamson D H 2013 *ACS Nano* **7** 7062–6

[47] Salvatierra R V, Domingues S H, Oliveira M M and Zarbin A J 2013 *Carbon* **57** 410–5

[48] Geim A and Grigorieva I 2013 *Nature* **499** 419–25

[49] Yang H, Withers F, Gebremedhn E, Lewis E, Britnell L, Felten A, Palermo V, Haigh S, Beljonne D and Casiraghi C 2014 *2D Mater.* **1** 011012

[50] Lee S, Yeo J-S, Ji Y, Cho C, Kim D-Y, Na S-I, Lee B H and Lee T 2012 *Nanotechnology* **23** 344013

[51] Wei D, Liu Y, Wang Y, Zhang H, Huang L and Yu G 2009 *Nano Lett.* **9** 1752–8

[52] Das S, Sudhagar P, Ito E, Lee D-y, Nagarajan S, Lee S Y, Kang Y S and Choi W 2012 *J. Mater. Chem.* **22** 20490–7

[53] Zheng Q, Ip W H, Lin X, Yousefi N, Yeung K K, Li Z and Kim J-K 2011 *ACS Nano* **5** 6039–51

[54] Dresselhaus M S and Dresselhaus G 2002 *Adv. Phys.* **51** 1–86

[55] Fillaux F, Menu S, Conard J, Fuzellier H, Parker S, Hanon A and Tomkinson J 1999 *Chem. Phys.* **242** 273–81

[56] Lancellotti L, Bobeico E, Capasso A, Della Noce M, Dikonimos T, Lisi N and Delli Veneri P 2014 *2014 Fotonica AEIT Italian Conf. on Photonics Technologies* pp 1–3

[57] Larsen L J, Shearer C J, Ellis A V and Shapter J G 2015 *RSC Adv.* **5** 38851–8

[58] Wang J, Zhou M, Tan G, Chen S, Wu F, Lu J and Amine K 2015 *Nanoscale* **7** 8023–34

[59] Xie X, Su D, Zhang J, Chen S, Mondal A K and Wang G 2015 *Nanoscale* **7** 3164–72

[60] Liang X, Fu Z and Chou S Y 2007 *Nano Lett.* **7** 3840–4

[61] Wu Y, Fang S and Jiang Y 1999 *Solid State Ion.* **120** 117–23

[62] Kudin K N, Ozbas B, Schniepp H C, Prud'Homme R K, Aksay I A and Car R 2008 *Nano Lett.* **8** 36–41

[63] Kravets V G, Grigorenko A N, Nair R R, Blake P, Anissimova S, Novoselov K S and Geim A K 2010 *Phys. Rev.* B **81** 155413

[64] Mak K F, Shan J and Heinz T F 2011 *Phys. Rev. Lett.* **106** 046401

[65] Chae D-H, Utikal T, Weisenburger S, Giessen H, Klitzing K v, Lippitz M and Smet J 2011 *Nano Lett.* **11** 1379–82

[66] Matković A, Beltaos A, Milićević M, Ralević U, Vasić B, Jovanović D and Gajić R 2012 *J. Appl. Phys.* **112** 123523

[67] Nair R R, Blake P, Grigorenko A N, Novoselov K S, Booth T J, Stauber T, Peres N M R and Geim A K 2008 *Science* **320** 1308

[68] Khan U, O'Neill A, Lotya M, De S and Coleman J N 2010 *Small* **6** 864–71

[69] Yu Y-J, Zhao Y, Ryu S, Brus L E, Kim K S and Kim P 2009 *Nano Lett.* **9** 3430–4

[70] Takahashi T, Tokailin H and Sagawa T 1985 *Phys. Rev.* B **32** 8317

[71] Bausi F, Schlierf A, Treossi E, Schwab M G, Palermo V and Cacialli F 2015 *Org. Electron.* **18** 53–60

[72] Giovannetti G, Khomyakov P A, Brocks G, Karpan V M, van den Brink J and Kelly P J 2008 *Phys. Rev. Lett.* **101** 026803

[73] Zang Y, Zhang F, Di C-a and Zhu D 2015 *Mater. Horiz.* **2** 140–56

Supplementary information

Aleksandar Matković[1]**, Ivana Milošević**[1]**, Marijana Milićević**[1]**, Tijana Tomašević-Ilić**[1]**, Jelena Pešić**[1]**, Milenko Musić**[1]**, Marko Spasenović**[1]**, Djordje Jovanović**[1]**, Borislav Vasić**[1]**, Christopher Deeks**[2]**, Radmila Panajotović**[1]**, Milivoj R. Belić**[3]**, and Radoš Gajić**[1]

[1] Center for Solid State Physics and New Materials, Institute of Physics, University of Belgrade, Pregrevica 118, 11080 Belgrade, Serbia

[2] Thermo Fisher Scientific, Unit 24, The Birches Industrial Estate, East Grinstead, RH19 1UB, UK.

[3] Texas A&M University at Qatar, P.O. Box 23874 Doha, Qatar

E-mail: `amatkovic@ipb.ac.rs`

1. Direct Current Electrical Characteristics

Direct current (DC) electrical characteristic measurements were used to confirm the type of majority carriers and to estimate carrier mobility. The results are shown in Fig. 3 of the main text. Here are presented the details regarding device fabrication, measurements setup and confirmation of Ohmic contacts with gold electrodes.

In order to measure DC electrical characteristics, LBA GS films were deposited on a highly doped (0.001-0.01 Ω/cm) silicon wafer with a 300 nm thick SiO_2 layer. The substrates had pre defined gold electrodes with $\sim$150 μm channel length and $\sim$700 μm channel width, made by a shadow mask. LBA GS films were deposited in the same manner as described in the main text. It is worth mentioning that due to much lower adhesion between LBA GS film and SiO_2 surface compared with PET substrates, majority of the films are either washed out by the acid, or exhibited holes and cracks on the surface. Only films that had no visible damage (inspected under optical microscope) after chemical doping have been used in DC electrical characterization.

Figure S1(a) shows a schematic representation of the setup used for the measurements of total source-drain conductance (S_{sd}) as a function of back gate voltage (V_{bg}). $S_{sd}(V_{bg})$ measurements are given in Fig. 3 in the main text. A schematic representation of the setup used for the measurements of $I_{sd}(V_{sd})$ is shown in figure S1(b), and the I-V function for the undoped film is shown in figure S1(c). The linear dependence of $I_{sd}(V_{sd})$ confirms that contacts between the LBA GS layer and underlying gold electrodes are Ohmic.

Figure S1(d) shows a top view schematic representation of the sample geometry used for two-point probe resistivity measurements. Gold pads were defined by a shadow

(a)

(b)

(c)

(d)
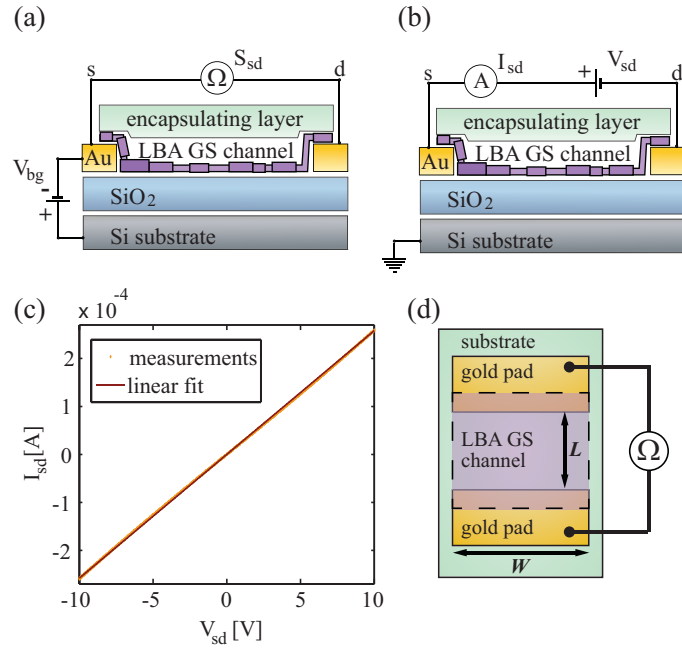
Figure S1. (a) and (b) schematic representations of the setups used for measuring $S_{sd}(V_{bg})$ and $I_{sd}(V_{sd})$, respectively. (c) The dependance of $I_{sd}(V_{sd})$ for an undoped LBA GS layer. (d) A top view schematic representation of the sample geometry used for two-point probe resistivity measurements. L and W stand for LBA GS channel length and width, respectively.

mask. The sheet resistivity was obtained by including the sample geometry factors L and W as: $\rho = R \cdot W/L$.

2. X-ray photoelectron spectroscopy

X-ray photoelectron spectroscopy (XPS) has been used to obtain elemental and chemical information of LBA GS films deposited on PET. High resolution scans of carbon 1s and oxygen 1s peaks are shown in Fig. 4 of the main text. Here, survey scans, high resolution scans of nitrogen 1s peak, relative depth plots, and the details regarding the estimate of residual NMP wt% in LBA GS films are given.

Figure S2(a,b) shows a survey scans of undoped and HNO_3-treated LBA GS films on PET, respectively. Survey scans were obtained with a spot size of 400 μm, thus averaging over a large amount of GSs. Using 1s core level intensities, atomic% of each detected element is calculated. The results are shown in a tabular insets of figure S2. Using angle resolved XPS (ARXPS) silicon was detected as a surface contamination. Considering that the LBA GS layer is 3-4 nm thick, the XPS spectra will have contributions both from the graphene layer and from the underlaying PET substrate.

Figure S3(a,b) shows high resolution scans of nitrogen 1s peaks for undoped and HNO_3-treated LBA GS films on PET. These spectra indicate that nitrogen is mostly present in a conjugated C=N bond at the edges of GSs [1].

(a)

Name	Atomic %
C 1s	91.79
O 1s	7.3
N 1s	0.47
Si 2p	0.44

(b)

Name	Atomic %
C 1s	92.86
O 1s	5.87
N 1s	1.01
Si 2p	0.27
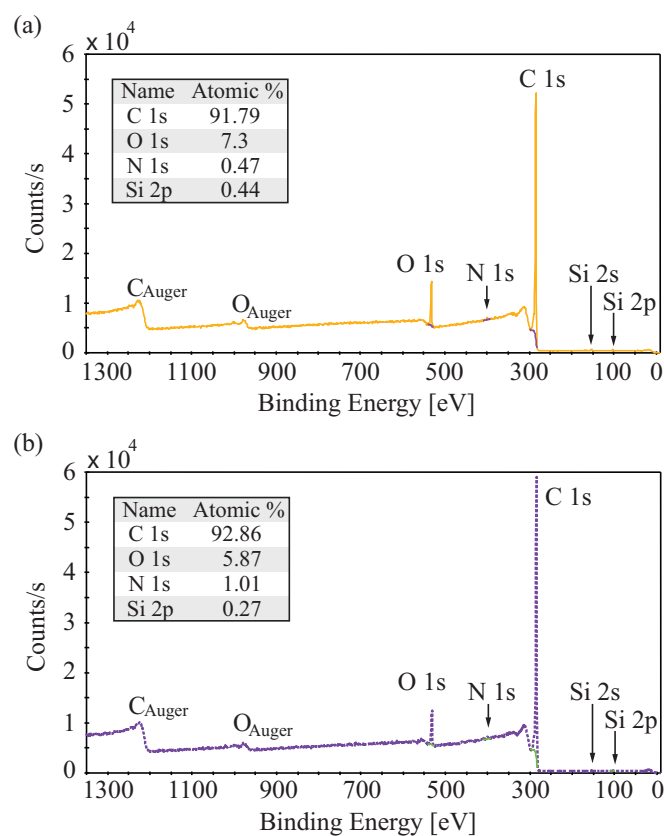
Figure S2. (a) and (b) survey scans of a LBA GS film on PET substrate prior and after chemical doping, respectively. Inset tables show atomic% of all elements detected in the scans.

(a)

(b)

(c)
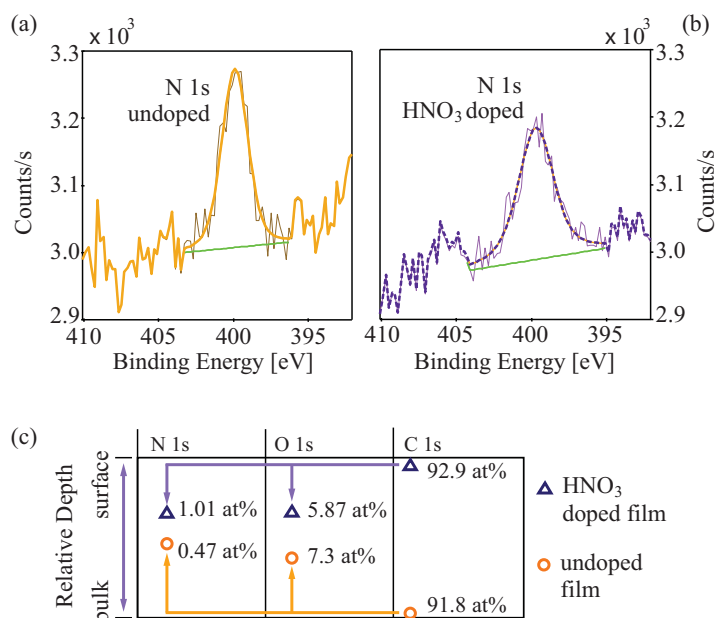
Figure S3. (a) and (b) high resolution scans of nitrogen 1s peak for undoped and HNO_3-treated LBA GS films on PET. (c) Relative depth plot obtained using ARXPS for undoped (circles) and chemically doped (triangles) LBA GS films on PET. Each point also indicates atomic% (at%) for that particular element in the sample.

ARXPS has been employed to obtain qualitative information on the depth ordering of the elements in LBA GS films prior and after chemical doping. ARXPS measurements were carried out under 16 separate angles between 20° and 80° by measuring high resolution spectra for each element with a 400 μm spot. As a result relative depth plots are obtained. A comparison between relative depth plots of undoped (circles) and HNO$_3$-treated (triangles) LBA GS films on PET is shown in figure S3(c). Each point in figure S3(c) represents an average depth of that particular species in the sample. Position of a C1s peak is associated with the position of a LBA GS layer. Relative positions of N1s and O1s peaks can then indicate where is the majority of nitrogen and oxygen atoms located in comparison with LBA GS layer. Interestingly, ARXPS suggests that prior to chemical doping both nitrogen and oxygen atoms are on average mostly located on the top of LBA GS layer, and after the doping both species are located under LBA GS layer. This implies a rearrangement of the LBA GS film upon exposure to nitric acid, as described in the main text.

3. KPFM Maps and Data Analysis

Kelvin probe force microscopy (KPFM) has been used to measure the work functions of LBA GS films prior and after chemical doping with nitric acid. The results are given in Fig. 5(c) of the main text. Here the details regarding the measurements, map analysis and the method used for obtaining the work functions are presented.

KPFM measurements were done using the two-pass technique [2, 3]. In the first pass, a topographic line was measured in the tapping mode. Figure S4(a) shows a typical 5×5 μm^2 LBA GS film topography measured with 256×256 points. In the second pass, the tip was lifted by 30 nm and moved across the surface following the topographic profile, obtained from the first scan. During the second pass, a combination of an AC and DC voltage was applied between the tip and the sample. The frequency of the AC voltage was matched to the resonant frequency of the cantilever. The DC component was then adjusted to cancel an electrostatic force between the tip and the sample, resulting with a zero amplitude of the cantilever oscillations (near its resonant frequency). This procedure was repeated for every point of a selected area of the sample. Resulting KPFM maps show the applied DC component, *i.e.* the contact potential difference (CPD) between the sample and the tip. Figure S4(b) shows corresponding KPFM map to the sample topography (figure S4(a)). In order to determine CPD of the measured surface histograms of KPFM maps were used and fitted by Gaussian lines, as shown in figure S4(c).

CPD shows the difference in the work functions of the tip and the sample. In order to obtain the work function of the measured surface, the work function of the tip must be known. This was obtained by measuring several KPFM maps of freshly cleaved highly oriented pyrolytic graphite (HOPG). Work function of HOPG was considered to be 4.6 eV [2, 4].

Afterwards, several KPFM maps of LBA GS films were measured prior and after

(a)

(b)

| 75.1 nm |
| 40.0 |
| 20.0 |
| 8.6 |

| -0.07 V |
| -0.10 |
| -0.12 |
| -0.13 |

(c)

(d)
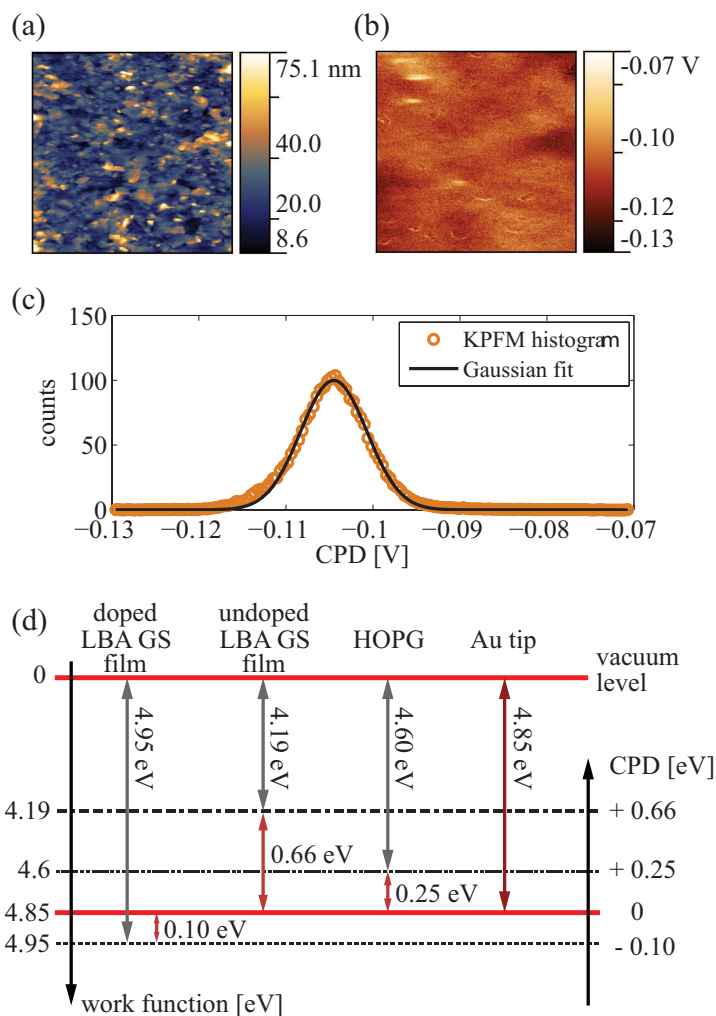
Figure S4. (a) 5×5 μm^2 topography image of a doped LBA GS film on PET. (b) Corresponding KPFM map of (a). (c) Histogram of (b) (circles) and Gaussian fit (solid line). (d) Schematic representation of the relation between measured CPDs and their corresponding work functions.

chemical doping. All of the obtained CPD histograms for each surface were added up, and an average CPD value was obtained from Gaussian fits as an average of the peak positions weighted by the hight of the peaks. The work functions were related to their corresponding CPD measurements as illustrated by a diagram in figure S4(d).

4. Raman measurements of LBA GS films on PET

Raman spectra of LBA GS films on PET substrate prior (solid line) and after (dashed line) chemical doping are shown in figure S5(a), and are compared with a clean PET substrate (dotted line). Most of the observed Raman modes belong to PET. The only two detected modes of the LBA GS film in the measured spectral range are D ($\sim$1350cm^{-1}) and G ($\sim$1580cm^{-1}) modes of graphene (graphite), also shown in figure S5(b) and (c), respectively. Due to the low intensity from LBA GS layer, compared
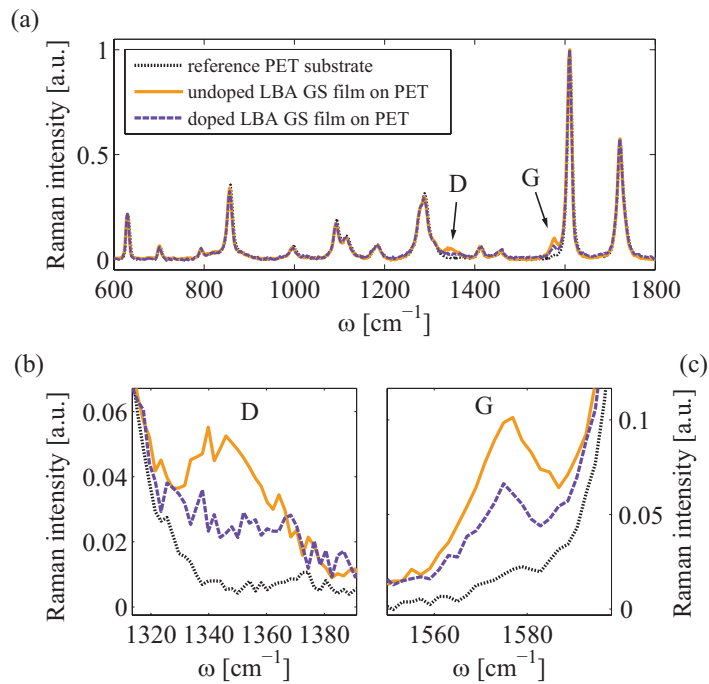
Figure S5. (a) Raman spectra of a single LBA GS film on a PET substrate, before (solid line) and after (dashed line) chemical doping, compared with a clean PET substrate (dotted line). (b) and (c) enlarged regions of graphene D and G modes, respectively.

to Raman intensity from PET substrate, graphite's 2D mode was barely resolved on PET. Relative intensity $I(D)/I(G)$ of both undoped and HNO_3-treated LBA GS films on PET are in agreement with the data obtained for the samples on glass substrates (figure 4(b) in the main text).

Additionally, no notable changes in any Raman modes of PET were detected after exposure of the sample to nitric acid. This indicates that nitric acid does not affect underlaying PET substrate.

Raman spectra of LBA GS films under various bending conditions have also been examined. Figure S6(a) shows Raman spectra of a single LBA GS film on PET substrate upon axial strain of 0 % (solid line), 1.5 % (dashed line) and 3 % (dot-dashed line). Figure S6(b) shows enlarged region of G mode. Resistance of the samples was monitored during the measurements of Raman spectra. Sheet resistivity increased by ∼50 % under axial strain of 1.5 %, and ∼100 % under axial strain of 3 %. However, as can be seen from Raman spectra in figure S6 individual sheet do not exhibit axial strain, since there is no detectable shifts or broadenings of the G mode [5, 6].

References

[1] Y. Wu, S. Fang and Y. Jiang, *Solid State Ionics*, 1999, **120**, 117–123
[2] Y.-J. Yu, Y. Zhao, S. Ryu, L. E. Brus, K. S. Kim and P. Kim, *Nano Letters*, 2009, **9**, 3430–3434

(a)

(b)
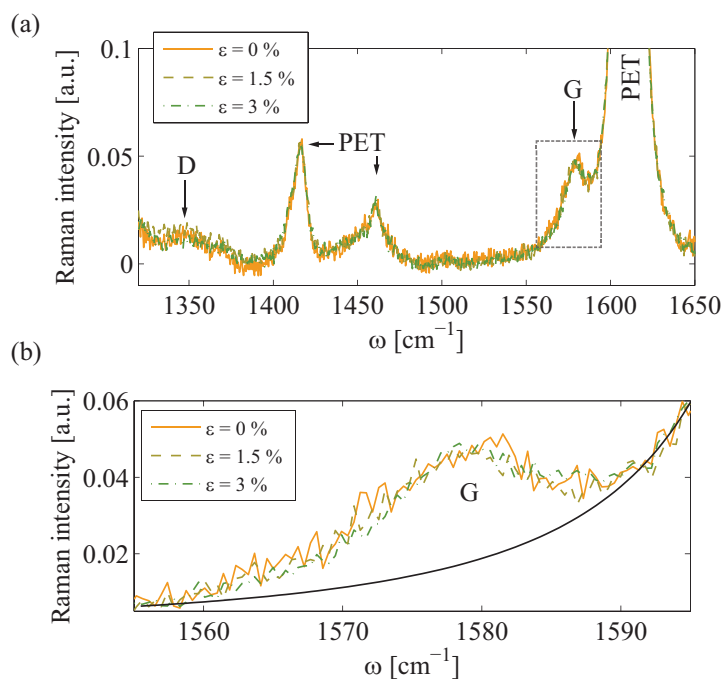
Figure S6. (a) Raman spectra of a single LBA GS film on a PET substrate upon axial strain of 0 % (solid line), 1.5 % (dashed line) and 3 % (dot-dashed line). (b) enlarged area of G mode.

[3] A. Matković, M. Chhikara, M. Milićević, U. Ralević, B. Vasić, D. Jovanović, M. R. Belić, G. Bratina and R. Gajić, *Journal of Applied Physics*, 2015, **117**, 015305

[4] T. Takahashi, H. Tokailin and T. Sagawa, *Physical Review B*, 1985, **32**, 8317

[5] T. Mohiuddin, A. Lombardo, R. Nair, A. Bonetti, G. Savini, R. Jalil, N. Bonini, D. Basko, C. Galiotis, N. Marzari *et al.*, *Physical Review B*, 2009, **79**, 205433

[6] F. Ding, H. Ji, Y. Chen, A. Herklotz, K. Dorr, Y. Mei, A. Rastelli and O. G. Schmidt, *Nano Letters*, 2010, **10**, 3453–3458

Silver film on nanocrystalline TiO₂ support: Photocatalytic and antimicrobial ability

Ivana D. Vukoje [a], Tijana D. Tomašević-Ilić [a], Aleksandra R. Zarubica [b], Suzana Dimitrijević [c], Milica D. Budimir [a], Mila R. Vranješ [a], Zoran V. Šaponjić [a], Jovan M. Nedeljković [a,*]

[a] Vinča Institute of Nuclear Sciences, University of Belgrade, P.O. Box 522, 11000 Belgrade, Serbia
[b] Department of Chemistry, Faculty of Science and Mathematics, University of Niš, Višegradska 33, 18000 Niš, Serbia
[c] Faculty of Technology and Metallurgy, University of Belgrade, Karnegijeva 4, 11000 Belgrade, Serbia

ABSTRACT

Nanocrystalline TiO₂ films were prepared on glass slides by the dip coating technique using colloidal solutions consisting of 4.5 nm particles as a precursor. Photoirradiation of nanocrystalline TiO₂ film modified with alanine that covalently binds to the surface of TiO₂ and at the same time chelate silver ions induced formation of metallic silver film. Optical and morphological properties of thin silver films on nanocrystalline TiO₂ support were studied by absorption spectroscopy and atomic force microscopy. Improvement of photocatalytic performance of nanocrystalline TiO₂ films after deposition of silver was observed in degradation reaction of crystal violet. Antimicrobial ability of deposited silver films on nanocrystalline TiO₂ support was tested in dark as a function of time against *Escherichia coli*, *Staphylococcus aureus*, and *Candida albicans*. The silver films ensured maximum cells reduction of both bacteria, while the fungi reduction reached satisfactory 98.45% after 24 h of contact.

© 2014 Published by Elsevier Ltd.

1. Introduction

Photocatalytic reactions on TiO₂ surfaces are very important in environmental cleanup and remediation, such as oxidation of organic materials [1,2] and reduction of heavy metal ions [3,4]. The large band gap of TiO₂ (3.2 eV), allowing only UV photons ($\lambda < 380$ nm) to produce electron–hole pairs and stimulate redox processes on the catalyst surface, limit the efficiency of solar light utilization [5]. In addition, the majority of photogenerated electron–hole pairs recombine, rendering them not available to initiate surface redox processes [6]. Different approaches have been applied in order to achieve efficient TiO₂ based photocatalytic process, including: (a) doping [7–9], to improve visible light absorption of the photocatalyst, (b) morphology and crystal phase optimization to enhance lifetimes of photoexcited states, and (c) deposition of metal nanoparticles to increase electron transfer rates [10,11].

The performance improvement of TiO₂ nanoparticles for reduction of heavy metal ions was achieved using multifunctional ligands which bind simultaneously the colloid surface and heavy metal ions [3]. The above mentioned studies were extended to photocatalytic depositions of metals by using solid state material. Efficient reduction of silver, copper and gold ions to corresponding metals by using dry nanocrystalline TiO₂ films surface modified with aliphatic amino acids was reported [12,13].

A rising problem with microbes resistant to antibiotics renewed the interest for silver and silver compounds which are historically recognized as powerful biocides for more than 650 various microbes. Despite the excellent antimicrobial activity, silver nitrate is unsuitable for the long term use. However, a desirable level of antimicrobial activity can be obtained with silver nanoparticles. The antimicrobial activity of colloidal silver nanoparticles is highly influenced by the dimensions of the particles – the smaller the particles, the higher the antimicrobial efficiency [14]. Recently developed simple routes for preparation of silver colloids with desired size gave burst to their application in the antimicrobial finishing of textile materials [15–22]. On the other hand, there are just a few studies concerning bacterial inactivation on nanostructured metallic films prepared by either high power impulse magnetron sputtering or direct current pulsed magnetron sputtering [23,24].

In this study, nanocrystalline TiO_2 films on glass slides were prepared by the dip coating technique using as a precursor colloid consisting of particles with average size of 4.5 nm. Photocatalytic reduction of silver ions led to the formation of metallic silver on nanocrystalline TiO_2 films. Photocatalytic and antimicrobial ability of synthesized nanostructures were main focus of this study. The influence of silver on photocatalytic efficiency of nanocrystalline TiO_2 films was tested in degradation reaction of the organic dye crystal violet. In addition, antibacterial and antifungal ability of deposited silver on nanocrystalline TiO_2 support against Gram-negative bacteria *Escherichia coli* and Gram-positive bacteria *Staphylococcus aureus*, as well as fungi *Candida albicans* was investigated.

2. Experimental

2.1. Synthesis and characterization of silver films on nanocrystalline TiO_2 supports

The TiO_2 colloids with mean particle diameter of 4.5 nm were prepared by controlled hydrolysis of titanium(IV) chloride, as described elsewhere [25]. The concentration of TiO_2 was determined from the concentration of the peroxide complex obtained after dissolving the colloid in concentrated H_2SO_4 [26].

The nanocrystalline TiO_2 films were prepared on the glass slides by a dip coating technique using 4.5 nm colloids as a precursor. After dipping the glass slides in the concentrated TiO_2 colloidal solution (0.12 M), the samples were dried at elevated temperature (110 °C) for 30 min. The thickness of the nanocrystalline TiO_2 films (0.4–0.5 μm) was adjusted by repeating the above mentioned procedure.

The surface modification of nanocrystalline TiO_2 films was accomplished in the dark by immersion of the samples in a water solution containing 0.05 M alanine and 0.05 M $AgNO_3$ for more than 24 h. After that the samples were rinsed with distilled water and dried in a stream of nitrogen.

Illumination of surface modified TiO_2 nanocrystalline films, almost instantaneously led to the reduction of silver ions to metallic silver. An UV-Xe lamp (Orion Corp.) was employed for steady state illumination. After illumination the samples were immersed for a few seconds in 0.1 M HCl, then rinsed with distilled water and dried in a stream of nitrogen.

The UV–vis absorption spectra of precursor TiO_2 colloid and corresponding nanocrystalline TiO_2 support, as well as deposited silver films on nanocrystalline TiO_2 support were measured using a Thermo Evolution 600 spectrophotometer.

Transmission electron microscopy (TEM) was performed using a JEOL JEM-2100 LaB_6 instrument operated at 200 kV. TEM images were acquired with a Gatan Orius CCD camera at 2× binning. The atomic force microscopy (AFM) studies were performed in the tapping mode at a scanning frequency of 2 Hz using "Ascope 250+" instrument (Quesant Instrument Corporation).

2.2. Photocatalytic degradation of crystal violet

Photocatalytic ability of nanocrystalline TiO_2 films after deposition of silver was compared with photocatalytic ability of pristine TiO_2 films using degradation of organic dye crystal violet (CV) as a test. The photochemical reactor consisted of UV lamp (Roth Co., 16 W, 2.5 mW/cm^2, λ_{max} = 366 nm) positioned annular to the 50 ml quartz flask. The rates of photocatalytic degradation of CV were followed for different initial concentrations in the range from 5.0 to 10.0 μM. The acidity of solutions was not adjusted and pH values were in the range from 6.7 to 7.0. The blank experiments, direct photolysis of CV, were also performed. In order to test performance of nanocrystalline TiO_2 films under long run working

conditions, photocatalytic degradation of organic dye was studied in a repeated cycles.

Initial concentrations of organic dye, as well as its decrease during photodegradation reaction were determined by measuring absorption at the peak position of CV (λ_{max} = 590 nm; ε_{590} = 8.7 × 10^4 M^{-1} cm^{-1}).

2.3. Antimicrobial activity tests

The antimicrobial activity of silver films on nanocrystalline TiO_2 support was evaluated against Gram-negative bacteria *E. coli* (ATCC 25922), Gram-positive bacteria *S. aureus* (ATCC 25923) and fungi *C. albicans* (ATCC 24433) using the standard test method (Standard test method for determining the antimicrobial activity of immobilized antimicrobial agents under dynamic contact conditions, ASTM E 2149-01) with some modifications [27]. Briefly, the glass slides (1.5 cm × 2.0 cm) with TiO_2–Ag films were submersed in flask with 10 ml saline inoculated with appropriate microorganism. The controls were nanocrystalline TiO_2 films on glass slides. The flasks were shaken in a water bath at 150 rpm for a proper time at 37 °C. After that, the 1 ml aliquot was taken and diluted in saline. From each dilution, the 1 ml aliquot was plated in TSA (tryptone soy agar, Torlak, Serbia). The inoculated plates are incubated at 37 °C for 24 h and surviving cells are counted. The percentage of microbial cells reduction (R, %) was calculated using the following equation:

$$R = \frac{C_{0-}C}{C_0} \times 100 \tag{1}$$

where C_0 (CFU – colony forming units) is the number of microbial colonies in the control sample (nanocrystalline TiO_2 film) and C (CFU) is the number of microbial colonies on the deposited silver films on nanocrystalline TiO_2 support. All antimicrobial tests were performed in dark and stated values are averages from three sets of measurements.

3. Results and discussion

3.1. Characterization of silver films on nanocrystalline TiO_2 supports

Conventional TEM image at high magnification of colloidal TiO_2 nanoparticles, used as a precursor in the dip coating process for preparation of thin TiO_2 films, is shown in Fig. 1. TEM measurements revealed the presence of nearly spherical TiO_2 nanoparticles with low degree of crystallinity and average size of 4.5 nm. Fast Fourier transform of the image, shown as an inset to
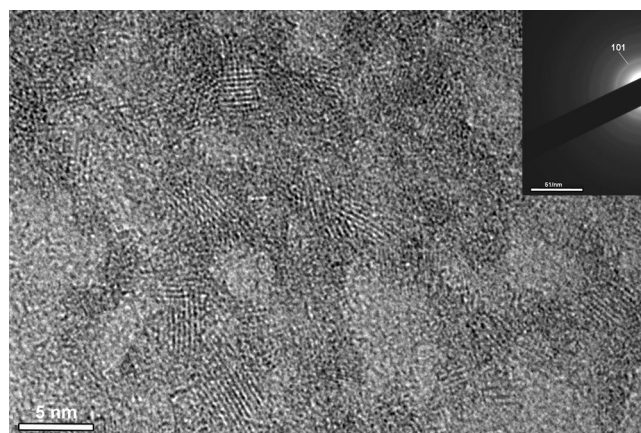
Fig. 1. Typical TEM image of colloidal TiO_2 nanoparticles used for preparation of nanocrystalline TiO_2 films. Inset shows SAED image.
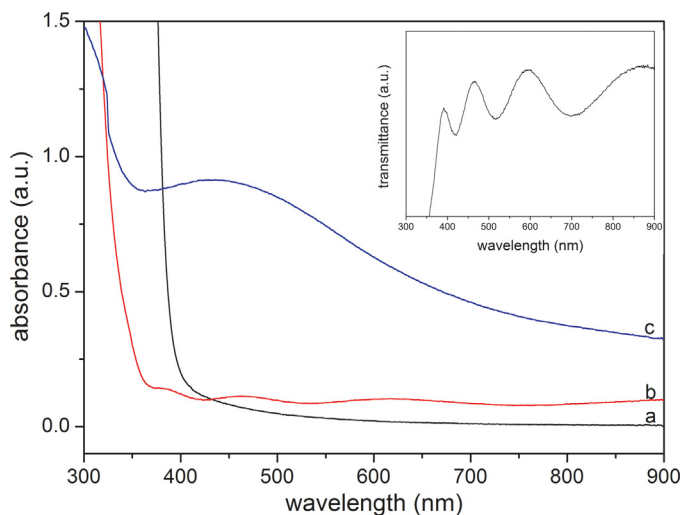
Fig. 2. Absorption spectra of precursor 4.5 nm TiO$_2$ colloid (a), nanocrystalline TiO$_2$ film (b), and photochemically deposited metallic silver on nanocrystalline TiO$_2$ film (c). Inset shows transmission spectrum of nanocrystalline TiO$_2$ film with interference fringes.

Fig. 1, indicated that observed lattice fringe is close to the (1 0 1) anatase value (0.36 nm).

The absorption spectra of precursor (TiO$_2$ colloid) and corresponding nanocrystalline TiO$_2$ film obtained by dip coating technique are shown in Fig. 2 (curves a and b, respectively). In both cases, steep increase of absorbance bellow 380 nm can be noticed, which corresponds to the characteristic band gap energy of anatase titania (3.2 eV).

The thickness of the nanocrystalline TiO$_2$ films on the glass slides was determined from the transmission spectra measured in the spectral range of 350–900 nm. Typical transmission spectrum of nanocrystalline TiO$_2$ film is shown as inset to Fig. 2. The method proposed by Babu et al. [28] was used to calculate thickness of TiO$_2$ films from the position of interference fringes in transmission spectra. Briefly, locations of the extrema in the transmission curve are uniquely determined in a first approximation by specifying the product nd, where n is refractive index and d is thickness of the thin film. In this approximation, which is applicable for weakly absorbing films, extrema occur at wavelengths specified by

$$\lambda = \left(\frac{m}{4nd}\right)^{-1} \quad m = 1, 2, \ldots \quad (2)$$

i.e., the locations of the extrema are uniquely determined by nd. If m' is the order of an extremum from an arbitrary reference extremum (of order m_0), then $m = m_0 + m'$ and
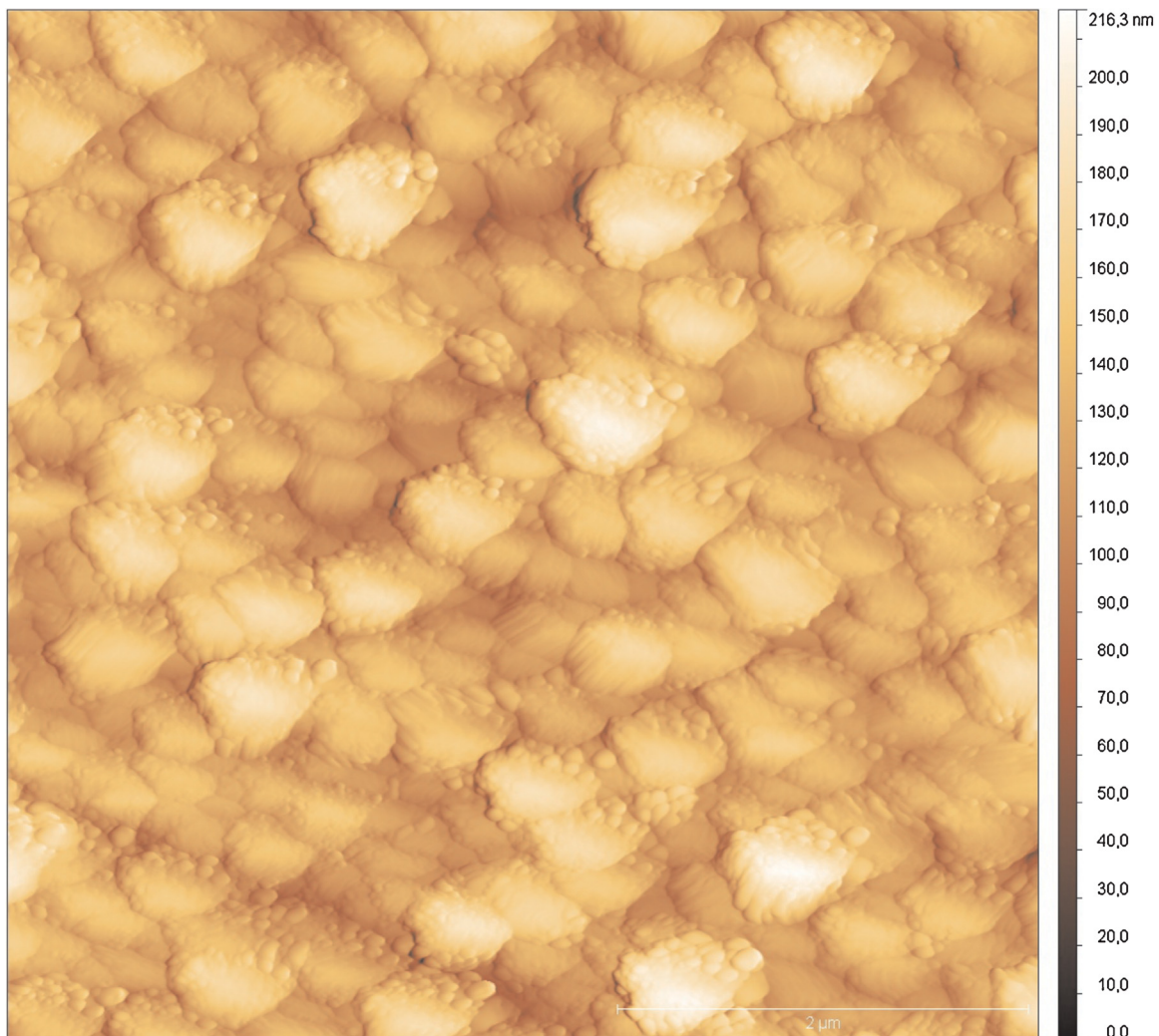
Fig. 3. Typical AFM image of silver grains on the surface of nanocrystalline TiO$_2$ film.

$$\frac{1}{\lambda_{\text{ext}}} = \left(\frac{m_0}{4nd}\right) + \left(\frac{m'}{4nd}\right) \qquad (3)$$

A plot of $1/\lambda_{\text{ext}}$ versus m', for a constant value of nd, will yield a straight line of slope $1/4nd$ and intercept $m_0/4nd$.

Knowing the value of the refractive index of anatase TiO$_2$ particles ($n = 2.524$), estimated thickness of all nanocrystalline TiO$_2$ films used further in experiments was in the range from 0.4 to 0.5 μm. Also, it should be pointed out that dip coating technique led to the formation of nanocrystalline TiO$_2$ films having a fairly uniform thickness across the film.

In order to efficiently deposit silver on nanocrystalline TiO$_2$ films, surface modification with simple amino acid alanine was performed in the presence of silver ions. It is well-known that nanocrystalline TiO$_2$ differs from the bulk material, and has unique surface chemistry due to distortions in surface Ti sites from the octahedral geometry to a penta-coordinate square pyramid with one double Ti= O bond [29,30]. The way of binding between surface Ti atoms and alanine was already described in our previous work [31]. Nanosized surface-modified TiO$_2$ offers several advantages for photocatalytic reduction of metal ions over the commercially available microparticle TiO$_2$: high surface area, increased adsorption of metal ions and enlarged charge separation distances.

Following illumination of dry samples with ultraviolet light, photogenerated electrons are transferred to the chelated silver ions adsorbed onto the surface, and as a consequence, metallic silver can be generated on the nanometer range length scale.

Photogenerated holes on the other hand can oxidize excess alanine adsorbed to surface Ti atoms. In order to remove alanine and unreduced silver ions from the photocatalytically deposited silver films on nanocrystalline TiO$_2$ support the samples were treated with diluted mineral acid (0.1 M HCl). Basically, this process resembles to the fixation process in photography. The absorption spectrum of photochemically deposited metallic silver on nanocrystalline TiO$_2$ support is shown in Fig. 2 (curve c). The presence of surface plasmon resonance band around 440 nm indicated that the grain size of silver is in the nanometer size range.

The morphology of deposited silver film on nanocrystalline TiO$_2$ support was investigated by using AFM measurements. Typical AFM image shows reasonable flat surface across the nanocrystalline TiO$_2$ film (Fig. 3). Also, AFM measurements indicate that homogeneous silver film consisting of well resolved grains with average size of about 80 nm is successfully assembled. It should be noticed that AFM data concerning grain size and optical properties of thin silver films are in agreement.

These results are in agreement with published data concerning photocatalytic reduction of silver, copper and gold ions to corresponding metals by using dry nanocrystalline TiO$_2$ films surface modified with aliphatic amino acids [12,13]. Purpose of these studies was development of simple procedure for formation of metallic pattern structure on nonconductive support, which is important technological process in microelectronics [32]. In this study, additional functions, antimicrobial ability and improvement of photocatalytic performance of TiO$_2$ films upon deposition of silver were tested.
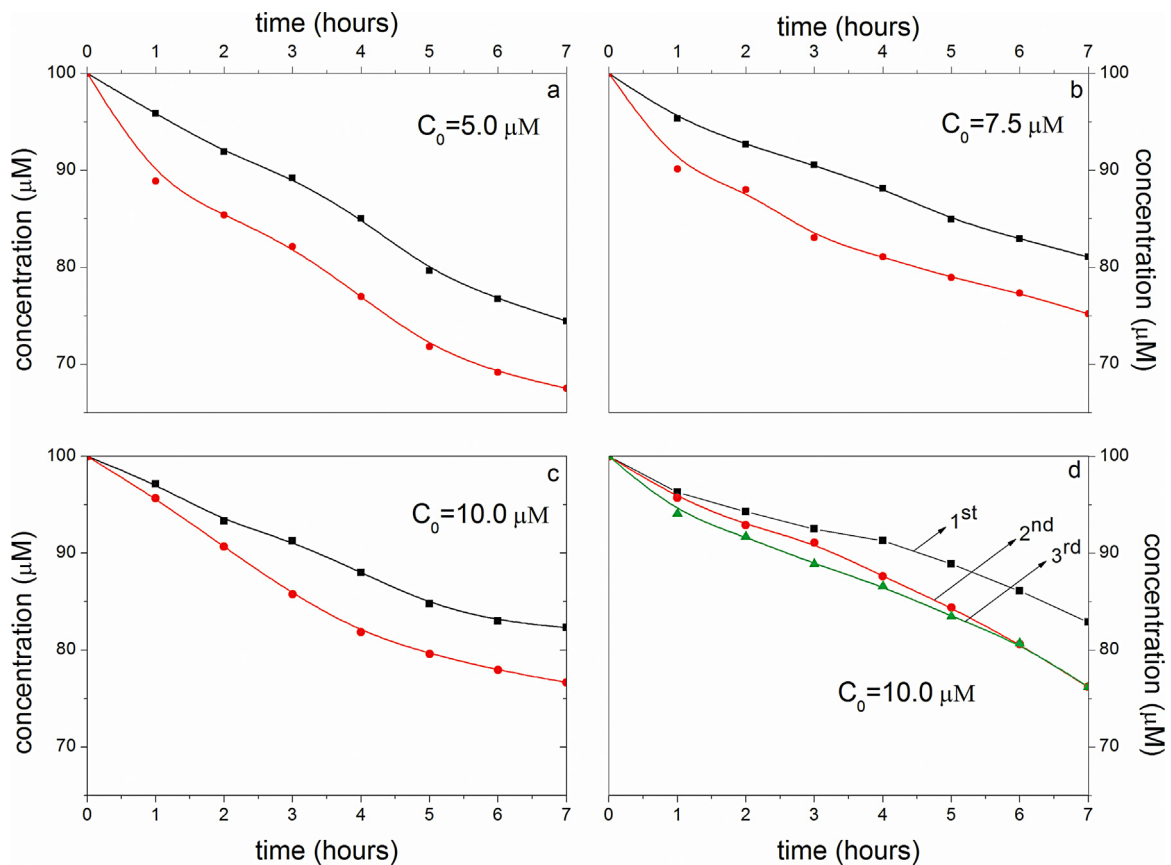
Fig. 4. Degradation kinetic of CV using pristine nanocrystalline TiO$_2$ films (black squares) and nanocrystalline TiO$_2$ films with deposited silver (red dotes) as a function of initial concentration of organic dye: (a) 5.0 μM, (b) 7.5 μM, and (c) 10.0 μM. Degradation kinetic of CV as a function of repeated cycles (initial concentration of CV was 10.0 μM) using pristine nanocrystalline TiO$_2$ film as photocatalyst (d). (For interpretation of the references to color in this figure legend, the reader is referred to the web version of this article.)

3.2. Effect of silver on photocatalytic degradation of crystal violet over nanocrystalline TiO2 films

Effect of deposited silver on photocatalytic performance of nanocrystalline TiO_2 films was investigated using degradation of organic dye CV as a test reaction. The organic dye CV was chosen for this purpose because direct photolysis does not induce its degradation. The comparison between kinetics of photocatalytic degradation of CV for different initial concentrations over pristine nanocrystalline TiO_2 films and nanocrystalline TiO_2 films with deposited silver is shown in Fig. 4 (a–c). Complete decolorization of organic dye was not achieved after 24 h of illumination, but based on the degradation kinetics data some general features can be recognized. First, the photocatalytic degradation for all initial concentrations of CV is slower over pristine nanocrystalline TiO_2 films compared to nanocrystalline TiO_2 films with deposited silver. As expected, in the presence of nanosized silver electron transfer rates of photogenerated charge carriers are enhanced reducing their recombination. This result is in agreement with literature data concerning Ag–TiO_2 nanocomposites consisting of hollow spheres whose photocatalytic activity were higher compared to pure TiO_2 and commercial Degussa P25 powders [33]. Second, the photocatalytic degradation kinetics of CV slowed down with the increase of initial concentration of organic dye for both kinds of films. This effect can be easily explained with limited number of available TiO_2 surface sites for adsorption of organic dye. Also, it should be mentioned that in all experiments pH of the solutions was in between 6.7 and 7.0. It is well known that TiO_2 is amphoteric and that the zero point charge is at $pH_{zpc} \approx 5.9$ [34]. Under such experimental conditions, the electrostatic attraction between positively charged organic dyes and negatively charged, i.e., deprotonated surface —OH groups is the driving force for adsorption of organic dyes. In addition, the formation rate of hydroxyl radicals, major active species during photocatalytic oxidation reaction, is much higher in the case of anatase compared to other semiconductors [35].

In order to test the photocatalytic ability of nanocrystalline TiO_2 films with and without deposited silver under long run working conditions, the degradation of CV was ascertained in repeated cycles without the photocatalyst being subject to any cleaning treatments. The subsequent degradation kinetic curves for CV using pristine nanocrystalline TiO_2 film as photocatalyst are shown in Fig. 4d. Identical behavior was also observed in the experiments with nanocrystalline TiO_2 films with deposited silver (results are not shown). It is noticeable by comparing the first kinetic cycle with the second as well as the third one that the photocatalytic ability of pristine nanocrystalline TiO_2 film is improving. Most likely, enhanced photocatalytic ability of TiO_2 films in repeated photocatalytic cycles can be explained by self-cleaning effect, i.e., removal of residual impurities from the surface of nanocrystalline TiO_2 film.

3.3. Antimicrobial activity of silver films on nanocrystalline TiO2 support

Antimicrobial and antifungal efficiency as an additional function of silver films photochemically deposited on nanocrystalline TiO_2 support was tested against Gram-negative bacteria E. coli and Gram-positive bacteria S. aureus, as well as yeast C. albicans. It is well known that TiO_2 particles under UV light have pronounced antibacterial activity [36,37]. In order to ensure that reduction of both bacteria and yeast is exclusively consequence of antibactericidal activity of silver films, all measurements were performed in dark. The obtained results after 24 h of contact in dark of various bacterial colonies with silver films are collected in Table 1. The silver films ensured maximum reduction of both bacteria, while the fungi reduction reached satisfactory 98.45%.

In order to determine differences in biological response of various microbial species (E. coli, S. aureus and C. albicans) exposed to silver films deposited on nanocrystalline TiO_2 support microbial cells reduction measurements were performed as a function time (from 2 to 60 min). The obtained data are presented in Fig. 5. It is clear that biological response is different for different microbial species and in entire time interval the microbial cells reduction in ascending order from C. albicans, over S. aureus to E. coli can be observed. Also, the differences of antimicrobial activities against various microbial strains are becoming more pronounced at shorter exposure times. For example, after 2 min of contact only reduction of E. coli was observed (slightly above 50%), while exposure of S. aureus and C. albicans to silver films deposited on nanocrystalline TiO_2 supports was uneffective. After 15 min of exposure, cells reduction of E. coli reached 96.3%, while for S. aureus and C. albicans was found to be 33.3 and 16.3%, respectively.

Different microbial species have different protective mechanisms when exposed to silver. Hwang et al. [38] showed that elevated accumulation of intracellular reactive oxygen species (ROS) in C. albicans cells is the main antifungal activity of silver nanoparticles. The accumulation of ROS induces and regulates the induction of apoptosis in yeasts. However, the C. albicans cells can produce the antioxidative enzyme–catalase that can protect the cells from the antimicrobials and oxidative damage [39]. Similar protective mechanism can be found in S. aureus strains that also produce catalase and other antioxidants, including, alkyl hydro-peroxide reductase, and staphyloxanthin, which may supplement catalase in defense against H_2O_2 and ROS [40]. Among tested organisms, only E. coli that showed the highest sensitivity upon exposure to silver, does not produce catalase. In addition to catalase action, there is a difference in cell wall composition between Gram-positive and Gram-negative species, which is responsible for smaller bactericidal effect of silver on S. aureus in comparison to E. coli [41].

Table 1
The percentage of cells reduction (R, %) of E. coli, S. aureus and C. albicans after 24 h of contact in dark with silver films deposited on nanocrystalline TiO_2 support.

Sample	E. coli		S. aureus		C. albicans	
	N/ml	R (%)	N/ml	R (%)	N/ml	R (%)
TiO_2 film (control)	1.2×10^7	99.99	1.8×10^7	99.99	1.1×10^7	98.45
TiO_2–Ag film	5.6×10^2		1.1×10^2		1.7×10^5	
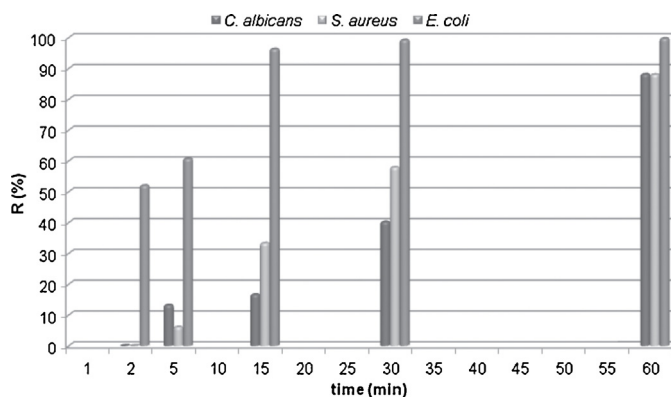
Fig. 5. The percentage of reduction of E. coli, S. aureus and C. albicans as a function of time of contact between microbial cells and silver films deposited on nanocrystalline TiO_2 supports; for the sake of clarity time scale is not proper.

4. Conclusion

Nanocrystalline TiO$_2$ films were prepared on glass slides by dip coating technique using colloids consisting of 4.5 nm TiO$_2$ nanoparticles as a precursor. Deposition of silver on nanocrystalline TiO$_2$ support was achieved using simple and non-expensive photocatalytic route. Deposited silver films proved to have excellent antimicrobial activity against Gram-negative bacteria *E. coli* and Gram-positive bacteria *S. aureus*, as well as fungus *C. albicans*. The different biological response of different microbial species was observed when contact between the microbial cells and silver was on a time scale of minutes. Also, the effect of silver on photocatalytic performance of nanocrystalline TiO$_2$ films was tested using degradation kinetic of the organic dye crystal violet as a test reaction. The obtained kinetic data indicated improvement of photocatalytic ability of nanocrystalline TiO$_2$ films after deposition of silver. Most likely, this effect is a consequence of reduced recombination of photogenerated charge carriers due to enhancement of their electron transfer rates.

References

[1] M.R. Hoffman, S.T. Martin, W.Y. Choi, D.W. Bahnemann, Chem. Rev. 95 (1995) 69.
[2] U. Stafford, K.A. Gray, P.V. Kamat, Heterogen. Chem. Rev. 3 (1996) 77–104.
[3] T. Rajh, A.E. Ostafin, O.I. Mićić, D.M. Tiede, M.C. Thurnauer, J. Phys. Chem. 100 (1996) 4538–4545.
[4] F. Forouzan, T.C. Richards, A.J. Bard, J. Phys. Chem. 100 (1996) 18123–18127.
[5] B. Ohtani, Chem. Lett. 37 (2008) 216–229.
[6] A. Kubacka, M. Fernandez-Garcia, G. Colon, Chem. Rev. 112 (2011) 1555–1614.
[7] E. Barborini, A.M. Cont, I. Kholmanov, P. Piseri, A. Podesta, P. Milani, C. Cepek, O. Sakho, R. Macovez, M. Sancrotti, Adv. Mater. 17 (2005) 1842–1846.
[8] M.V. Dozz, E. Selli, J. Photochem. Photobiol. C 14 (2013) 13–28.
[9] M. Chiodi, C.P. Cheney, P. Vilmercati, E. Cavaliere, N. Mannella, H.H. Weitering, L. Gavioli, J. Phys. Chem. C 116 (2011) 311–318.
[10] A. Naldoni, M. D'Arienzo, M. Altomare, M. Marelli, R. Scotti, F. Morazzoni, E. Selli, V. Dal Santo, Appl. Catal. B 130–131 (2013) 239–248.
[11] J.T. Carneiro, T.J. Savenije, G. Mul, Phys. Chem. Chem. Phys. 11 (2009) 2708–2714.
[12] T. Rajh, J. Nedeljkovic, L.X. Chen, D.M. Tiede, M.C. Thurnauer, J. Adv. Oxid. Tech. 3 (1998) 292–298.
[13] I. Ruvarac-Bugarčić, I. Janković, Z. Konstantinović, Z. Šaponjić, J. Nedeljković, Acta Chim. Slov. 55 (2008) 268–272.
[14] A. Panacek, L. Kvitek, R. Prucek, M. Kolar, R. Vecerova, N. Pizurova, V.K. Sharma, T. Nevecna, R. Zboril, J. Phys. Chem. B 110 (2006) 16248–16253.
[15] H.J. Lee, S.Y. Yeo, S.H. Jeong, J. Mater. Sci. 38 (2003) 2199–2204.
[16] S.H. Jeong, Y.H. Hwang, S.C. Yi, J. Mater. Sci. 40 (2005) 5413–5418.
[17] T. Yuranova, A.G. Rincon, C. Pulgarin, D. Laub, N. Xantopoulos, H.J. Mathieu, J. Photochem. Photobiol. A 181 (2006) 363–369.
[18] N. Vigneshwaran, A.A. Kathe, P.V. Varadarajan, R.P. Nachane, R.H. Balasubramanya, J. Nanosci. Nanotechnol. 7 (2007) 1893–1897.
[19] M. Radetić, V. Ilić, V. Vodnik, S. Dimitrijević, P. Jovančić, Z. Šaponjić, J.M. Nedeljković, Polym. Adv. Technol. 19 (2008) 1816–1821.
[20] V. Ilić, Z. Šaponjić, V. Vodnik, R. Molina, S. Dimitrijević, P. Jovančić, J. Nedeljković, M. Radetić, J. Mater. Sci. 44 (2009) 3983–3990.
[21] V. Ilić, Z. Šaponjić, V. Vodnik, B. Potkonjak, P. Jovančić, J. Nedeljković, M. Radetić, Carbohyd. Polym. 78 (2009) 564–569.
[22] V. Ilić, Z. Šaponjić, V. Vodnik, S. Lazović, S. Dimitrijević, P. Jovančić, J. Nedeljković, M. Radetić, Ind. Eng. Chem. Res. 49 (2010) 7287–7293.
[23] O. Baghriche, A.P. Ehiasarian, E. Kusiak-Nejman, C. Pulgarin, R. Sanjines, A.W. Morawski, J. Kiwi, J. Photochem. Photobiol. A 227 (2012) 11–17.
[24] O. Baghriche, S. Rtimi, C. Pulgarin, R. Sanjines, J. Kiwi, J. Photochem. Photobiol. 251 (2013) 50–56.
[25] T. Rajh, Z.V. Šaponjić, O.I. Mićić, Langmuir 8 (1992) 1265–1270.
[26] R.C. Thompson, Inorg. Chem. 23 (1984) 1794–1798.
[27] A. Varesano, C. Vineis, A. Aluigi, F. Rombaldoni, Antimicrobial polymers for textile products, in: A. Mendez-Vilas (Ed.), Science against Microbial Pathogens: Communicating Current Research and Technological Advances, Vol. 3, Microbiology Series No. 3, Vol. 1, Formatex, Badajoz, Spain, 2011, pp. 99–110.
[28] S.V. Babu, M. David, R.C. Patel, Appl. Opt. 30 (1991) 839–846.
[29] L.X. Chen, T. Rajh, W. Jeger, J. Nedeljković, M.C. Thurnauer, J. Synchrotron Rad. 6 (1999) 445–447.
[30] T. Rajh, J.M. Nedeljković, L.X. Chen, O. Poluektov, M.C. Thurnauer, J. Phys. Chem. B 103 (1999) 3515–3519.
[31] A.I. Ruvarac-Bugarčić, Z.V. Šaponjić, S. Zec, T. Rajh, J.M. Nedeljković, Chem. Phys. Lett. 407 (2005) 110–113.
[32] T. Rajh, N. Meshkov, J.M. Nedeljković, L.R. Skubal, D.M. Tiede, M. Thurnauer, U. S. Patent No. 6,271,130 B1, 2001.
[33] Q. Xiang, J. Yu, B. Cheng, H.C. Ong, Chem. Asian J. 5 (2010) 1466–1474.
[34] M. Kosmulski, Adv. Colloid Interface Sci. 99 (2002) 255–264.
[35] Q. Xiang, J. Yu, P.K. Wong, J. Colloid Interface Sci. 357 (2011) 163–167.
[36] D. Mihailović, Z. Šaponjić, M. Radoičić, T. Radetić, P. Jovančić, J. Nedeljković, M. Radetić, Carbohyd. Polym. 79 (2010) 526–532.
[37] D. Mihailović, Z. Šaponjić, R. Molina, N. Pauč, P. Jovančić, J. Nedeljković, M. Radetić, ACS Appl. Mater. Inter. 2 (2010) 1700–1706.
[38] I.-S. Hwang, J. Lee, J.H. Hwang, K.-J. Kim, D.G. Lee, Fed. Eur. Biochem. Society J. 279 (2012) 1327–1338.
[39] C.E.B. Linares, D. Griebeler, D. Cargnelutti, S.H. Alves, V.M. Morsch, M.R.C. Schetinger, J. Med. Microbiol. 55 (2006) 259–262.
[40] B. Park, V. Nizet, G.Y. Liu, J. Bacteriol. 190 (2008) 2275–2278.
[41] S.H. Kim, H.S. Lee, D.S. Ryu, S.J. Choi, D.S. Lee, Korean J. Microbiol. Biotechnol. 39 (2011) 77–85.

Silicon going indoor

Djordje Jovanović[1], Tijana Tomašević-Ilić[1], Nikola Tasić[2], Aleksandar Matković[1,3], Marko Spasenović[1], Radoš Gajić[1], and Emmanuel Kymakis[4]

[1]*Graphene Laboratory, Center for Solid State Physics and New Materials, Institute of Physics, University of Belgrade, Pregrevica 118, 11080 Belgrade, Serbia*
[2]*Department of Materials Science, Institute for Multidisciplinary Research, University of Belgrade, Kneza Višeslava 1,11000 Belgrade, Serbia*
[3]*Institut für Physik, Montanuniversität Leoben, Franz-Josef-Straße 18, 8700 Leoben, Austria*
[4]*Electrical Engineering Department, Technological Educational Institute (TEI) of Crete, Heraklion, 71004 Crete, Greece*

We develop and test low-light efficient graphene/n-Si Schottky junction solar cells (SCs) based on liquid phase exfoliated (LPE) graphene produced by *Langmuir-Schaefer* (LS) assembly. SCs performances are tested under different light intensities of the solar simulator. Our SCs have better performances in indoor then outdoor light conditions. For illumination of only 0.002 Sun, the SCs have up to 10% efficiency and just 0.2% for illumination of 1 Sun, which is about 50 times efficiency increase. This result is, according to our knowledge, highest efficiency solar cells made by LPE 2D materials and is better than commercial Si solar cells in indoor conditions. SC performance in low light regime mainly depends on high shunt (parallel) resistance of solar cells. Better performances in low-light regime proposed their usage in indoor conditions. Furthermore, the low cost of the graphene films we used will have an impact on faster adoption of these specific devices.

P-type field-effect transistors based on liquid phase exfoliated MoS$_2$

Tijana Tomašević-Ilić
Aleksandar Matković, Jasna Vujin, Radmila Panajotović, Marko Spasenović, Radoš Gajić

Graphene Laboratory (GLAB) of the Center for Solid State Physics and New Materials, Institute of Physics, University of Belgrade, Pregrevica 118, 11080 Belgrade, Serbia
Institute of Physics, Montanuniversität Leoben, Franz Josef Straße 18, A-8700 Leoben, Austria

ttijana@ipb.ac.rs

Abstract

Two-dimensional (2D) materials are a new class of materials with interesting physical properties and applications. The most studied 2D semiconducting dichalcogenide MoS$_2$ is gaining importance as a promising channel material for field-effect transistors (FETs) [1]. Liquid phase exfoliation (LPE) is a promising route for large-scale production of 2D materials [2]. However, the MoS$_2$ films produced with LPE showed low carrier mobility [3]. The assembly of nanomaterials in thin films directly affects their morphology and electronic properties with ordered packing usually resulting in superior film quality and device performance. Integrating nanomaterials into FETs requires reliable assembly methods to fabricate relatively uniform thin films. In our work, we describe controlled deposition of few-layer MoS$_2$ films using a modified Langmuir-Schaefer (LS) method and perform mobility measurements on few-layer MoS$_2$ FETs (Fig. 1). Our films showed p-type conduction and mobility larger than 60 cm2 V^{-1}s^{-1} at room temperature in air (Fig. 2). This is the largest ever achieved mobility for FET devices from LPE MoS$_2$, comparable to the previously reported p-type MoS$_2$ FET from chemically doped CVD samples [4]. Our facile and reproducible method results in high-quality films that seriously compete with CVD films as materials of choise for applications in electronics.

References

[1] Radisavljevic B. *et al*., Nature Materials 12, (2013) 815-820.
[2] Coleman J. et al., Science, 331(2011)568
[3] Li J. Advanced Functional Materials, 24 (2014) 6524-6531
[4] Liu X. et al., Advanced Materials, 28 (2016) 2345-51

Figures
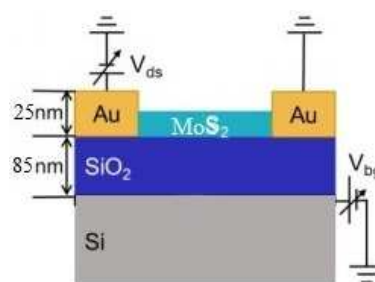
Figure 1: Schematic "cross-sectional" view of the device
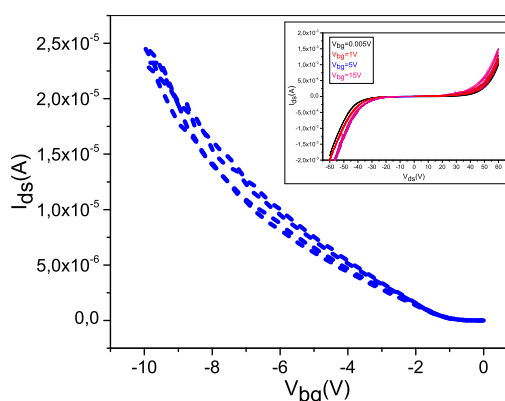
Figure 2: Room-temperature transfer characteristics with 100 mV applied bias voltage, and output characteristics Ids-Vds measured for different gate voltages (inset).

Enhancing conductivity of self-assembled transparent graphene films with UV/Ozone Treatment

T. Tomasević-Ilić[1], Đ. Jovanović[1], J. Pešić[1], A. Matković[1, 2], M. Spasenović[1], R. Gajić[1]

[1]*Graphene Laboratory (GLAB) of the Center for Solid State Physics and New Materials, Institute of Physics, University f Belgrade, Pregrevica 118, 11080 Belgrade, Serbia*
[2]*Present address: Institute of Physics, Montanuniversität Leoben, Franz Josef Straße 18, 8700 Leoben, Austria*
e-mail:ttijana@ipb.ac.rs

We demonstrate enhanced electrical conductivity of self-assembled transparent large area graphene films by UV/ozone treatment. Graphene as a material with high optical transparency and conductivity is an excellent choice for transparent electrodes in various optoelectronic devices [1]. Langmuir-Blodgett (LB) and Langmuir-Shaefer (LS) assembly are methods for simple, large-scale and cost-effective production of thin graphene films [2]. However, uncontrollable monolayer assembly into thin films and large defect density often leads to reduced LB and LS film conductivity. There is much effort to decrease sheet resistance of these films with annealing, chemical doping and functionalization [3, 4]. Here, we examine the effects of exposure to ultraviolet radiation and ozone (UVO) on LB/LS self-assembled graphene thin films by UV/VIS spectrophotometry, resistance measurements and Raman spectroscopy. We observe that the intensity of the D peak in Raman spectra of our graphene films decreases after UVO exposure, indicating a lower defect density. Also, sheet resistance decreased by an order of magnitude without loss in film transparency. We conclude that in contrast to the degrading effects it has on mechanically exfoliated and CVD-grown single layer graphene [5, 6], UVO treatment on LB/LS self-assembled graphene thin films leads to local defect patching which enhances the film conductivity while retaining the high optical transparency. We propose that our approach is suitable for various materials with a multitude of active edges and a large area of reactive surface making the solution-processed thin films usablein practical optoelectronics applications.

REFERENCES

[1] F. Bonaccorso et al., Nat. Photonics 4, 611 (2010).
[2] Li X. et al., Nat. Nanotechnol. 3, 538 (2008).
[3] T. Tomasevic et al., Opt. Quant. Electron. 48, 319 (2016).
[4] A. Matkovic et al., 2D Mater. 3 015002 (2016).
[5] E. X. Zang et al., Appl. Phys. Lett. 101, 121601 (2012).
[6] S. Zhao et al., Nanotechnol. 23, 355703 (2012).

Ab-initio study of optical properties of MoS$_2$ and WS$_2$ compared to spectroscopic results of liquid phase exfoliated nanoflakes

Jelena Pešić[1], Jasna Vujin[1], Tijana Tomašević-Ilić[1], Marko Spasenović[1], Radoš Gajić[1]

[1]*Graphene Laboratory (GLAB) of the Center for Solid State Physics and New Materials,*
Institute of Physics, University of Belgrade,
Pregrevica 118, Belgrade, 11080, Serbia
e-mail: yelena@ipb.ac.rs

MoS$_2$ and WS$_2$ are part of the family of transition metal dichalcogenide crystals (TMDC). TMDCs have emerged as a new class of semiconductors that display distinctive properties at a thickness of one and few layers [1-3]. They have also attracted much interest for applications in optoelectronics as detectors, photovoltaic devices and light emitters [4-8].

Spectroscopic techniques are among the most important methods for research in the field of nanoscience and nanotechnologies. Parallel with the development of experimental methods, computational science becomes a very valuable tool in pursuit for new low-dimensional materials and their characterization. Employing high-end modeling codes, it is possible to simulate from first principles more than a few spectroscopic techniques. Using approaches based on density functional theory (DFT), including density functional perturbation theory, time-dependent DFT and many-body perturbation theory, implemented in the Quantum Espresso software package [9], we study optical properties of low-dimensional materials, MoS$_2$ and WS$_2$.

We calculate the dielectric function within the framework of the random-phase approximation (RPA) [10] based on DFT ground-state calculations, starting from eigenvectors and eigenvalues all calculated with Quantum Espresso. The final goal of our theoretical work is a comparison to corresponding experimental data. We compare our computational results with optical measurements on MoS$_2$ and WS$_2$ nanoflakes. MoS$_2$ and WS$_2$ were exfoliated by ultrasonic treatment in low-boiling point organic solvent [11-15] and characterized using UV/VIS spectrophotometry. We use our results for analysis of optical properties of liquid phase exfoliated MoS$_2$ and WS$_2$ nanoflakes, as a proven method for analysis of basic optical properties of 2D materials [11].

REFERENCES
[1] S. Z. Butler, et al., ACS Nano 7, 2898 (2013).
[2] Q. H. Wang, et al., Nat Nano 7, 699 (2012).
[3] X. Xu et al., Nat Phys 10, 343 (2014).
[4] A. Pospischil, M. M. Furchi, and T. Mueller, Nat Nano 9, 257 (2014).
[5] B. W. H. Baugher, et al., Nat Nano 9, 262 (2014).
[6] L. Britnell, et al., Science 340, 1311 (2013).
[7] F. H. L. Koppens, et al., Nat Nano 9, 780 (2014).
[8] J. Ross, Nat Nanotechnol. 4, 268 (2014).
[9] P. Giannozzi et al., J. Phys.:Condens. Matter 21 395502 (2009) http://www.quantum-espresso.org
[10] Brener, N.E., Phys. Rev. B 12, 1487, (1975).
[11] A. Matković et al., 2D Mater. 3(1), 015002 (2016).
[12] T. Tomašević-Ilić, et al. Opt Quant Electron 48: 319, (2016).
[13] T. Tomašević-Ilić et al., submitted (2017).
[14] R. Panajotović et al. Book of Abstracts, SPIG 2016, 182-185, (2016).
[15] J. Vujin et al. Book of Abstracts RAD 2016, (2016).
[16] J. Pešić et al. , Opt Quant Electron, 48:368 (2016).

P54

Szén alapú bio-nanokompozitok optoelektronikai alkalmázásának lehetőségei

SZABÓ TIBOR[1,2], T. TOMASHEVIC[3], R. PANAJOTOVIĆ[3], ABD ELAZIZ SARRAI[1,4], SZEGLETES ZSOLT[5], VÁRÓ GYÖRGY[5], HAJDU KATA[1], MÁTHÉ BOTOND[1], SZABÓ ANNA[6], HERNÁDI KLÁRA[6] ÉS **NAGY LÁSZLÓ**[1]

1. Orvosi Fizikai és Orvosi Informatikai, Szegedi Tudományegyetem, Szeged
2. Izotóp Klimatológiai és Környezetkutató Központ (IKER), Magyar Tudományos Akadémia Atommagkutató Intézet, Debrecen
3. Institute of Physics, University of Belgrade, Belgrade, Serbia
4. Laboratory for Biomaterials and Transport Phenomena LBMPT, University Yahia Fares, Medea, Algeria;
5. Biofizikai Intézet, Magyar Tudományos Akadémia, Szegedi Biológiai Kutatóközpont, Szeged
6. Alkalmazott és Környezeti Kémiai Tanszék, Szegedi Tudományegyetem, Magyarország

Funkcionális bio-hibrid nanokompozit anyagokat állítottunk elő bíborbaktériumokból tisztított fotoszintetikus reakciócentrum fehérjéből (RC) és szénalapú nanoszkópikus hordozó anyagokból (szén nanocsövekből, nanocső kötegekből, grafénból). Az így előállított anyagok optikai és elektromos tulajdonságait jellemeztük. A RC-ot sikeresen kötöttük különböző módszerekkel (fizikai szorpció és specifikus kémiai kötésekkel) a szervetlen hordozókhoz, és a fényindukált abszorpcióváltozást, elekromos vezetőképességváltozást mértük. A spektroszkópiai vizsgálatok azt mutatták, hogy a RC a kötődés után is fotoaktív maradt. A sötéten és fényben mért áram/feszültség karakterisztikák azt mutatták, hogy a fotoaktív biológiai és a szervetlen hordozó között elektrosztatikus/elektromos kölcsöhatás lehet. Az eredmények azt mutatták, hogy a fényindukált ellenállásváltozás kialakításában mind a szervetlen hordozóban lejátszódó gerjesztési, mind pedig a RC-ban végbemenő energiadisszipáció szerepet játszhat. A kapott eredméyek segíthetnek újgenerációs optoelektroikai rendszerek (pl. nagy specifitású bioszenzorok, fénnyel működtethető kapcsolók, fotoelektromos energiaátalakító rendszerek, mikroképalkotó rendszerek, stb.) kialakításában.

JEGYZETEK

Transparent and Conductive Films From Liquid Phase Exfoliated Graphene

Marko Spasenović, Tijana Tomašević-Ilić, Aleksandar Matković, Radoš Gajić

Center for Solid State Physics and New Materials, Institute of Physics, Belgrade, Serbia

The lab production of graphene has sparked huge scientific and commercial interest, especially since the discovery of methods to produce graphene in large quantities. Although many of those methods use costly sacrificial growth substrates, liquid phase exfoliation (LPE) with the aid of ultrasound has proven to be a facile, reliable, and economically satisfying solution to producing significant volumes of graphene colloid dispersions. Graphene can be extracted from dispersion to be used in various electronic devices and as a transparent flexible electrode in applications ranging from solar cells to wearable sensors.

We describe transparent and conductive films of LPE graphene deposited from soluation with the Langmuir–Blodgett (LB) method [1]. Graphene sheets (GS) were exfoliated from graphite by ultrasonic treatment in N-Methyl-2-pyrrolidone (NMP) and N, N-dimethylacetamide (DMA) solvents. For comparison, graphene sheets were also exfoliated in a water solution of surfactants. We confirm a higher exfoliation rate for surfactant-based processing compared to NMP and DMA. Furthermore, we demonstrate that our films exfoliated in NMP and DMA, deposited with LB and annealed have a higher optical transmittance and lower sheet resistance compared to films obtained with vacuum filtration, which is a necessary step for GS exfoliated in water solutions. High optical transmittance and low sheet resistance are desirable properties for transparent electrodes. The structural, optical and electrical properties of graphene layers were

ESOF theme:

• Healthy populations
• Material dimensions
• Sustaining the environment
• Turing's legacy – data and the human brain
• Far frontiers
• Living in the Future
• Bio-revolution
• Science for policy and policy for science
• Science in our cultures

characterized with scanning electron microscopy, atomic force microscopy, UV/VIS spectrophotometry and sheet resistance measurements.

Our facile and reproducible method results in high-quality transparent conductive films with potential applications in flexible and printed electronics and coating technology.

Reference:

[1] T. Tomašević-Ilić et al, Opt Quant Electron (2016) 48:319

Low light solar cells

Djordje Jovanović[1], Tijana Tomasević[1], Aleksandar Matković[1,2], Nikola Tasić[3], and Radoš Gajić[1]

[1] EU Centre of Excellence for Optical Spectroscopy Applications in Physics, Institute of Physics Belgrade, University of Belgrade, Serbia
[2] Institut für Physik, Montanuniversität Leoben, Leoben, Austria
[3] Department of Materials Science, Institute for Multidisciplinary Research, University of Belgrade, Serbia

: In this study we have developed and tested low-light Graphene / n-Si Schottky junction solar cells (SC) based on LPE (liquid phase exfoliated) graphene produced by Langmuir-Blodgett assembly (LBA) [1-3]. SCs have about 1% efficiency for 0.25 sun and 0.1% for 2 sun for AM1.5G solar light. When tested upon very weak light intensity for 0.01 sun, with non-standard SC simulator setup, the efficiency is increased by an order of magnitude - over 20%. SCs have better performance in low light that could have applications in these conditions [3]. SCs performance is measured on non-treated (NT) and treated (T) - ozone (O_3) and annealed (A) one layer LBA Graphene films / n-Si. Performance depends mainly on quality of the graphene films (GS). Low cost graphene film production will have an impact on faster adoption of these devices.

1. Aleksandar Matković et al., 2D Mater. 3, 015002 (2016).
2. Lachlan J. Larsen et al., RSC Adv. 5, 38851 (2015).
3. Valentina Janošević et al., Prog.Photovolt: Res. Appl. (2015).

Modification of reduced graphene oxide with gold nanoparticles stabilized by SH-PEG-NH2

A. Leniart1, P.Szustakiewicz1, W. Lewandowki1

1Faculty of Chemistry, University of Warsaw, Laboratory of organic nanomaterials and biomolecules, Pasteur 1 Street, 02-093 Warsaw, Poland

Reduced graphene oxide modified with nanoparticles (RGO / NPs) may, in the future, provide a basis for the development of various technologies. The challenge for us is to optimize the synthesis process and to investigate the physicochemical properties of such composites. The project, which will be presented, consisted of three stages: the synthesis of reduced graphene oxide (RGO), the synthesis of nanoparticles (NPs) and the modification of the reduced graphene oxide with gold nanoparticles. An essential element of the strategy is to achieve stable metallic nanoparticles coated with amino ligands e.g SH-PEG-NH2. An additional objective was to carry out the amidation reaction on the particle surface to covalently bonding RGO and NPs, which can provide the high durability material. The synergy resulting material, composed of nanoparticles disposed on the surface of graphene, combines the properties of both components. The resulting hybrids were examined in transmission electron microscope (TEM) in order to illustrate the topography of the material. To sum up, we were able to get a stable material type RGO / NPs in various solvents. In addition, we have made successful attempts to modify RGO with anisotropic nanoparticles, such as nanoprisms. The resulting material type RGO / NPs opens wide possibilities of application in particular in analytical chemistry, technology SERS or catalysis.

Transparent Graphene Oxide and reduced Graphene Oxide Humidity Sensors

D.-P. Argyropoylos[1], S. Papamatthaiou[1], F. Farmakis[1], N. Georgoulas[1]

Department of Electrical and Computer Engineering, University of Thrace Xanthi, Greece

Graphene oxide (GO) is a promising material for various sensing applications. In this contribution we propose a humidity sensing device based on GO on glass. A GO water-based solution was disposed on glass substrate and with the aid of spin coating method, a thin film was deposited and planar resistive devices were fabricated by depositing Aluminum metal pads through thermal evaporation. Two different spin speeds were applied (3000 and 6000 rpm) to evaluate the effect of GO thickness to the humidity sensing properties. In addition, the devices were subjected to various thermal annealing steps in order to reduce GO and investigate the role of functional oxygen groups to the sensing properties. Furthermore, a transparent device was prepared by depositing ITO contacts with DC magneton sputtering. The resistive behavior was evaluated with current-voltage measurements and it was correlated with the process parameters. The sensing behavior of the devices was investigated through resistance measurements while alternating between vacuum and air conditions. GO sensors at both speeds, exhibit a high sensitivity in humidity of more than 10.000% but lack of stability over several air/vacuum cycles was observed. As expected, thermal reduction of GO largely improves its resistance and after several thermal annealing steps it remains rather constant. The humidity sensing capability of the reduced GO is much lower than GO and it is further decreased after two successive annealing steps and remains constant for any additional step. This behavior is well correlated with the existence of the functional oxygen groups within the GO layer. In all cases, thicker (spin-coated at 3000 rpm) rGO sensors exhibit higher sensitivity and faster response to humidity (<3 s for six times annealed rGO) compared thinner (spin-coated at 6000 rpm) rGO sensors.

"Saint Petersburg OPEN 2016"

3rd International School and Conference on Optoelectronics, Photonics, Engineering and Nanostructures

St Petersburg, Russia, March 28 – 30, 2016

BOOK of ABSTRACTS

Low light low cost solar cells

D Jovanović[1], T Tomašević[1], A Matković[1,2], M Musić[3], N Tasić[4],
M Spasenović[1], and R Gajić[1]
[1]EU Centre of Excellence for Optical Spectroscopy Applications in Physics, Institute of Physics Belgrade, University of Belgrade, Serbia
[2]Institut für Physik, Montanuniversität Leoben, Leoben, Austria
[3]Key to Metals AG, Belgrade, Serbia
[4]Department of Materials Science, Institute for Multidisciplinary Research, University of Belgrade, Serbia

Abstract. In this paper we develop and tasted low light low cost state of the art LPE graphene/n-Si Schottky junction solar cell with 1% efficient for 0.25 sun and 0.1% for 2 sun. The solar cells have better performances in low light than in normal light intensity which recommends it for the applications in low light geographical conditions. There performances mainly depend on the quality of the LPE graphene film and the treatment. Main contribution comes from R_{sheet} of the graphene film. The additional reason comes from treatments of graphene films with ozone, annealing and atmospheric conditions. The second realized main goal is low cost graphene film production that will have valuable impact on faster adoption of this device.

1. Introduction

In this paper we develop and tasted low light low cost state of the art LPE graphene/n-Si Schottky junction solar cell with 1% efficient for 0.25 sun and 0.1% for 2 sun. The solar cells have better performances in low light than in normal light intensity which recommends it for the applications in low light geographical conditions. There performances mainly depend on the quality of the LPE graphene film and the treatment. Main contribution comes from R_{sheet} of the graphene film. The additional reason comes from treatments of graphene films with ozone, annealing and atmospheric conditions. The second realized main goal is low cost graphene film production that will have valuable impact on faster adoption of this device.

References
[1] Valentina Janošević et al., *Prog. Photovolt: Res.Appl.* (2015).
[2] Lachlan J. Larsen et al., *RSC Adv.* **5**, 38851 (2015).
[3] Yi Song et al., *Nano Lett.* **15**, 2104 (2015).
[4] Francesco Bonaccorso et al., *Science* **347**, 1246501(2015).

Transparent and conductive films from liquid phase exfoliated graphene

T. Tomašević-Ilić[1], J. Pešić[1], I. Milošević[1], J. Vujin[1], A. Matković[1], M. Spasenović[1] and R. Gajić[1]

[1]*Center for Solid State Physics and New Materials, Institute of Physics, University of Belgrade, Pregrevica 118, 11080 Belgrade, Serbia*
e-mail: ttijana@ipb.ac.rs

Liquid phase exfoliation of graphite presents a promising route for large-scale graphene production [1]. We describe basic advantages and disadvantages of the controlled deposition of few-layer graphene using the Langmuir-Blodgett (LB) method, which is compatible with usage in transparent conductors [2,3]. The graphene sheets (GS) were exfoliated from graphite by ultrasonic treatment in N-Methyl-2-pyrrolidone (NMP) and dimethylacetamide (DMA) solvents. For comparison, graphene sheets were also exfoliated in a water solution of surfactants. We confirm a higher exfoliation rate for surfactant-based processing compared to NMP and DMA. Furthermore, we demonstrate that our films exfoliated in NMP and DMA and deposited with LB have a higher optical transmittance compared to films obtained with vacuum filtration, which is a necessary step for GS exfoliated in water solutions [4]. The structural, optical and electrical properties of graphene layers were characterized with scanning electron microscopy, atomic force microscopy, ellipsometry, UV/VIS spectrophotometry and sheet resistance measurements. Our facile and reproducible method results in high-quality transparent conductive films with potential applications in flexible and printed electronics and coating technology.

REFERENCES
[1] K. R. Paton et al., Nat. Mater. 13, 624 (2014).
[2] H. K. Kim et al., Nanoscale 5, 12365 (2013).
[3] F. Bonaccorso et al., Nat. Photon. 4, 611 (2010).
[4] M. Lotya et al., J. Am. Chem. Soc. 131, 3611 (2009).

Chemical Doping Of Langmuir-Blodgett Assembled Graphene Films For Flexible Transparent Conductive Electrodes

<u>A. Matković</u>[a], I. Milošević[a], M. Milićević[a], T. Tomašević-Ilić[a], J. Pešić[a], M. Musić[a], M. Spasenović[a], Dj. Jovanović[a], B. Vasić[a], M. R. Belić[b] and R. Gajić[a]

[a]*Center for Solid State Physics and New Materials, Institute of Physics, University of Belgrade, Pregrevica 118, 11080 Belgrade, Serbia*
[b]*Texas A&M University at Qatar, P.O. Box 23874 Doha, Qatar*

Abstract. We demonstrate how chemical doping can be used to enhance properties of liquid-phase exfoliated (LPE) graphene films. Langmuir-Blodgett assembly (LBA) on a water-air interface was used to fabricate multi-layer graphene films several square centimeters in size (Fig. 1(a)). Sheet conductivity of these films is enhanced through doping with nitric acid, leading to a fivefold improvement while retaining the same transparency as un-doped films (Fig. 1(b)). In addition, chemical doping increases the work function by 0.75 eV, to a value of 4.95 eV, making these films a promising candidate for anode electrodes in hybrid solar cells and organic electronics.
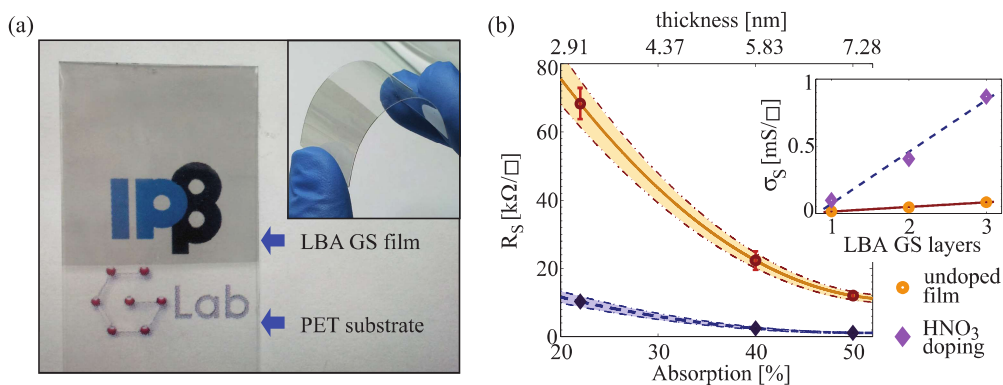
FIGURE 1. (a) 2×2 cm² LBA graphene sheet (GS) film on a polyethylene terephthalate (PET) substrate. (b) The sheet resistance (R_S) and sheet conductivity (σ_S) (inset) of stacked LBA GS layers, prior and after chemical doping.

Spectroscopic And Scanning Probe Microscopic Investigations And Characterization Of Graphene

A. Matković[a], I. Milošević[a], M. Milićević[a], A. Beltaos[a], T. Tomašević-Ilić[a], J. Pešić[a], M. M. Jakovljević[a], M. Musić[a], U. Ralević[a], M. Spasenović[a], Dj. Jovanović[a], B. Vasić[a], G. Isić[a] and R. Gajić[a]

[a]*Center for Solid State Physics and New Materials, Institute of Physics, University of Belgrade, Pregrevica 118, 11080 Belgrade, Serbia*

Abstract. Graphene synthesized by various techniques has different properties. Here we give an overview of several graphene synthesis techniques and device fabrication processes; as micromechanical exfoliation, fabrication of free standing membranes, chemical vapor deposition, liquid phase exfoliation, Langmuir-Blodgett assembly, wet transfer, shadow mask and UV photolithography. We employ various scanning probe and optical spectroscopy techniques to determine how these different fabrication processes affect properties of graphene, and present advantages and drawbacks for various applications.

In particular we focus on optical properties of graphene obtained using spectroscopic ellipsometry, and how these are altered by the interaction with an ambient [1], or various dielectric and metallic substrates [2], or by different fabrication processes [3]. We highlight how transfer residue and sample annealing affect optical properties of graphene [3], as well as how the interaction between graphene and a gold substrate can be observed through spectroscopic ellipsometry and Kelvin probe force microscopy [2]. In addition, we demonstrate how graphene can be manipulated by an atomic force microscope, using dynamic plow lithography [4].

REFERENCES

1. Matković, A., Beltaos, A., Milićević, M., Ralević, U., Vasić, B., Jovanović, Dj., and Gajić, R., *Journal of Applied Physics* **112**, 123523 (2012).
2. Matković, A., Milićević, M., Chhikara, M., Ralević, U., Vasić, B., Jovanović, Dj., Belić, M., Bratina, G., and Gajić, R., *Journal of Applied Physics* **117**, 015305 (2015).
3. Matković, A., Ralević, U., Chhikara, M., Jakovljević, M. M., Jovanović, Dj., Bratina, G., and Gajić, R., *Journal of Applied Physics* **114**, 093505 (2013).
4. Vasić, B., Kratzer, M., Matković, A., Nevosad, A., Ralević, U., Jovanović, Dj., Ganser, C., Teichert, C., and Gajić, R., *Nanotechnology* **24**, 015303 (2013).

Република Србија
Универзитет у Београду
Факултет за физичку хемију
Д.Бр.2014/0318
Датум: 20.05.2019. године

На основу члана 29. Закона о општем управном поступку („Сл. гласник РС", бр.18/2016 и 95/2018) и службене евиденције издаје се

УВЕРЕЊЕ

Томашевић-Илић (Драган) Тијана, бр. индекса 2014/0318, рођена 19.10.1982. године, Београд, Савски венац, Република Србија, уписана школске 2018/2019. године, у статусу: самофинансирање; тип студија: докторске академске студије; студијски програм: Физичка хемија.

Према Статуту факултета студије трају (број година): три године.
Рок за завршетак студија: у двоструком трајању студија.

Ово се уверење може употребити за регулисање војне обавезе, издавање визе, права на дечији додатак, породичне пензије, инвалидског додатка, добијања здравствене књижице, легитимације за повлашћену вожњу и стипендије.

Овлашћено лице факултета

РЕПУБЛИКА СРБИЈА

УНИВЕРЗИТЕТ У БЕОГРАДУ

ФАКУЛТЕТ ЗА ФИЗИЧКУ ХЕМИЈУ

ДИПЛОМА

О СТЕЧЕНОМ ВИСОКОМ ОБРАЗОВАЊУ

Томашевић Драгана Тијана

РОЂЕН-А 19-X-1982. ГОДИНЕ У БЕОГРАДУ, САВСКИ ВЕНАЦ

СРБИЈА , УПИСАН-А 2001/2002.ШКОЛСКЕ ГОДИНЕ,

А ДАНА 3. ЈУНА 2011. ГОДИНЕ, ЗАВРШИО-ЛА ЈЕ СТУДИЈЕ НА

ФАКУЛТЕТУ ЗА ФИЗИЧКУ ХЕМИЈУ

СА ОПШТИМ УСПЕХОМ 8,67 (ОСАМ И 67/100) У ТОКУ СТУДИЈА И ОЦЕНОМ

10 (ДЕСЕТ) НА ДИПЛОМСКОМ ИСПИТУ.

НА ОСНОВУ ТОГА ИЗДАЈЕ МУ-ЈОЈ СЕ ОВА ДИПЛОМА О СТЕЧЕНОМ ВИСОКОМ

ОБРАЗОВАЊУ И СТРУЧНОМ НАЗИВУ

ДИПЛОМИРАНИ ФИЗИКОХЕМИЧАР

РЕДНИ БРОЈ ИЗ ЕВИДЕНЦИЈЕ О ИЗДАТИМ ДИПЛОМАМА 217/2011

У БЕОГРАДУ, 6.ЈУНА 2011. ГОДИНЕ

ДЕКАН   РЕКТОР

проф. др Шћепан Миљанић   проф. др Бранко Ковачевић

Република Србија

Универзитет у Београду
Факултет за физичку хемију, Београд

Оснивач: Република Србија

Дозволу за рад број 612-00-02666/2010-04 од 10. децембра 2010.
године је издало Министарство просвете и науке Републике Србије

Диплома

Тијана, Драган, Томашевић

рођена 19. октобра 1982. године у Београду, Савски венац, Република Србија,

уписана школске 2011/2012. године, а дана 5. марта 2015. године завршила је

мастер академске студије, другог степена, на студијском програму Физичка хемија,

обима 60 (шездесет) бодова ЕСПБ са просечном оценом 9,20 (девет и 20/100).

На основу тога издаје јој се ова диплома о стеченом високом образовању и академском називу

мастер физикохемичар

Број: 3682500

У Београду, 13. марта 2015. године

Декан
Проф. др Шћепан Миљанић

Ректор
Проф. др Владимир Бумбаширевић

ВЕЋЕ НАУЧНИХ ОБЛАСТИ   Београд, 25.04.2019.
ПРИРОДНИХ НАУКА   02-07 Број: 61206-1782/2-19
     МЦ

На основу члана 48. став 5. тачка. 3. Статута Универзитета у Београду ("Гласник Универзитета у Београду", број 201/18) и чл. 14. – 21. Правилника о већима научних области на Универзитету у Београду („Гласник Универзитета у Београду", број 134/07, 150/09, 158/11, 164/11, 165/11, 180/14, 195/16, 196/16 и 197/17), а на захтев Факултета за физичку хемију, број: 306/2 од 12.04.2019. године, Веће научних области природних наука, на седници одржаној 25.04.2019. године, донело је

О Д Л У К У

ДАЈЕ СЕ САГЛАСНОСТ на предлог теме докторске дисертације ТИЈАНЕ ТОМАШЕВИЋ-ИЛИЋ, под називом: „Површинска модификација графена ексфолираног из течне фазе и депонованог Лангмир-Блоџетовом методом".
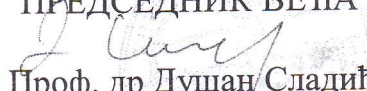
ПРЕДСЕДНИК ВЕЋА
Проф. др Душан Сладић

Доставити:
- Факултету
- архиви Универзитета